ABSTRACT

AN INNOVATIVE PROTECTIVE JACKET FOR STRUCTURES SUBJECT TO BLAST LOADS: A COMPREHENSIVE EXPERIMENTAL AND SIMULATION STUDY

by
Nicholas J. Carlson

As the importance of protective engineering and multi-hazard mitigation design has grown in recent years, the development of an effective structural protection system that aids in the preservation of life safety during blast events is an important topic of research in structural engineering. This protection is especially vital for blast and explosion mitigation, where a vehicle-borne bomb or an improvised explosive device can readily cause an under-designed structure with insufficient redundancy to undergo progressive collapse due to the removal of its first-floor columns. An especially pressing research need is the consideration of structures that require blast protection, but—due to time or budget constraints, lack of available space, unusual construction techniques or other externalities—cannot be sufficiently strengthened by traditional structural hardening techniques such as those described in the FEMA counterterrorism design primers.

As an alternative, the author proposes the development of an ablative, sacrificial protective jacket, based on prior research on the use of water as hazard mitigation to protect weapon storage facilities from accidental munitions detonation. The proposed system consists of a relatively thick layer of water sandwiched between two thin layers of polyethylene film or a similar polymer membrane, with the entire assembly wrapped around or affixed to the vulnerable structural elements. The water layer is theorized to reduce the incident and reflected pressure of the blast wave through two principal modes of attenuation: the reduction of the blast wave's energy through harnessing the high enthalpy of fusion and specific heat of water (the "thermodynamic mode") and the transformation of the blast pressure into kinetic energy (the "kinetic mode"). The theoretical mitigation pathways are discussed and analyzed, and the necessary assumptions required for the jacket to mobilize its protective capacity within the short timescale of a blast event are shown to be valid—namely, that the initial disruption of the water layer by the blast wave forms an ultra-fine mist of 20 μm to 30 μm diameter droplets that can evaporate in approximately 1 ms.

The investigation of the ablative ability of the proposed, 1.5 in to 6.0 in protective jackets takes the form of a series of two- and three-dimensional finite element simulations which measure the protective capacity of various water jacket volumes protecting various structures from both impact and blast. For the blast loads (scaled standoffs from 5 ft/lb$^{1/3}$ and 1.25 ft/lb$^{1/3}$) and structural configuration chosen, the optimum energy reduction occurs when the jacket is approximately 4.5 in thick. For cases where a thinner jacket is desired, the author used the relative energy dissipation data to derive an empirical relationship between the thickness of a jacket, the blast load it is subjected to and its predicted energy dissipation capacity. This relationship can be used by design engineers to use the proposed design method, employing the integrals of $P-\Delta$ pushover curves, in order to meet important performance criteria that ensure life safety during catastrophic events.

AN INNOVATIVE PROTECTIVE JACKET FOR STRUCTURES SUBJECT TO BLAST LOADS: A COMPREHENSIVE EXPERIMENTAL AND SIMULATION STUDY

by
Nicholas J. Carlson

A Dissertation
Presented to the Faculty of
New Jersey Institute of Technology
in Partial Fulfillment of the Requirements for the Degree
of Doctor of Philosophy in Civil Engineering

Department of Civil and Environmental Engineering

May 2013

APPROVAL PAGE

AN INNOVATIVE PROTECTIVE JACKET FOR STRUCTURES SUBJECT TO BLAST LOADS: A COMPREHENSIVE EXPERIMENTAL AND SIMULATION STUDY

Nicholas J. Carlson

Dr. M. Ala Saadeghvaziri, Dissertation Advisor — Date
Professor of Civil and Environmental Engineering, NJIT

Dr. John Schuring, Committee Member — Date
Professor of Civil and Environmental Engineering, NJIT

Dr. Methi Wecharatana, Committee Member — Date
Professor of Civil and Environmental Engineering, NJIT

Dr. Bruce Bukiet, Committee Member — Date
Associate Professor of Applied Mathematics, NJIT

Dr. Ernest Baker, Committee Member — Date
Senior Research Scientist, ARDEC, U.S. Army

BIOGRAPHICAL SKETCH

Author: Nicholas J. Carlson

Degree: Doctor of Philosophy

Date: May 2013

Undergraduate and Graduate Education:

- Doctor of Philosophy in Civil Engineering,
  New Jersey Institute of Technology, Newark, NJ, 2013
- Master's of Science in Civil Engineering,
  New Jersey Institute of Technology, Newark, NJ, 2013
- Bachelor of Science in Civil Engineering,
  New Jersey Institute of Technology, Newark, NJ, 2007

Major: Civil Engineering

Presentations and Publications:

Carlson, N. (2011). "Parameter study and finite element analysis of a multi-hazard protective jacket for structural members." Poster. Graduate STEM Fellows in K-12 Education (GK-12) Graduate Fellow Research Poster Session, National Science Foundation GK-12 Projects Annual Conference, Washington, D.C.

Carlson, N., and Saadeghvaziri, M. A. (2010). "On effectiveness of water in attenuating blast loads." Presented at 2010 International Conference on Computational Engineering and Science, Las Vegas, NV.

Carlson, N., and Saadeghvaziri, M. A. (2010). "On multi-hazard considerations in design of structures." Submitted to 9th US National and 10th Canadian Conference on Earthquake Engineering, Toronto, ON, Canada.

Carlson, N., and Saadeghvaziri, M. A. (2010). "A multi-hazard protective jacket for structural members." Submitted to the 2010 Structures Congress, Orlando, FL.

Carlson, N., and Saadeghvaziri, M. A. (2010). "ProJackB4 – Protective Jacket to Blunt Blast on Bridges and Buildings." Presentation. Homeland Defense Technology Center, Picatinny Arsenal, NJ.

Saadeghvaziri, M. A. and Carlson, N. (2009). "ProJackB4 – Protective Jacket to Blunt Blast on Bridges and Buildings." Presentation. Technology Research Day, Armament Research Development and Engineering Center (ARDEC), Newark, NJ.

For Tom and Lisa, my parents

ACKNOWLEDGMENTS

This thesis would not have been possible without the support and encouragement of my advisor, Dr. M. Ala Saadeghvaziri; he has been a constant source of enthusiasm, suggestions and assistance, especially at the times when I felt overwhelmed by the scope of my research. This work continues the research begun by my colleague Dr. Navid Allahverdi, who provided a sound foundation for me to build on.

I am indebted to the members of my dissertation committee: Dr. Methi Wecharatana, for encouraging me to apply to graduate school; Dr. John Schuring, for supporting me during my first year in the Ph.D. program; Dr. Bruce Bukiet from the College of Science and Liberal Arts, the principal investigator of the NSF *Graduates in K-12 Education* project C^2PRISM, from which I received the funding (and the communication skills) necessary to complete this research; and Dr. Ernest Baker, who graciously took time from his busy schedule at Picatinny Arsenal to join my committee.

To Newark Public Schools teachers Monique Buggs, Mridula Bajaj and Dr. Ferdinand Oguama, my colleagues in the high school classrooms where I learned effective teaching methods, presentation skills and the value of resourcefulness, I am forever grateful for the experience.

Much of this research would have been insurmountably difficult without the technical assistance of Allyn Luke, Frank Johansson and Frank Golub. The courses taught by Dr. Bernard Koplik and Dr. I. Joga Rao in the Mechanical Engineering department and Dr. Yassine Boubendir and Dr. Michael Booty in Mathematical Sciences helped expand my knowledge of structural mechanics and numerical analysis. My fellow doctoral students and officemates Dr. Bakhtiar Feizi, Dr. Shabnam Darjani and Oruba Rabie have been great resources and fantastic friends, and I wish them luck with their future careers.

Finally, I'd like to thank my family for their patience, love and unconditional support, and for always being there at the times I needed them the most.

TABLE OF CONTENTS

TABLE OF CONTENTS
(Continued)

Chapter **Page**

LIST OF TABLES

LIST OF FIGURES

LIST OF FIGURES
(Continued)

Figure **Page**

LIST OF FIGURES
(Continued)

Figure **Page**

LIST OF FIGURES
(Continued)

Figure **Page**

LIST OF DEFINITIONS

1-DOF	One degree of freedom, in a dynamic structural system
ARDEC	[U.S. Army] Armament Resarch, Development and Engineering Center
C-4	Composition-4 plastic explosive
CONWEP	Conventional weapon effect calculation tool, published by the U.S. Army Corps of Engineers
JH	Johnson-Holmquist damage model for brittle materials
leeward	Facing away from an incoming blast wave.
LVDT	Linear voltage displacement transducer
RHT	Riedel-Hiermaier-Thoma constitutive material model for brittle materials
SPH	Smoothed-particle hydrodynamics, a meshless finite element method
UFM	Ultra-fine mist, consisting of droplets 20 μm to 30 μm in diameter
windward	Facing towards an incoming blast wave.

LIST OF SYMBOLS

D	Johnson-Holmquist relative damage parameter; $D = 0$ for undamaged material and $D = 1$ for bulk failure
ψ	Relative energy dissipation of the protective jacket
p_o^+	Peak reflected blast pressure
p_s^+	Peak incident blast pressure
R	Standoff distance from center of blast
U	Velocity of blast shock wave
W	Weight of explosive
Z	Scaled blast standoff distance using the Hopkinson-Cranz scaling equation $Z = RW^{-1/3}$

CHAPTER 1

INTRODUCTION

1.1 Background and Motivation

Protective engineering has become a paramount concern in recent decades, as engineers and architects attempt to balance the traditional concerns of aesthetics and functionality with the need to protect and preserve structures and their contents from catastrophic loss in the rare event of a disaster, whether natural (for example, seismic events or hurricanes), unintentional (fires and other accidents), or intentional (terrorist attacks).

An effective protection system, while never an ironclad guarantee of safety, must also sufficiently defend against multiple possibilities without unnecessarily wasting resources (Mays and Smith 2001). In the case of protection against explosions, especially those caused by intentional acts of terrorism, guidelines for new construction exist for good protective engineering design practices (FEMA 2003), but comparatively less work has been done regarding the retrofitting of existing structures for multi-hazard conditions (Carlson and Saadeghvaziri 2010b). The strengthening of existing structures is often economically or practically infeasible, requiring large labor and material costs, the prolonged disruption of services provided by the structure, and the time to analyze the existing structure and design a strengthening system that ties into it. One possible remedy to this problem is to design a protective system that readily applies to the exterior of a vulnerable structure which would redirect the energy of a blast load rather than strengthen the structure to endure it.

1.2 Objectives of This Work

The main objectives of the study are twofold:

Simulating the effects of blast loads on structural members protected by an energy-dissipating jacket: using the finite element method and commercially-available analysis

software, numerically analyze the response of structural elements subjected to specified blast loadings with and without protective water-filled jackets intended to dissipate the energy of the oncoming blast through kinetic and thermodynamic energy absorption means. Different thicknesses of the protective jacket will be analyzed in order to identify the optimal thickness that minimizes the amount of energy transmitted to the structural member during the blast event.

Developing an empirical relationship for structural designers: using the blast simulations as well as additional impact event simulations, propose an empirical relationship that predicts the amount of energy dissipation that a water-filled jacket of a specified thickness will enable for a given design blast intensity, as well as a relationship betwen impact and blast tests that will allow for the substitution of an laboratory impact test for one needing live explosives when testing the capacity of a water-filled protective jacket.

1.3 Outline

The remainder of this chapter reviews the initial design process of the proposed protective jacket, including the required design parameters and a review of the development of the prototype designs and their manufacture. Chapter 2 reviews the existing literature on the topics of blast mitigation through ablation and the effects of water on the structural effects of explosive loading.

Chapter 3 discusses the theoretical modes of energy dissipation relevant to the design of the protective jacket – a "kinetic mode" consisting of the breakup and acceleration of the standing water into fast-moving droplets, and a "thermodynamic mode" where the droplets further break up into a fine mist and absorb the heat necessary to vaporize from the blast wave. Example calculations demonstrate the high capacity for dissipation of a modest amount of water in the presence of a blast from a typical improvised explosive device's payload.

Chapter 4 is a review of the relevant topics in finite element analysis used to develop

the numerical models formulated in later chapters. The overview includes discussions of the various solver methods, typical equations of state encountered in blast simulations, and a method for closely approximating the effects of an explosive device on a structure without simulating the surrounding atmosphere.

Chapters 5 and 6 document in more depth the qualitative and quantitative experimental testing and numerical analysis performed by the author that served as the "proof of concept" of the protective jacket which preceded the parameter study described in later chapters. The research described in these chapters can be broken down into three categories: impact and live blast testing in Chapter 5 and finite element analysis in 6.

Chapter 7 begins with a simple two-dimensional finite element analysis of impact on a protected slab. The discretization methods (both traditional mesh and mesh-free), material models and equations of state are introduced and discussed in Chapter 4.

Chapter 8 extends the analyses from the prior chapter and introduces the finite element analysis of the jacket subject to a blast load, also taking into account the thermodynamic properties of the jacket.

Chapter 9 takes the results from the prior chapters and synthesizes them into a general, empirical relationship that predicts the energy dissipation capacity of the jacket in the presence of a given blast load, and further relates that capacity to the performance of a given structural element, providing an estimation of the expected reduction in peak structural deformation.

Chapter 10 summarizes the results from the prior three chapters, and provides recommendations for further analysis and applying the results to protective engineering design.

1.4 Identification of Parameters

The structural hardening required to protect the vulnerable members in an existing structure falls into two categories: (1) strengthening retrofitting, where the strength and ductility of the structural members, and thus their resistance to blast loads, are increased by installing

additional structural material that increases their mass and/or strength, and (2) attenuation retrofitting, where the energy of the blast load is dissipated or redirected, either by the ductility of the members themselves or by sacrificial claddings and protective layers installed on or around the members to be protected (Mays and Smith 2001).

Though a well-detailed, redundant steel frame with judiciously designed connections, multiple redundant load paths and reserve strength from meeting servicability limits will have an high inherent blast resistance (Carter 2011), many times, the purchasing, installation and maintenance of attenuation systems is more practical if not more economical than the design, demolition, construction and refinishing required for the strength retrofitting of structures that do not meet these standards of design.

Five general parameters were considered by the author for the initial design of an attenuation system:

- The attenuating material ought to be relatively *cost-effective*, both in terms of acquisition and deployment,
- it should be *readily available* and not require special handling or manufacturing,
- it should be *chemically inert*, and not degrade in the presence of typical outdoor conditions or adversely affect the performance of structural materials it comes in contact with after a blast effect,
- it needs to be *non-combustible*, and not reduce a structure's fire-resistance rating (the amount of time a passive fire protection system can withstand failure), and
- it ought to be *durable* enough to be left alone with minimal maintenance.

After considering these requirements and performing an initial review of various protective systems in use in mechanical engineering and military applications, the author chose to develop a blast attenuation system using water as the mitigating material. This configuration

has the advantage of being suitable for combination with other forms of protection, such as the confinement wrapping of concrete columns in seismically active areas, or the addition of fire-retardant layers or filler to provide additional protection against fire.

1.5 Initial Design

The general description of the protective system is a layer of water confined inside a flexible polyethylene container, which can be affixed to walls or wrapped around columns and beams, and contained within an architectural façade. This system would lend itself to scenarios where protection is needed on short notice without unnecessarily intruding on public space or adversely diminishing the appearance of the structure, as well as having the advantage of possibly integrating other forms of structural protection (such as seismic confinement or fire suppressant) where needed. An example of one deployment of this system is shown in Figure 1.1.

The initial designs of the protective shell were simple refinements of the original "plastic bag filled with water" used in the initial quantitative impact tests. The first refinement was the use of "quilting" – using a commercial thermal sealer, the jacket was subdivided into a mesh of "pockets" with pockets containing an attenuation material and

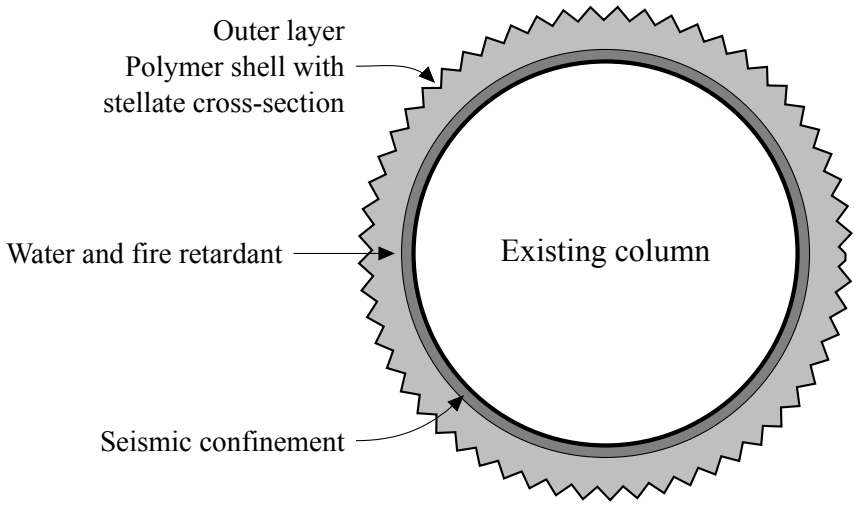

Figure 1.1 Schematic of protective system, including seismic confinement.

Figure 1.2 Quilted water-filled jacket.

Figure 1.3 Quilted bentonite jacket, with "checkerboard" fill pattern.

empty pockets arranged in a checkerboard pattern; examples are shown in Figures 1.2 and 1.3. This design is intended to give the attenuation material room to expand laterally, parallel to the pressure front, increasing its ability to convert blast pressure into kinetic energy. Since at short time scales, liquid subjected to an impulse behave as solids, the expansion channels keep the water from only transmitting the bulk of the energy into the slab.

As will be described in section 2.4, the results of an analysis of the effects of column cross-sectional geometry on peak blast pressure by Allahverdi (2010) suggested an additional refinement in the form of a serrated, stellate cross-section (Figure 1.5) would provide multiple leading edges to reduce the maximum pressure and impulse.

A set of prototype shells (Figure 1.4) featuring both these refinements were manufactured by the Center for Manufacturing Systems at NJIT for the author and used in the preliminary live blast testing. The shells were formed from polyethylene sheets with a vacuum forming process, using a mold milled from porous metal (Figure 1.6) to eliminate the need for venting holes; the shell has a thick, rigid backing which holds its shape easily, while the pockets for the attenuation material are thinner and more easily ruptured, suitable for their sacrificial role.

The shells are then filled with water, then thermally and chemically sealed with an adhesive polyethylene backing sheet. This completes the jacket and produces a prototype that is suitable for testing; so far, eight of these completed jackets have been used in the qualitative blast tests described in section 5.3 on page 60.

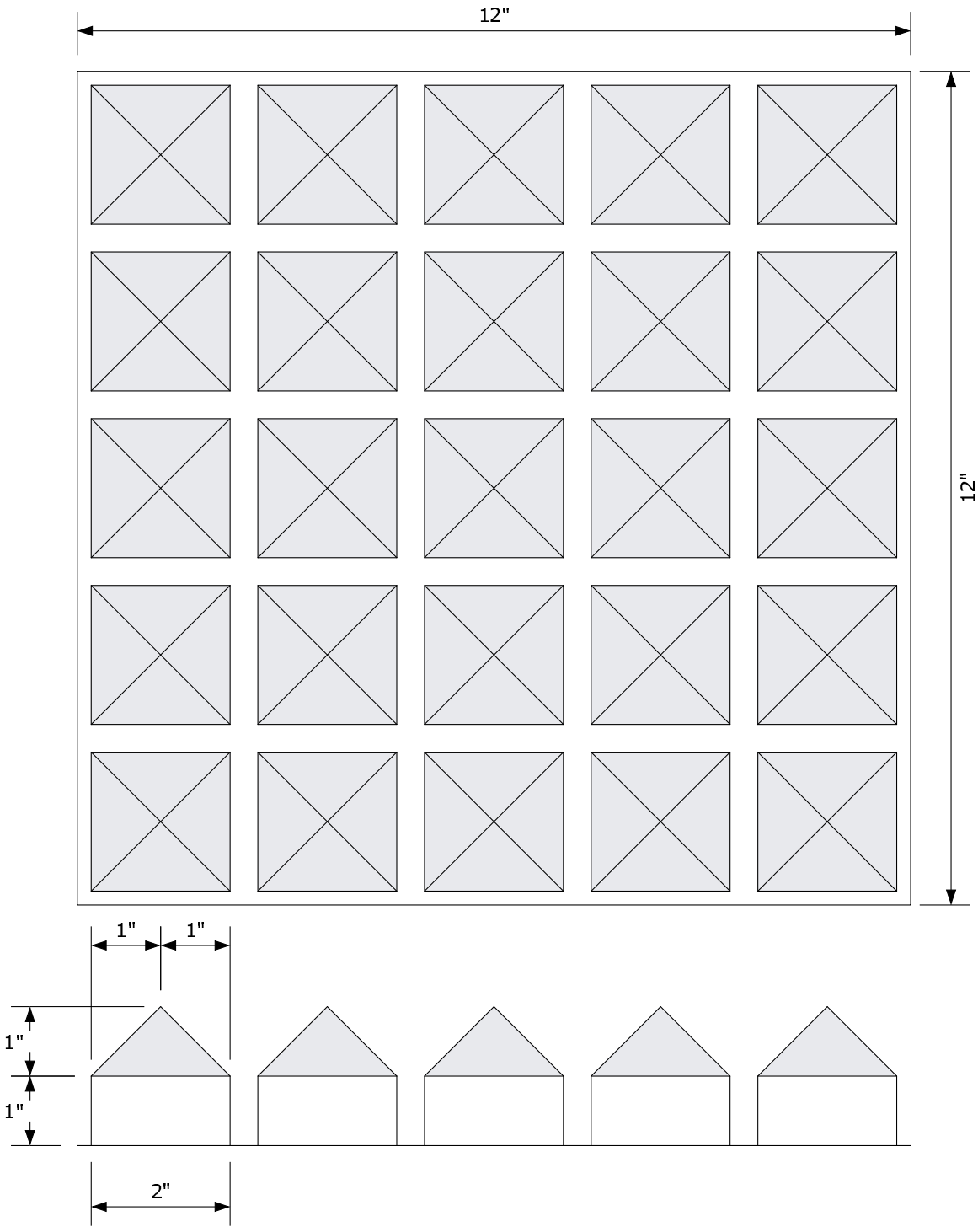

Figure 1.4 Schematic of refined jacket prototype, featuring ”quilting” and leading edges.

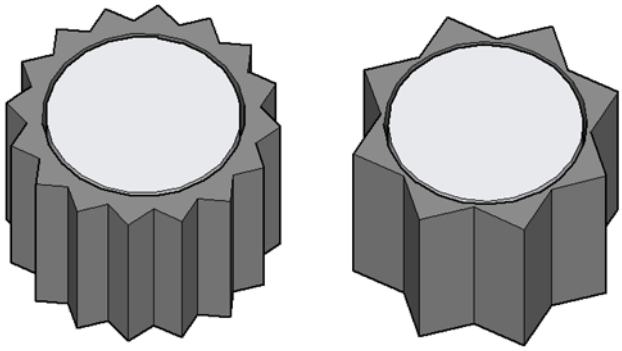

Figure 1.5 Stellate cross-sections with multiple possible leading edges.

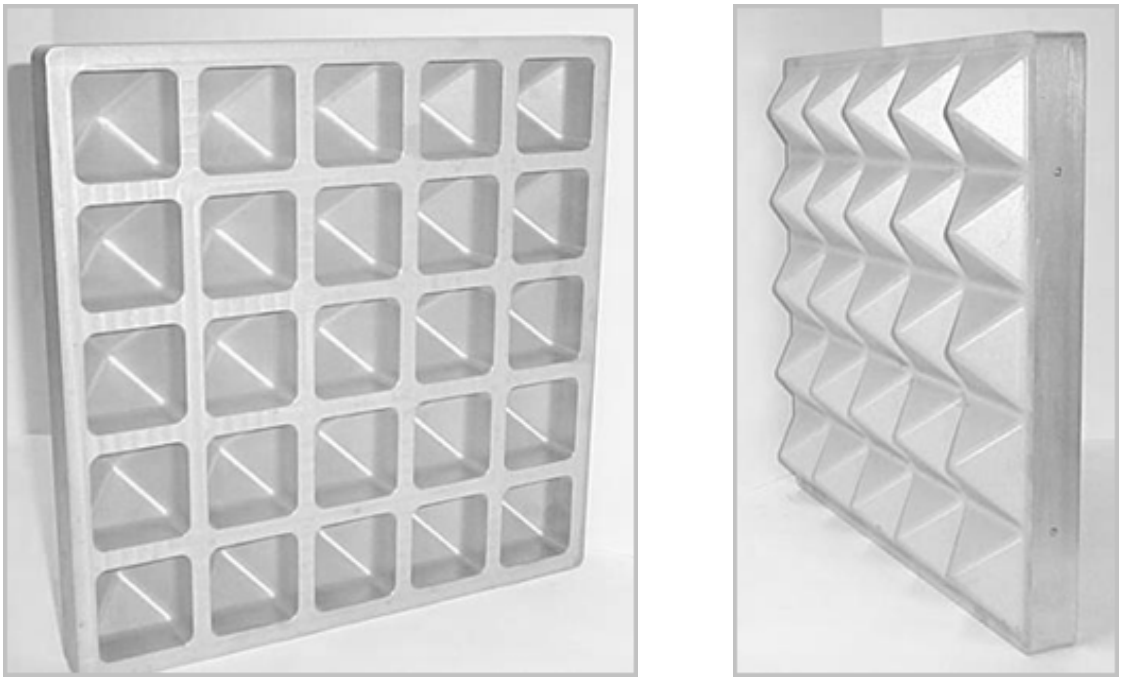

Figure 1.6 Porous metal vacuum mold, manufactured by CMS.

CHAPTER 2

LITERATURE REVIEW

2.1 The Mechanics of an Explosion

In general, an explosion is a physical, chemical or nuclear reaction which causes a violent release of energy accompanied by a rapid increase of volume of the gaseous products. The sudden volume increase causes a rapidly-traveling pressure differential (Figure 2.1), forming a shock wave which propagates through the surroundings, engulfing and accelerating whatever obstacles it encounters; behind the peak positive pressure at the shockwave front, a negative pressure zone is formed, causing a partial vacuum that can carry debris long distances. The effects on buildings of the compressed air blast wave released by the explosion are summarized in Figure 2.2. The duration of the blast event is usually on the scale of tens of milliseconds, as compared to the usual duration of seconds for impact loading, or some minutes for other dynamic loadings such as wind or seismic events. The blast event affects the vertical stability of a structure both through the damage or removal of columns and the direct imposition of distributed loads on floor elements.

Measurements of the pressure and impulse of an explosive device depend on the

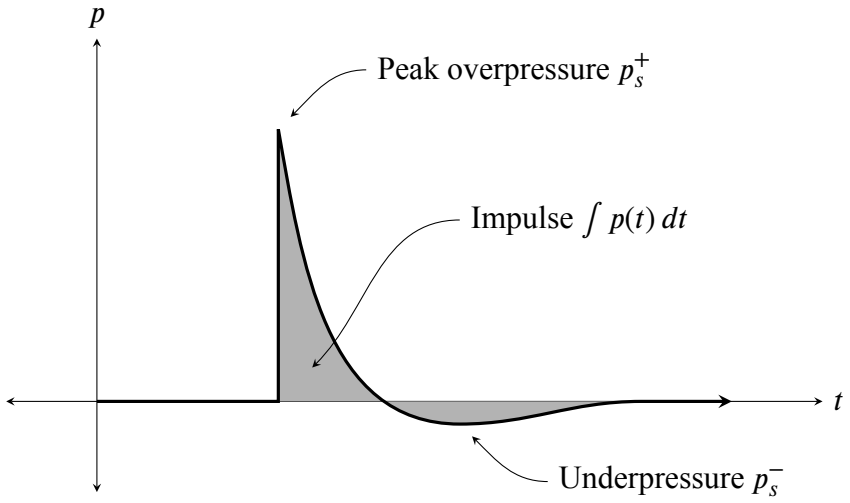

Figure 2.1 Typical pressure history of a free-air blast.

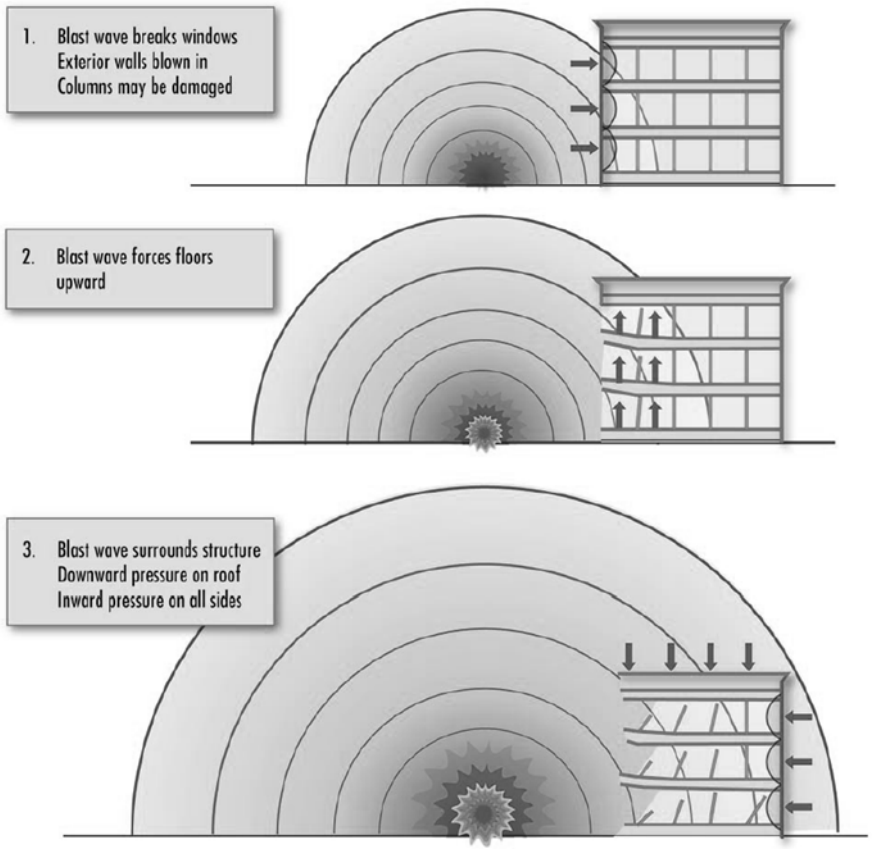

Figure 2.2 Blast pressure effects on a structure (FEMA 2003).

quantity of explosive used and the standoff distance from the center of the blast. However, it can be shown that for an ideal spherical explosive of radius r set a length of R away from a blast pressure measurement device, the maximum pressure generated by the blast will be constant for all pairs of values of r and R such that R/r is constant. Generally, however, rather than the radius of the equivalent sphere of explosive, the cube root of the explosive's weight W is used as the scale factor, a form of scaling called Hopkinson-Cranz scaling, so that the scaled blast distance is $Z = RW^{-1/3}$ (Zukas and Walters 1998). Selected values of Z, their corresponding peak pressures and a description of the blasts' effects on conventional buildings are shown in Table 2.1 (Department of the Navy 1999).

Table 2.1 Damage to Structures vs. Scaled Distance

Scaled distance $Z = R/W^{1/3}$	**Peak presssure** p_s^+	**Description of damage to a light, unreinforced structure**
6	29 psi	Complete destruction
9	12 psi	Severe structural damage, global collapse
10.5	8.4 psi	Major structural damage, local collapse
18	3.6 psi	Damage costing 50% of replacement cost
25	2.3 psi	Damage costing 20% of replacement cost
30	1.7 psi	10% of replacement cost; 100% glazing broken
40	1.1 psi	Minor structural damage; 60% glazing broken
50	0.8 psi	Negligible structural damage; 30% glazing broken

Source: Department of the Navy (1999)

2.2 Blast Protection Design

2.2.1 Progressive Collapse

It is absolutely imperative that a building's occupants remain as safe as possible in the event of an attack or disaster. As well as the concerns regarding the interruption of important building subsystems such as fire suppression, communication systems and evacuation routes, and the risk of occupant injuries from hazards such as airborne debris and smoke inhalation (Committee on Feasibility, 1995), the global stability of the damaged structure is a vital consideration.

If an explosion destroys load-bearing elements but the remaining elements are unable to compensate for the change in load path, the rest of the structure is at risk of undergoing a progressive collapse that will cause damage greatly out of proportion to the size of the instigating blast. For example, the analysis (Ngo et al. 2007) of a typical Australian cast-in-place concrete high-rise simulating the effects of a nearby ground-level explosion demonstrates the risk of progressive collapse of a frame when blast loading effectively removes structural members local to the event if the rest of the frame is not capably detailed to withstand the effects of the failure of some of its supporting members.

The importance of considering progressive collapse is corroborated by events such

Figure 2.3 Exterior view of Alfred P. Murrah Federal Building after bombing and subsequent progressive collapse (FEMA 2003).

as the partial building collapse caused by an accidental natural gas explosion in the Ronan Point disaster of 1968 (Hadden 2003) or the bombing of the Alfred P. Murrah Federal Building in Oklahoma City via a vehicle-borne explosive device in 1993 (Sozen et al. 1998, Pujol and Smith-Pardo 2009, Liu 2010; also see Figure 2.3).

In both cases, the damage caused by the initial explosion (the loss of one precast concrete wall panel in Ronan Point, the destruction of two columns and the shear failure of two more in Oklahoma City) was dwarfed by the destruction caused by progressive collapse immediately after the explosion event due to the catastrophic inability of the frames in the locality of the event to even temporarily handle the increased loads redirected through the remaining, undamaged structural elements, due to a lack of redundancy or interconnectivity (Nair 2006). Considering these examples and others, if a structure is likely to be unable to endure a local failure without undergoing progressive collapse, one tactic to reduce the chance of disproportionate damage is to protect the most vulnerable structural members in

a manner that blunts the force of an explosion.

2.2.2 Blast Mitigation

While some explosive events are accidental (the ignition of the gas leak that caused the Ronan Point collapse, for example), the typical event a building designer wishes to safeguard against is the intentional, malicious detonation of an explosive device.

The most dangerous explosive events involve the use of car- or truck-borne explosives, which enable the relatively inconspicuous delivery of large amounts of explosive material directly to the target. In this type of attack, the structural members at ground level are the ones most vulnerable to being damaged or removed by the explosion. However, if the site surrounding the structure is properly defended by a well-designed security system—all vehicle approaches to vulnerable areas are inaccessible, physically barricaded or screened by security personnel (Hadden 2003)—the risk of such a large explosive device being successfully deployed is greatly reduced. Thus, in the design of a structure to mitigate blast, a designer may instead wish to design to safeguard against smaller explosive devices, such as those which can be carried by hand, hidden under clothing, concealed inside suitcases and backpacks, or delivered in the mail (FEMA 2003).

Blast mitigation design often conflicts directly with seismic design: generally, heavy structures resist blast loads well, since the transient event will have passed before the mass of the structure can respond to the excitation, while light structures are preferable for seismic design to reduce the lateral inertial loads generated by the structure's acceleration, so a multi-hazard design that accounts for both risks requires cautious use of engineering judgment and prior experience. However, much of the same structural detailing at joints to provide ductility and continuity in the event of a seismic event is also beneficial to ensure the vertical stability of a structure which has suffered the removal of key columns (Carter 2011, Gurley 2008).

2.2.3 Blast Pressure Prediction

Explosive events can be classified into four broad categories, depending on their proximity to reflective surfaces—ground burst explosions, where the explosive device is placed on a relatively unyielding surface; above-ground explosions, where the device is detonated at low altitude, causing complex blast wave reflections near the ground; free-air blasts away from any reflecting surfaces; and underground explosions of buried or tunnel-borne devices. Due to the nature of the explosive devices the proposed protective system aims to guard against—improvised hand-carried or vehicle-borne devices, as opposed to air-to-ground bombs or land mines—ground-burst explosions will be the predominant form of blast event considered in the analysis and design of this protective system.

Many empirical relationships between scaled blast distance and peak overpressure for various high explosive materials have been determined since interest in the subject of analytical blast load prediction grew in the post-war era. For example, Mills (1987) proposed the relationship between peak overpressure p_s^+ and scaled blast distance for a spherical, free-air blast

$$p_s^+ = \frac{1772}{Z^3} - \frac{114}{Z^2} + \frac{108}{Z}$$

where Z is expressed in SI units (i.e. $\mathrm{m/kg^{1/3}}$). Other properties of the blast wave can be determined analytically; Glasstone (1962) derives the equation for the shock wave velocity U

$$U = c_0 \sqrt{1 + \frac{\gamma + 1}{2\gamma} \cdot \frac{p_s^+}{p_a}}$$

p_s^+	peak overpressure
p_a	ambient pressure
c_0	sound velocity in atmosphere
γ	specific heat ratio ($\gamma = 1.4$in air)

Similarly, the peak reflected pressure p_o^+, caused by above-ground explosions due to the

interaction of the incident (original) blast front and the reflected front from the ground plane, is found to be

$$\begin{aligned} p_o^+ &= 2p_s^+ + \frac{(\gamma+1)\left(p_s^+\right)^2}{2\gamma p_a + (\gamma+1)\,p_s^+} \\ &= 2p_s^+\left(\frac{7p_a + 4p_s^+}{7p_a + p_s^+}\right) \end{aligned}$$

This peak reflected pressure may only be twice the incident pressure for relatively weak blasts, but may approach up to 8 to 13 times the incident blast pressure as the scaled blast distance decreases. Additional empirical and analytical relationships for blast events are discussed further in Section 4.4.3.

2.3 Blast Mitigation Materials

The structural hardening required to protect these vulnerable members falls into two categories: (1) strengthening retrofitting, where the strength and ductility of the structural members, and thus their resistance to blast loads, are increased by installing additional structural material that increases their mass and/or strength, and (2) attenuation retrofitting, where the energy of the blast load is dissipated or redirected, either by the ductility of the members themselves or by sacrificial claddings and protective layers installed on or around the members to be protected (Mays and Smith 2001). Most times, purchasing, installing and maintaining attenuation systems is more economical and practical than the costs incurred, time required and reduced practicality of the design, demolition, construction and refinishing required for strength retrofitting.

2.3.1 Sandwich Layers as Blast Mitigation Devices

Traditional sacrificial plate methods have been considered for use as protective jackets, though their performance against impulse loads varies: Xue and Hutchinson (2003) state that the deflection response of a well-designed sacrificial sandwich plate (i.e. two iden-

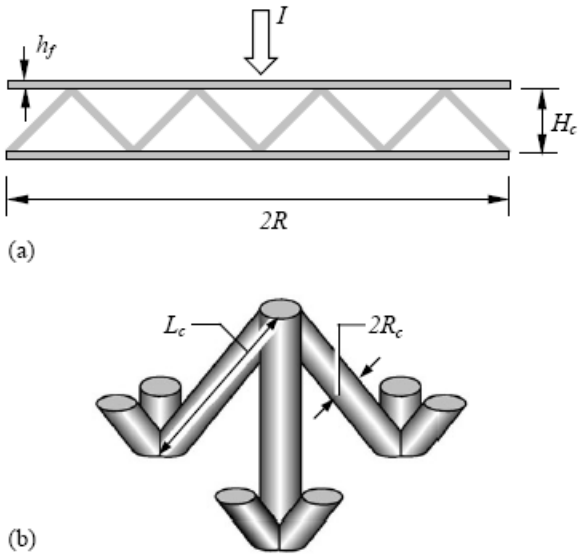

Figure 2.4 Typical sandwich plate with internal tetragonal truss element (Xue and Hutchinson 2003).

tical plates joined with a truss or honeycomb structure as in Figure 2.4) can outperform an equivalent-mass solid plate when subjected to impulse with optimum performance at a relative core density of $\overline{\rho} = 0.08$, even though the sandwich plate absorbs twice as much energy as the solid plate through plastic deformation (Figure 2.5). However, Vaziri et al. (2006) found that foam-filled honeycombed sandwich plates did not offer any additional resistive advantage to sandwich plates without unfilled cores, and increasing the foam-filled sandwich thickness may possibly reduce their strength further. Most importantly, from a practical standpoint, the cost of constructing honeycombed and sandwiched plates would be prohibitively high for the amount of protective covering required for a typical protective structural engineering design.

2.3.2 Water as a Blast Mitigation Material

Some recent research, both theoretical and experimental, has been done regarding the use of water as a sacrificial explosive blast attenuation material (Joachim and Lunderman 1997, Cheng et al. 2005, Absil and Bryntse 2006, Chong et al. 1999). The first research on the effects of water on blast intensities (Eriksson 1974) demonstrated that a blast event's peak

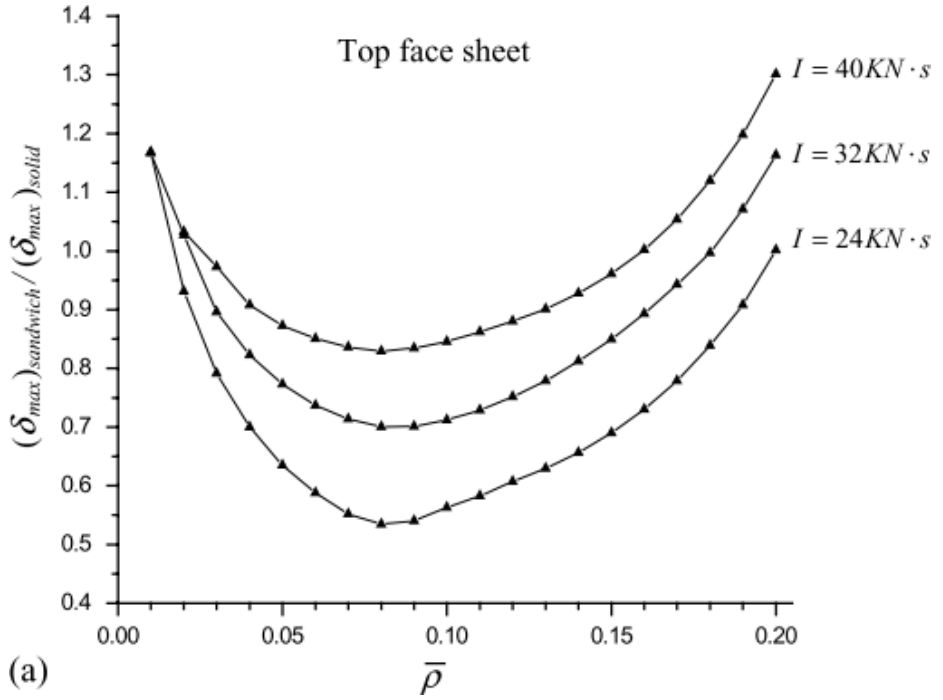

Figure 2.5 Maximum deflection response of the top face of a sandwich plate with relative core density $\overline{\rho}$ subjected to impact, with respect to a solid plate of equal mass (Xue and Hutchinson 2003).

pressure caused by a weight of explosive of up to 1.1 lb [0.5 kg] could be halved, when the explosion event occurs directly in contact with and surrounded by a layer of water weighing about 5 lb.

Further research describes the physical mechanisms by which the explosive pressure is mitigated: Keenan and Wager (1992) state that the protective water will aerosolize in the presence of an explosion and mix with the heated detonation gases, cooling them and causing the gas pressure to decrease; Eriksson and Vretblad (1994) state that the water additionally causes a reduction in the rise in temperature caused by afterburning of the detonation products; and Absil and Bryntse (2006) theorize that the water will also transform the momentum of the shock wave into kinetic energy, further sapping its strength.

A contemporary example of this use of water as a mitigation device was demonstrated in the tests to evaluate the effect of the mass ratio of water to explosive performed by Joachim and Lunderman (1997), and corroborated by the numerical analysis by Chong

et al. (1999), where a mass of Composition C-4 plastic explosive was detonated inside a confined container (Figure 2), both with and without a protective layer of water-filled reservoirs surrounding the explosive. A percent-pressure reduction (defined as unity less the ratio of the peak overburden pressure with a protective water jacket to the pressure without it) of approximately 50% was achieved by enveloping explosive charges with protective water jackets at a 2.5 water-explosive mass ratio. Similarly, the Naval Civil Engineering Laboratory blast tests performed by Malvar and Tancreto (1998) showed a reduction in both peak pressure and total impulse of about 90% when 4.67 lb of TNT was closely surrounded by twice its weight in water (Figure 2.6).

Prior investigations of water as a blast mitigation material have focused on placing water on top of live munitions in a confined environment (Absil and Bryntse 2006, Keenan and Wager 1992, Joachim and Lunderman 1997, Malvar and Tancreto 1998) or sprayed into closed quarters as a continuous mist (Adiga et al. 2009, Ananth et al. 2008, Schwer and Kailasanath 2005, Willauer et al. 2009), rather than the current proposal of a water layer placed on the structures to be protected as a external layer in an unconfined environment at a distance from the blast event. However, the thermodynamic and kinetic mitigation modes required for this proposal to be valid are identical to those demonstrated in these other applications. The theoretical basis for the use of water as a blast mitigation material is further discussed in chapter 3.

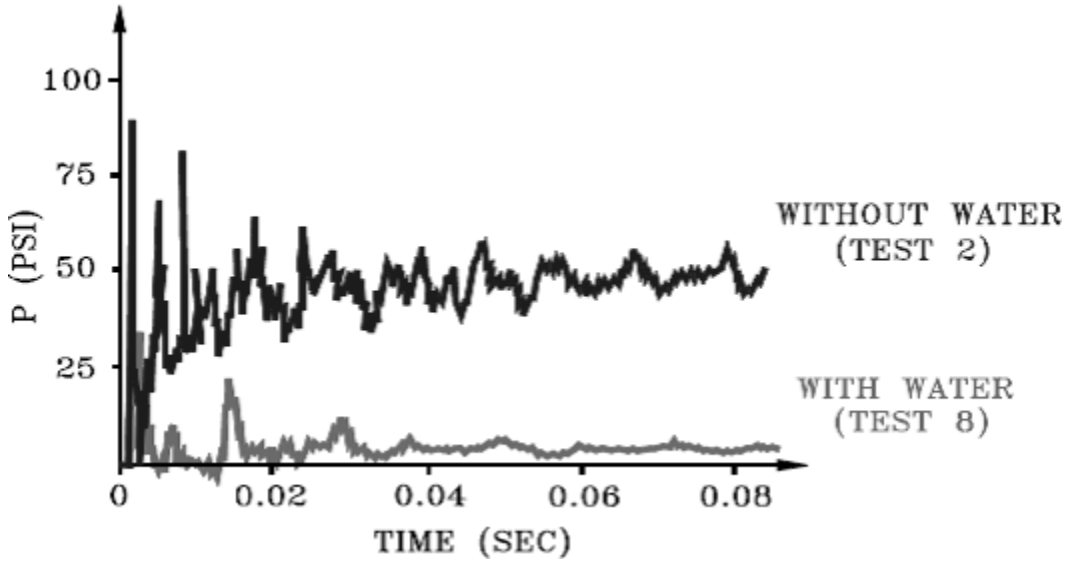

Figure 2.6 Comparison of of pressure history for explosives detonated with and without a surrounding layer of water (Malvar and Tancreto 1998).

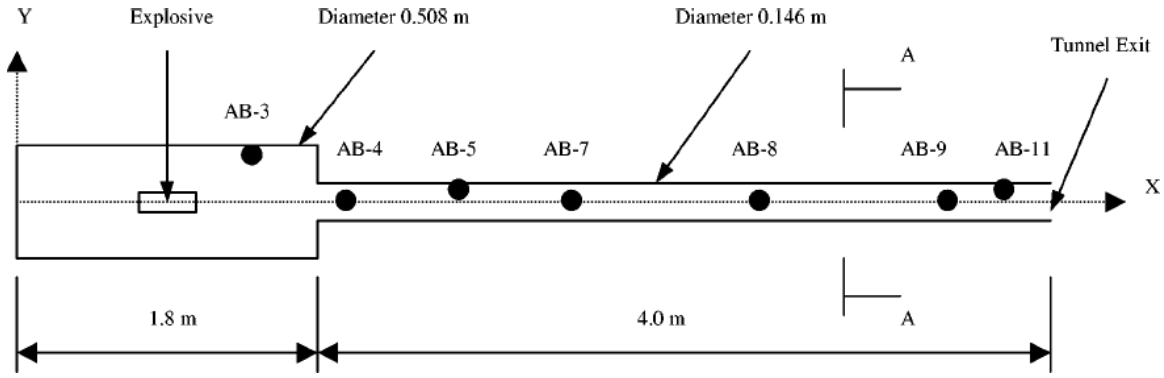

Figure 2.7 Confined blast chamber used to investigate the effect of surrounding explosives with water, used in experiments by Joachim and Lunderman (1997) and simulated by Chong et al. (1999).

2.4 Effect of Cross-Section Geometry on Blast Pressure

As a starting point for the design of the shape of the protective jacket, an analytical investigation of the effects of a column's cross-section geometry on the maximum resultant blast pressure caused by a free air blast was performed by Allahverdi (2010). Three basic cross-section shapes were considered: circular, square (sides orthogonal with blast) and "diamond" (square, rotated 45˚ from orthogonal). The circular cross-section has a diameter of 3.28 ft (1 m), while the two square cross-sections are both 3.28 ft × 3.28 ft (1 m × 1 m). Using the finite element analysis software AUTODYN (Figure 2.9), each cross section was subjected to the blast caused by 100 lb (45.4 kg) of TNT at a standoff of 6.56 ft (2.0 m), simulated with the using an Euler mesh (see Section 4.1.3) modeling the atmosphere surrounding the column. Reflected pressures were tracked over time at the gauge points *a* through *e* (Figure 2.8), and the impulses were calculated by taking the time integral of these pressures.

The shape and orientation of the cross-section has a significant effect on both pressure and impulse, as seen in Figure 2.10: for example, at the gage point *a* at the leading point of the cross-section, the square cross-section is subjected to an impulse of about 6.3 kPa · s, while the diamond cross-section undergoes a maximum impulse of approximately 4.6 kPa · s, a reduction of about 30%. At gage point *c*, the point furthest longitudinally from the standoff line, the diamond cross-section is briefly subjected to a higher maximum pressure than the square cross-section, but regardless, the total impulse on the diamond at the point is still less than half the total impulse on the square, an important result

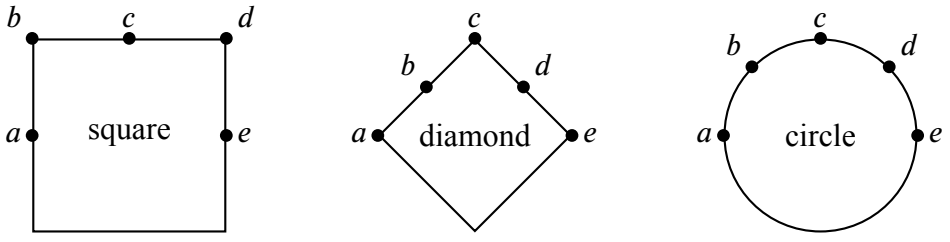

Figure 2.8 Locations of gauge points on column cross-sections.

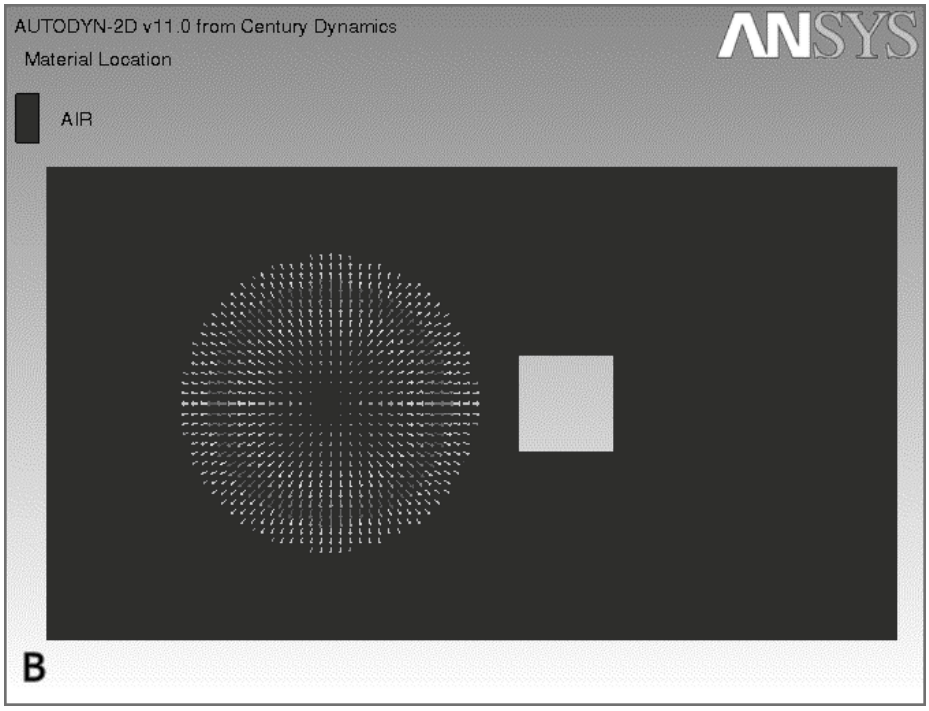

Figure 2.9 AUTODYN simulation in progress of blast on square column, showing the velocity of explosion products moments after detonation.

since the structural response of a structure is often more sensitive to total subjected impulse than to maximum transient pressure. The pressure and impulse at gage points *d* and *e* are negligible compared to those at the front and side of the column (Allahverdi 2010). The pressure and impulse reductions associated with the modified column geometry suggest that shaping the protective jacket into one with a leading edge, such as the stellate cross-section as proposed in Section 1.5 would reduce the pressure and impulse imparted to the underlying column further than using a jacket with a flat exterior.

These blast simulations, performed using a standard Euler mesh method, are compared to the use of an analytical method introduced in Section 8.1.

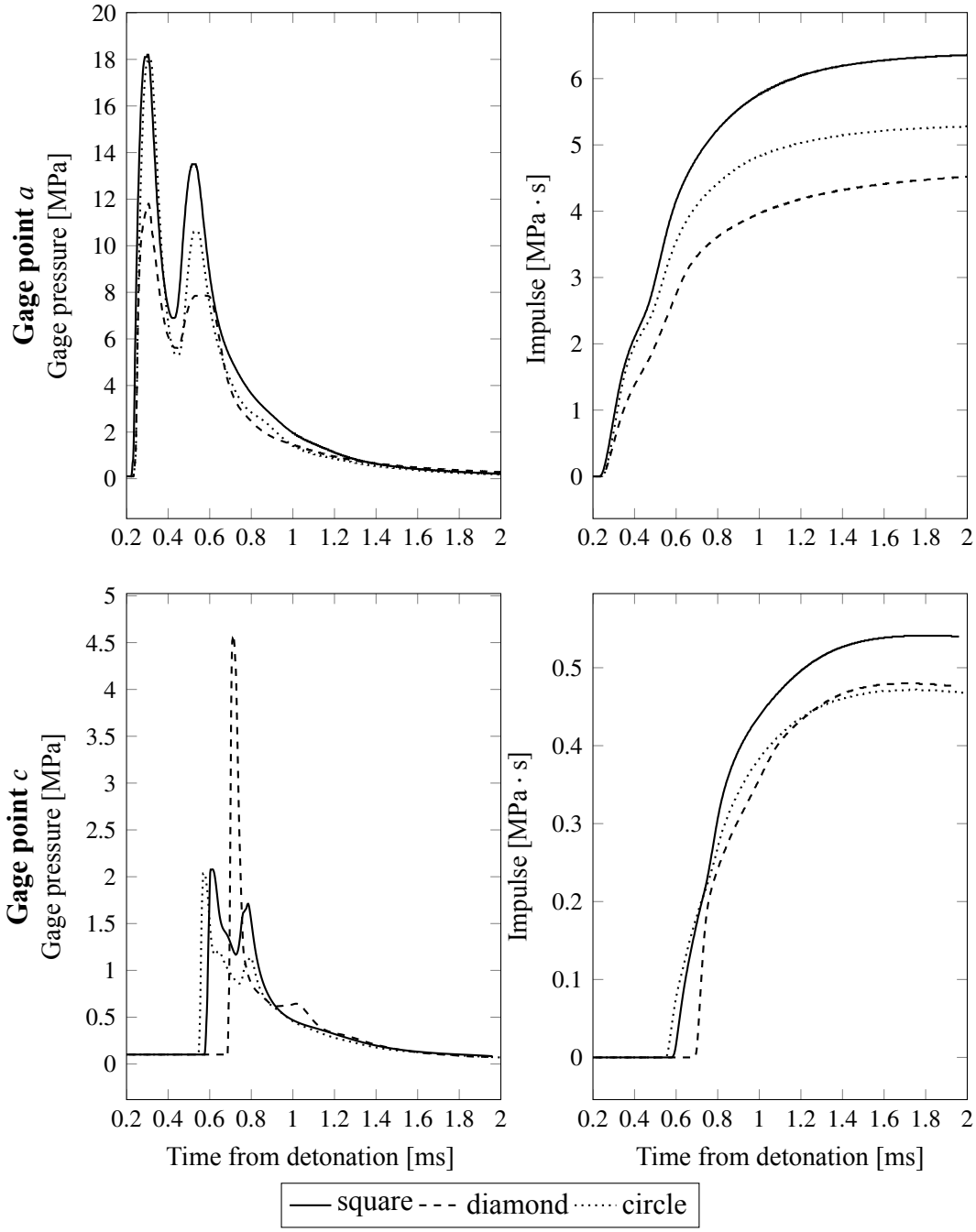

Figure 2.10 Example pressure and impulse histories at selected gage points for the three considered cross-section shapes.

CHAPTER 3

THEORETICAL ENERGY DISSIPATION MODES

In this chapter, the two theorized blast energy dissipation modes—the kinetic dissipation mode, where the energy of the blast is turned into the kinetic energy of the water, and the thermodynamic dissipation mode, where the energy of the blast is absorbed by and used to vaporize the water—are described. An example deployment of the protective jacket in the presence of various sizes of explosive devices is theoretically analyzed, demonstrating the high theoretical dissipative capacity of the protective jacket against typical hand-carried or vehicle-borne devices.

3.1 1-DOF Approximation of Dynamic Structural Loading

As an initial estimate of the effects of a sudden load on an elastic structural system, the system can be idealized by approximating it as a single degree-of-freedom (1-DOF) system consisting of a weight W falling from a height h onto a massless spring with stiffness $k = W/\Delta_{st}$ (where Δ_{st} is the deflection of the system under a static load of force W), subject to the following conservative assumptions:

1. The material properties (and thus, the spring stiffness k) are not significantly different during static and dynamic loading, a conservative assumption;
2. The system only deforms elastically, such that the displacement is linearly proportional to the applied forces, and local deformation is negligible,
3. The inertia of the structure during the impact event is negligible, and
4. All energy is conserved – the collision is perfectly inelastic and no energy is lost to friction, air resistance or damping.

When the spring reaches its maximum deflection of Δ_{max} and the instantaneous velocity of the weight is $v = 0$, the work done by gravity on the weight is equal to the work

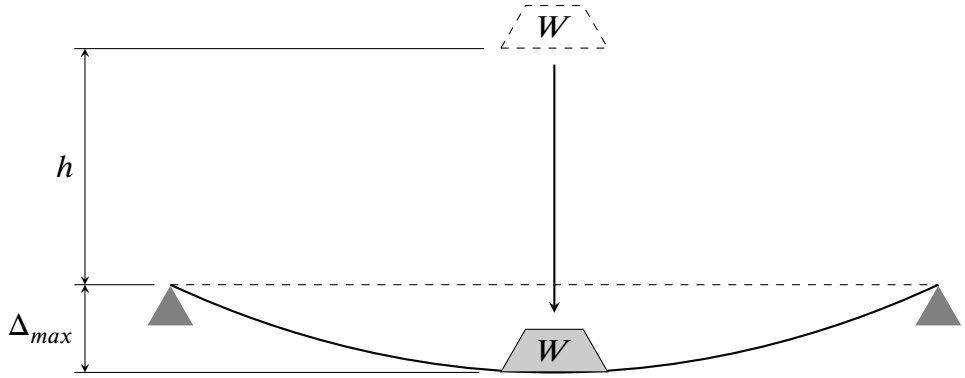

Figure 3.1 Schematic diagram of the single degree-of-freedom approximation.

performed to deform the spring, such that

$$W\left(h+\Delta_{max}\right)=\frac{k\Delta_{max}^2}{2} \tag{3.1}$$

Since $k = W/\Delta_{st}$, (3.1) is equivalent to

$$\begin{aligned}\Delta_{st}\left(h+\Delta_{max}\right) &= \frac{1}{2}\Delta_{max}^2\\ \frac{1}{2}\Delta_{max}^2-\Delta_{st}\Delta_{max}-h\Delta_{st} &= 0\end{aligned} \tag{3.2}$$

The relevant solution to the quadratic equation is

$$\begin{aligned}\Delta_{max} &= \Delta_{st}+\sqrt{\Delta_{st}^2+2h\Delta_{st}}\\ \therefore \Delta_{max} &= \Delta_{st}\left[1+\sqrt{1+\frac{2h}{\Delta_{st}}}\right]=A\Delta_{st}\end{aligned} \tag{3.3}$$

The deflection of the structure under an impact load can be considered the static deflection, magnified by a factor of $A(h,\ \Delta_{st}) = 1 + \sqrt{1 + 2h/\Delta_{st}}$ as found in equation (3.3). For a

height of $h = 0$, equivalent to a simple suddenly-applied load, $A = 2$, as expected for a quasi-static loading.

Since the structure's deflection is linearly proportional to the applied load, the maximum dynamic deflection can be found by calculating the structure's deflection under the magnified, dynamic-equivalent static load of $P_{eq} = AW$. This is a conservative upper bound of the dynamic deflection, since the impact is considered to be perfectly inelastic; a correction factor which accounts for the coefficient of restitution and any frictional forces could be found later experimentally or via simulation.

As an example, for the experimental setup described in Section 5.1, consisting of a 100 lb hammer falling $5'6''$ and striking a $\mathsf{W}\,6 \times 15$ steel beam of length $9'0''$ at mid-span, the magnification factor is thus

$$\begin{aligned}
\Delta_{st} &= \frac{WL^3}{48EI} \\
&= \frac{(110\text{lb})(9\,\text{ft} \times \frac{12\,\text{in}}{1\,\text{ft}})^3}{48(29 \times 10^6\,\text{psi})(29.3\text{in}^4)} \\
&= 0.0034\,\text{in} \\
A &= 1 + \sqrt{1 + \frac{2h}{\Delta_{st}}} \\
&= 1 + \sqrt{1 + \frac{66\,\text{in})}{(0.0034\,\text{in})}} \\
&= 198 \\
\Delta_{max} &= A\Delta_{st} = (198)(0.0034\,\text{in}) \qquad (3.4) \\
&= 0.67\,\text{in}\,[17.1\text{mm}]
\end{aligned}$$

Even for this simple case, the predicted effect of the impact load is a nearly two-hundredfold magnification of the static deflection, two orders of magnitude more than the doubling of deflection expected due to a suddenly applied load of equal weight.

The 1-DOF structure model can be extended to approximate the effects of blasts on structural elements; now, assuming that the source of the excitation is not a sudden imparting of energy due to impact, but a forcing described by the function

$$F(t) = \begin{cases} Ap_s^+ \left(1 - \frac{t}{t_0}\right) & 0 \le t \le t_0 \\ 0 & t < 0,\ t > t_0 \end{cases} \tag{3.5}$$

p_s^+	mean peak overpressure
t_a	time of arrival of blast wave
A	surface area exposed to blast

the graph of which is shown in Figure 3.2; from the figure, it is evident that the approximate impulse delivered by the simplified blast pulse is equal to $I = \frac{1}{2} A p_s^+ t_a$.

Assuming that damping is negligible over the short timespan of the simplified blast effect, but now that the excited mass of the structure is equal to m, the inhomogeneous ordinary differential equation of 1-DOF motion $m\ddot{x} + kx = F(t)$, where $x(t)$ is the deflection

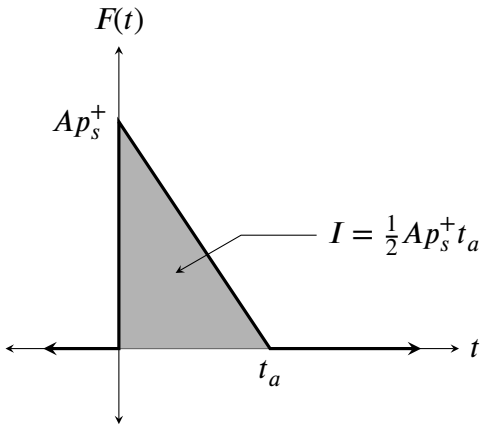

Figure 3.2 Simplified blast forcing function.

at midspan at time t, can be derived using Duhamel's convolution integral,

$$x(t) = \frac{1}{m\omega_n} \int_0^t F(\tau) \sin\left[\omega_n (t-\tau)\right] \, d\tau$$

to produce the piecewise equations for position and velocity of

$$x(t) = \begin{cases} \dfrac{Ap_s^+}{k}\left(1 - \cos\omega_n t\right) - \dfrac{Ap_s^+}{kt_0}\left(t - \dfrac{\sin\omega_n t}{\omega_n}\right) & 0 \le t \le t_a \\ \dfrac{Ap_s^+}{k}\left[\dfrac{\sin\omega_n t}{\omega_n t_a} - \dfrac{\sin\omega_n\left(t - t_a\right)}{\omega_n t_a} - \cos\omega_n t\right] & t \ge t_a \end{cases} \tag{3.6}$$

$$\dot{x}(t) = \begin{cases} \dfrac{Ap_s^+}{k}\left(\omega_n \sin\omega_n t + \dfrac{\cos\omega_n t}{t_a} - \dfrac{1}{t_a}\right) & 0 \le t \le t_a \\ \dfrac{Ap^+}{k}\left[\dfrac{\cos\omega_n t}{t_a} - \dfrac{\cos\omega_n\left(t - t_a\right)}{t_a} + \omega_n \sin\omega_n t\right] & t \ge t_a \end{cases} \tag{3.7}$$

where $\omega_n = \sqrt{k/m}$ is the natural frequency of the system.

3.2 The "Kinetic Mode" of Dissipation

A number of prior experimental studies (Absil and Bryntse 2006, Eriksson 1974, Eriksson and Vretblad 1994, Joachim and Lunderman 1997, Keenan and Wager 1992) explored the ability of a mass of water placed around stored explosive devices to reduce the pressure and impulse on the surrounding structure during an accidental detonation, such as the investigation by Keenan and Wager (1992) of a "water blanket" which could be spread over or suspended above pallets of ordnance in storage, to significantly reduce the peak pressure and impulse generated by an accidental detonation, due to the energy absorption required to move and break up the water. As the leading edge of the blast wave reaches the boundary of the water's container, the disruption caused by the blast wave and the disintegration of the

container causes the water to be accelerated, breaking it into fast-moving droplets (Ananth et al. 2008).

3.3 The "Thermodynamic Mode" of Dissipation

Once the water has been accelerated and fragmented by the blast, its capability to dissipate energy via evaporation is greatly enhanced. The enthalpy of vaporization of water is 2.25 MJ/kg; that is, one kilogram of liquid water at 100 °C and 1 atm pressure requires the addition of 2.25 MJ of energy to completely transition into the vapor state. In terms of volume, a 30 cm × 30 cm × 15 cm layer of water (i.e. approximately one square foot of wall, protected by a 6 inch thick layer) would ideally be able to absorb through phase change

$$(30\,\text{cm})^2\,(15\,\text{cm})\left(\frac{1\,\text{L}}{1000\,\text{cm}^3}\right)\left(\frac{1\,\text{kg}}{1\,\text{L}}\right)\left(\frac{2.25\,\text{MJ}}{1\,\text{kg}}\right) = 30.38\,\text{MJ}$$

and assuming that the water was initially at about 70 °F (about 20 °C), to reach vaporization temperature, would absorb an additional energy of

$$(30\,\text{cm})^2\,(15\,\text{cm})\left(\frac{1\,\text{L}}{1000\,\text{cm}^3}\right)\left(\frac{1000\,\text{g}}{1\,\text{L}}\right)\left(4.186\,\frac{\text{J}}{\text{g}\cdot\text{K}}\right)(80\,\text{K}) = 4.52\,\text{MJ},$$

a total of 34.90 MJ.

The droplets initially formed by the kinetic mode's dispersal process–about 1 mm to 5 mm in diameter–are further fragmented via "bag breakup" (Figure 3.3), where individual droplets are flattened and deformed into a thin, concave semispheroid shell (Pilch and Erdman 1987, Zhao et al. 2011), the rupture of which forms an ultra-fine mist (UFM) of droplets approximately 20 μm to 30 μm across (Adiga et al. 2009). Assuming the droplets are roughly spherical, the total surface area of the ultra-fine mist generated from the dissi-

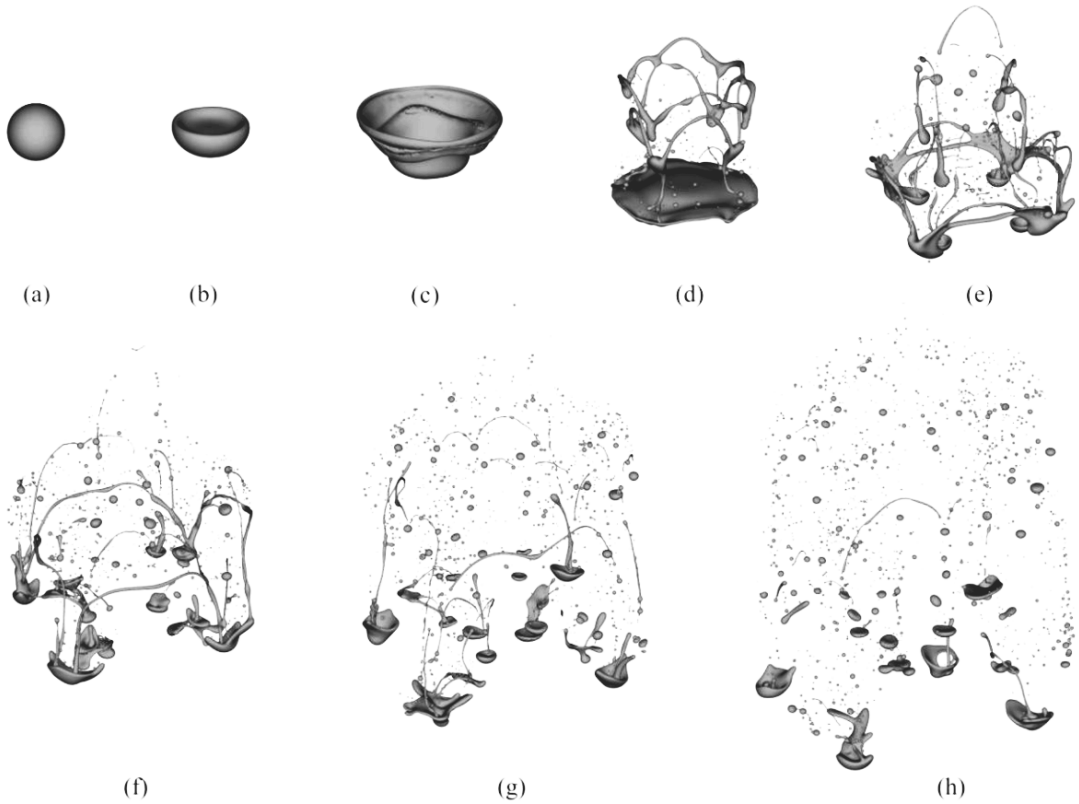

Figure 3.3 Droplet undergoing bag breakup (Jalaal and Mehravaran 2012).

pation and breakup of the 6 inch thick layer can be calculated:

$$\begin{aligned}
V_{layer} &= (30\,\text{cm})^2\,(15\,\text{cm}) \\
&= 0.0135\,\text{m}^3 \\
V_{droplet} &= \frac{4}{3}\pi\left(\frac{25\,\text{m}}{2}\right)^3 \\
&= 8181\,\text{m}^3 = 8.181\times10^{-15}\,\text{m}^3 \\
A_{droplet} &= 4\pi\,(25\,\text{m})^2 \\
&= 1963\,\text{m}^2 = 1.963\times10^{-9}\,\text{m}^2 \\
\frac{V_{layer}}{V_{droplet}}\cdot A_{droplet} &= \frac{1.35\times10^{-2}\,\text{m}^3}{8.181\times10^{-15}\,\text{m}^3}\cdot 1.963\times10^{-9}\,\text{m}^2 \\
&= 3240\,\text{m}^2
\end{aligned} \tag{3.8}$$

The surface area available for heat absorption is increased about $3240\,\mathrm{m}^2/(0.3\,\mathrm{m})^2 = 36\,000$ times by the breakup process. While some energy is necessary to aerosolize the water, the surface energy of water is $0.072\,\mathrm{J/m}^2$ at typical atmospheric temperature, so the energy necessary for the mechanical breakup process is at most $\left(3240\,\mathrm{m}^2\right)\left(0.072\,\mathrm{J\,m}^{-2}\right) = 0.233\,\mathrm{kJ}$, a very small fraction of the vaporization capacity, so this energy absorption capacity is negligible compared to evaporation.

Due to the extremely transitory nature of blast events, the question remains of whether these droplets could properly evaporate in the time-scale necessary to maximize their energy absorption. From Adiga et al. (2009), the time necessary for a single droplet of water to evaporate can be determined using the equation

$$t_{vap} = \frac{d_0^2 \rho}{8\Gamma_{vap} \ln\left(1 + \frac{m_{vap}}{1 - m_{vap}}\right)}. \tag{3.9}$$

t_{vap}	evaporation time (s)
d_0	initial diameter of the droplet (m)
ρ	density of liquid water ($1000\,\mathrm{kg/m}^3$)
Γ_{vap}	water vapor exchange coefficient ($2.6 \times 10^{-5}\,\mathrm{kg/(m \cdot s)}$)
m_{vap}	mass fraction of water vapor at the droplet surface (≈ 0.95)

The calculated time necessary for a range of droplet sizes typically found in an ultrafine water mist to evaporate completely is shown in Figure 3.4. The average UFM droplet will evaporate completely in under one millisecond, well within the typical $< 10\,\mathrm{ms}$ time scale of a typical blast event, according to Adiga et al. (2009).

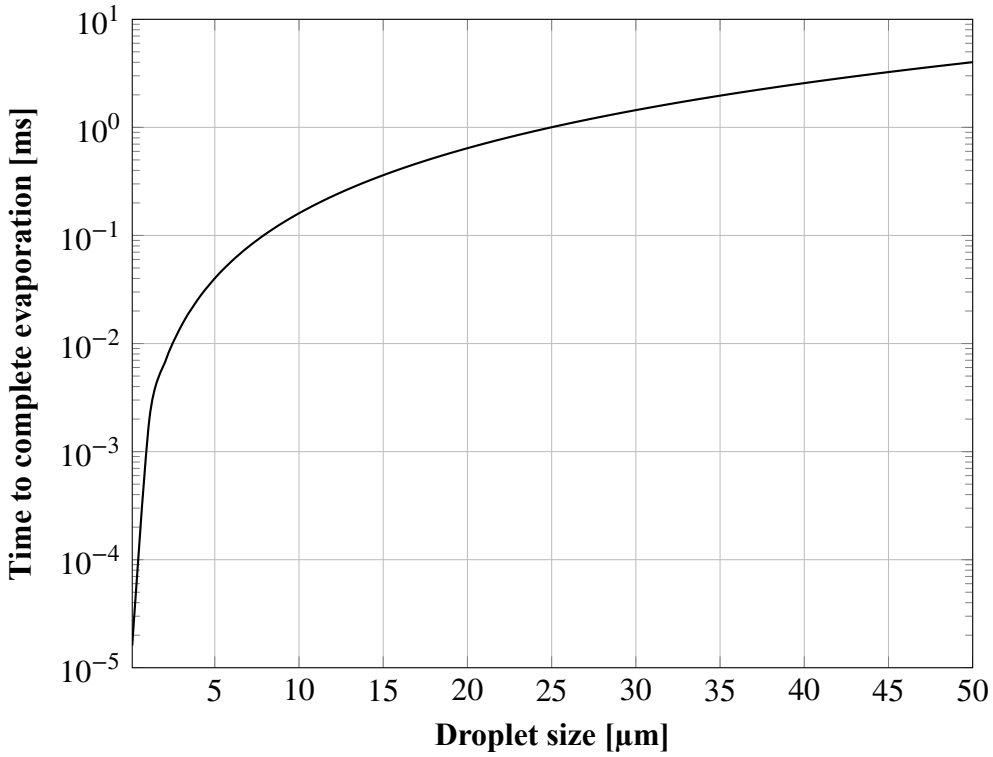

Figure 3.4 Time necessary for various droplet sizes to evaporate completely, calculated using equation 3.9 on the previous page.

3.4 Theoretical Capacity of the Protective Layer

Assuming an open-air, ground level explosion in front of a relatively large (practically semi-infinite) wall with no significant barriers or obstructions nearby (i.e. no increase in over-pressure caused by confinement or reflected shock waves), the amount of energy per unit surface area the wall is subject to can be estimated by assuming the energy is evenly distributed across the entirety of a hemispherical wave front centered on the explosive, and computing the ratio of the total energy released in the explosion to the area of the hemisphere which makes up the leading pressure wave.

As an example demonstrating the ablative potential of the thermodynamic mode, if a 5 kg TNT bomb–an average-sized backpack bomb–with an explosive energy of approximately 4.5 MJ/kg is placed at ground level 2 m from a targeted structure and detonated, when the leading edge of the blast wave reaches the structure, the total area of the hemi-

sphere centered on the bomb is

$$\frac{1}{2}\left[4\pi(2\,\mathrm{m})^2\right] = 25.1\,\mathrm{m}^2 \tag{3.10}$$

and the approximate energy per unit area of the leading wave is

$$\frac{0.7\,(5\,\mathrm{kg})\,(4.5\,\mathrm{MJ/kg})}{25.1\,\mathrm{m}^2} = 0.63\,\frac{\mathrm{MJ}}{\mathrm{m}^2} \tag{3.11}$$

For this example, the blast energy inflicted per unit area of the wall is equivalent to only about 2% of the ideal capacity of the protective layer to absorb energy via the enthalpy of vaporization, not including the energy required to disperse the water or heat the water from ambient temperature to its boiling point. Only a small fraction of the water would need to be vaporized in this manner to sufficiently blunt the effect of the explosion, even in a situation where the reflection of shock waves caused up to a thirteen-fold amplification of the peak pressure (FEMA 2003).

Various combinations of explosive size and standoff are compared to the theoretical heat of vaporization capacity of a 6 in and a 3 in thick protective layer in Figure 3.5; from these results, even a modestly-sized layer of water placed over a structural member would theoretically have the capacity to protect against even relatively large, vehicle-borne-size explosive devices when considering the combined effect of kinematic dissipation and heat absorption.

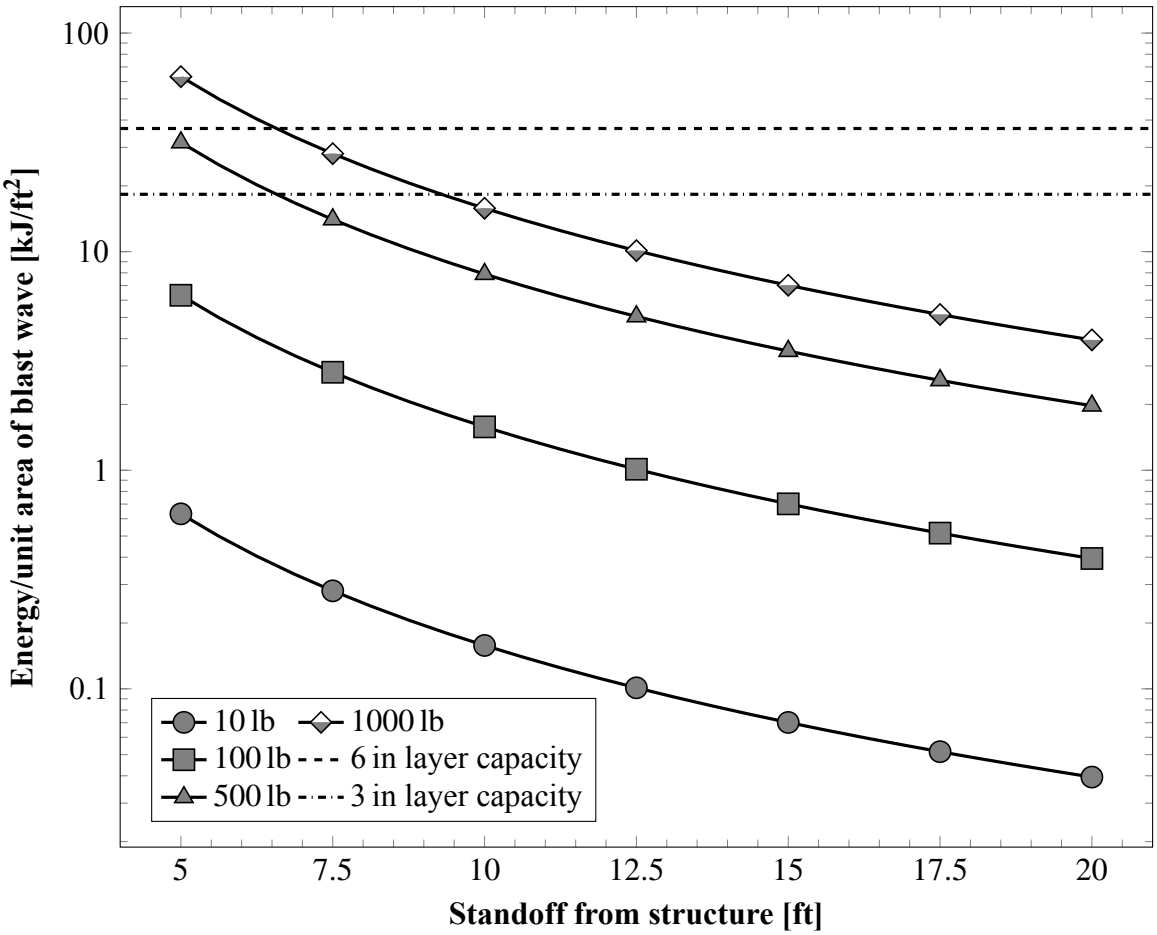

Figure 3.5 Blast energy per unit area of blast wave vs. standoff from structure for varying explosive device sizes, compared to theoretical capacity of protective layer to dissipate energy via heat capacity and enthalpy of vaporization.

CHAPTER 4

FINITE ELEMENT SOLVER METHODS AND MATERIAL MODELS

This chapter provides a brief overview of the formulation and motivation behind the finite element solver methods and material models employed in the following chapters to numerically analyze the effectiveness of the protective jacket system.

4.1 Finite Element Solver Methods

4.1.1 General Mesh-Based Formulation Motivation

Consider an arbitrary body occupying a known volume V bounded by the surface Γ, in a rectangular coordinate frame with axes x_1, x_2 and x_3, composed of many particles X_1, X_2, … , X_N at initial locations $\mathbf{x}_{1\cdot0}$, $\mathbf{x}_{2\cdot0}$, … , $\mathbf{x}_{N\cdot0}$, which is subjected to some combination of boundary conditions, displacements and external forces over a span of time $t = [0, T]$. If one wishes to determine the equilibrium position $\mathbf{x}_{n\cdot t} = \chi\left(X_n, t\right) = \mathbf{x}_{n\cdot0} + u\left(X_n, t\right)$ of each particle in the volume at given time increments Δt, $2\Delta t$, ..., T, two complementary approaches exist for formulating the analysis:

- Track the movement of each individual element in the body relative to the coordinate frame such that the body obeys the principle of virtual displacements, the material or *Lagrangian* formulation, or
- Track the motion of the material as it passes through fixed control volumes such that the flow through each control volume obeys the principle of virtual velocities, the spatial or *Eulerian* formulation (Bathe 1996).

4.1.2 Lagrange Formulation

In the explicit Lagrangian formulation of finite element analysis, the body is discretized using a mesh which is attached to the volume; no matter how the body is deformed or displaced, a mesh point tracks the same particle of the material. Because the discretization

tracks the particle motion directly, in the Lagrangian formulation, the velocity and acceleration of each mesh point are

$$\begin{aligned} \mathbf{v}\left(X_n, t\right) &= \frac{\partial \mathbf{x}_{n\cdot t}}{\partial t} \\ \mathbf{a}\left(X_n, t\right) &= \frac{\partial^2 \mathbf{x}_{n\cdot t}}{\partial t^2} \end{aligned}$$

The deformation gradient $\mathbf{F}$ is the Jacobian matrix of the element coordinates $\mathbf{x}_{n\cdot t}$ with respect to the original coordinates $\mathbf{x}_{n\cdot 0}$, such that in three spatial dimensions (Bathe 1996),

$$\mathbf{F} = \frac{\partial (x_i)_{n\cdot t}}{\partial (x_j)_{n\cdot 0}} = \begin{bmatrix} \frac{\partial (x_1)_{n\cdot t}}{\partial (x_1)_{n\cdot 0}} & \frac{\partial (x_1)_{n\cdot t}}{\partial (x_2)_{n\cdot 0}} & \frac{\partial (x_1)_{n\cdot t}}{\partial (x_3)_{n\cdot 0}} \\ \frac{\partial (x_2)_{n\cdot t}}{\partial (x_1)_{n\cdot 0}} & \frac{\partial (x_2)_{n\cdot t}}{\partial (x_2)_{n\cdot 0}} & \frac{\partial (x_2)_{n\cdot t}}{\partial (x_3)_{n\cdot 0}} \\ \frac{\partial (x_3)_{n\cdot t}}{\partial (x_1)_{n\cdot 0}} & \frac{\partial (x_3)_{n\cdot t}}{\partial (x_2)_{n\cdot 0}} & \frac{\partial (x_3)_{n\cdot t}}{\partial (x_3)_{n\cdot 0}} \end{bmatrix}$$

the determinant of which is equal to the volumetric strain, such that as per the conservation of mass,

$$\rho \det \mathbf{F} = \rho_0$$

and the conservation of momentum can be expressed as

$$\rho a_i = \frac{\partial \sigma_{ij}}{\partial x_j} + \rho f_i$$

where $\boldsymbol{\sigma}$ is the Cauchy stress tensor and f_i is the body force on the element along the ith axis. Similarly, the internal energy of a given element is given by

$$\rho \frac{\partial E}{\partial t} = \sigma_{ij} \frac{\partial \epsilon_{ij}}{\partial t} + \rho f_i v_i$$

4.1.3 Euler Formulation

In the Euler formulation, rather than being used to discretize a body, the Euler mesh is a fixed mesh which forms a series of control volumes which the body passes through in a manner which satisfies conservation of mass, momentum and energy. In terms of the Euler formulation, assuming no exterior sources or sinks of material, the conservation of mass is

$$\frac{\partial \rho}{\partial t} = -\nabla \cdot (\rho \mathbf{v})$$

conservation of momentum is

$$\frac{\partial}{\partial t}(\rho \mathbf{v}) + \nabla \cdot (\mathbf{v} \otimes \rho \mathbf{v}) = -\nabla P,$$

and conservation of energy is

$$\frac{\partial}{\partial t}(\rho E) + \nabla \cdot [\mathbf{v}(\rho E + P)] = 0,$$

where E is the total energy in the control volume and P is the static pressure in the control volume (ANSYS Inc. 2011).

4.1.4 Arbitrary Lagrange-Euler Mesh (ALE)

The arbitrary Lagrange-Euler formulation method is a synthesis of the material and spatial mesh formulations. Lagrange formulations are ideal for modeling the free-surface deformation of bodies undergoing moderate strain, but are very sensitive to local mesh deformation and mesh tangling in very high strain regions, and cannot automatically generate new damaged surfaces in bodies which undergo material failure. Conversely, Euler formulations

have a fixed mesh allows for the automatic generation of failure surfaces but is not sensitive to deformation, requiring that local material response must be found with a very fine mesh, which can be unduly computationally expensive (ANSYS Inc. 2011).

As a balance between the two formulations, the ALE formulation consists of alternating Lagrange timesteps and "advection steps", where the mesh is incrementally rezoned by adjusting the positions of the nodes of distorted elements, and the current material solution variables are transported to the adjusted mesh (Donea et al. 1982, Hallquist 1998).

4.1.5 Mesh-free Smoothed Particle Hydrodynamics

An alternate approach to the traditional mesh-based finite element methods is the smoothed particle hydrodynamics (SPH) method. Unlike Euler, Lagrange or ALE methods, SPH does not require either a body mesh or a control volume mesh, which eliminates the need for geometric erosion to correct for excessively deformed meshes or the need to model the volume where material will eventually flow but does not initially exist. Rather, it represents bodies as a set of particles associated with freely-moving interpolation points, allowing the calculation of material properties between them through the use of a weighting function averaging the contribution of all nearby surrounding particles. Because of these advantages, SPH formulations are especially more efficient for problems which involve the large deformations of fluids and granular materials.

The value of the generic material property A at location $\mathbf{x}$ in a body represented by SPH particles, where n particles are within a distance of $2h$ of $\mathbf{x}$, is found with the sum

$$A(\mathbf{x}) = \sum_{j=1}^{n} m_j \frac{A_j}{\rho_j} \cdot W\left(\left|\mathbf{x} - \mathbf{x}_j\right|, h\right)$$

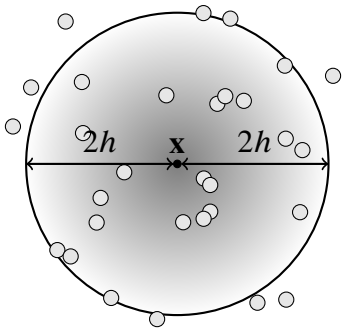

Figure 4.1 Representation of interpolation smoothing radius.

m_j	mass associated with particle j
A_j	material property of particle j
ρ_j	density associated with particle j
W	kernel function
$\mathbf{x}_j$	location of particle j
h	smoothing radius over which the property is averaged

AUTODYN's formulation of SPH uses for its kernel function the cubic spline

$$W(d) = \frac{2}{3h} \cdot \begin{cases} 1 - \frac{3}{2}d^2 + \frac{3}{4}d^3 & 0 \le q \le 1 \\ \frac{1}{4}(2-d)^3 & 1 \le d \le 2 \\ 0 & d > 2 \end{cases}$$

where d is the normalized distance $\left|\mathbf{x} - \mathbf{x}_j\right| / h$. This kernel function, graphically represented in Figures 4.1 and 4.2, will only include particles within a radius of $2h$ in its interpolation, with a higher weight placed on particles nearer the location **x**.

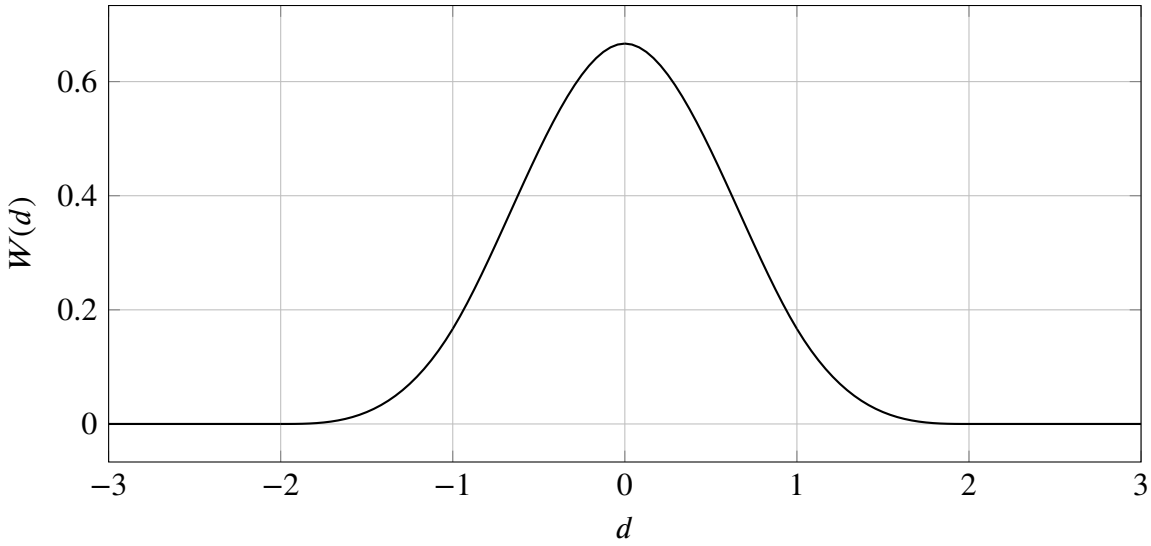

Figure 4.2 Cubic kernel function $W(d)$ used in smoothed-particle hydrodynamics material properties interpolation.

4.2 Equations of State

4.2.1 Ideal Gas Equation of State

The ideal gas equation of state is one of the most basic constitutive material models, derived from the three basic ideal gas laws as $pV = nRT$, or, in terms of the ratio of specific heats $\gamma = \frac{c_P}{c_V}$, specific volume v and bulk internal energy E, $pv = (\gamma - 1)\, E$. From Zukas and Walters (1998), if the isentropic condition

$$\left(\frac{\partial E}{\partial v}\right)_S = -p$$

is applied to the ideal gas equation of state, then

$$p = -\frac{v}{\gamma - 1} \cdot \frac{\mathrm{d}p}{\mathrm{d}v} + \frac{p}{\gamma - 1}$$

which, when integrated, gives

$$\frac{p}{p_0} = \left(\frac{v_0}{v}\right)^{\gamma}.$$

Applied to the Gibbs equation

$$T\,\mathrm{d}S = C_v\,\mathrm{d}T + T\left(\frac{\partial p}{\partial T}\right)_v \mathrm{d}v$$

the entropy change in an ideal gas is found to be

$$\Delta S = R \ln \frac{v}{v_0}\left(\frac{T}{T_0}\right)^{1/\Gamma}$$

The ideal gas equation of state assumes that gas particles are infinitesimally small, making it only a good approximation for locations in a gas where the particles are very far apart compared to their molecular radii. While this is not a valid assumption for the dense gas at high pressure near the center of an explosion, the ideal gas equation of state can be used in lieu of a more intricate model once the gas has reached a large expansion ratio of about 10 times its original volume (Century Dynamics 2005).

4.2.2 Polynomial Equation of State

The polynomial equation of state, based on the Mie-Gruneisen equation of state describing the relationship between pressure and volume of a shock-compressed solid, models the pressure-volume relationship as two empirically-determined polynomials, one cubic polynomial for compression and one quadratic polynomial for tension:

$$\begin{cases} p = A_1\mu + A_2\mu^2 + A_3\mu^3 + \left(B_0 + B_1\mu\right)\rho_0 e & \mu \geq 1 \\ p = T_1\mu + T_2\mu^2 + B_0\rho_0 e & \mu \leq 1 \end{cases}$$

μ	compression ratio $\frac{\rho}{\rho_0}$
ρ_0	density at zero pressure
$A_1, A_2, A_3, B_0, B_1, T_1, T_2$	empirical material constants

4.2.3 Two-Phase Equation of State

The two-phase equation of state is a formulation that describes the thermodynamic behavior of water when it solely exists in the liquid or gas phase as well as when the two phases co-exist in the form of steam (Morgan 1984). While this equation of state only represents the behavior of water at densities lower than 1.0 g/mL (i.e., when the water is expanding), this equation of state can be paired with a second EOS, like the polynomial equation of state or one based on the Rankine-Hugionot shock relations (ANSYS Inc. 2011).

The Hugionot, the saturation curve and the phase boundaries in the P–v plane define three regions of interest—single-phase regions for liquid and vapor water above the saturation curve, and the two-phase region below it (figure 4.3). In the single-phase regions, the water's behavior is calculated using a typical Gruneisen EOS equation,

$$P = p_r(v) + \frac{\Gamma(v)}{v}\left(e - e_r(v)\right)$$

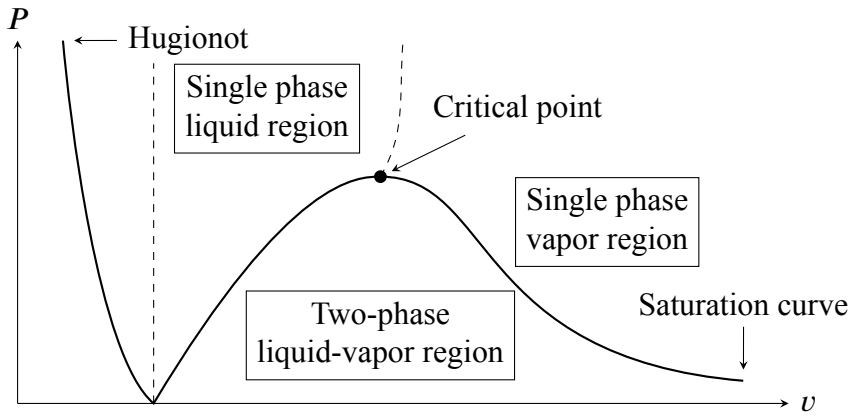

Figure 4.3 Regions of interest for two-phase EOS.

where the functions $p_r(v)$, $e_r(v)$ and $\Gamma(v)$ are calculated by interpolating between provided tabular data from the original paper by Morgan (1984). In the two phase region, the specific volume and internal energy of the phase mixture is defined in terms of the mass fraction of vapor α and the individual known phase properties v_g, v_l, e_g and e_l taken from the saturation curve as

$$\begin{aligned} v &= \alpha v_g + (1-\alpha) v_l \\ e &= \alpha e_g + (1-\alpha) e_l \end{aligned}$$

which may be rewritten implicitly without α as

$$\frac{v - v_g}{v_g - v_l} = \frac{e - e_g}{e_g - e_l}$$

4.2.4 Jones-Wilkins-Lee Equation of State

The Jones-Wilkins-Lee (JWL) equation of state is used to simulate the behavior of high explosives–substances which may undergo a chemical change over a very short timescale that releases a large amount of energy. This chemical change can be idealized as a discontinuity traveling through the high explosive, where the unreacted material detonates instantaneously as the shock wave passes through it, releasing its energy and transforming into the products of detonation.

Using the Rankine-Hugionot relations to quantitatively describe the conservation of mass, energy and momentum across the discontinuity, the detonation velocity D of the high explosive (the speed at which the discontinuity travels through the material), the particle

velocity u and the change in specific internal energy $E - E_o$ are found to be

$$D = \sqrt{v^2 \cdot \left(\frac{p - p_o}{v_o - v}\right)} \tag{4.1}$$

$$u = \sqrt{(p - p_o)(v_o - v)}$$

$$E - E_o = Q + \frac{1}{2}(p + p_o)(v_o - v) \tag{4.2}$$

v	specific volume of the detonation products
v_o	specific volume of the unreacted high explosive
p	pressure of the detonation products
p_o	pressure of the unreacted high explosive
E	specific internal energy of the detonation products
E_o	specific internal energy of the unreacted high explosive
Q	exothermic energy released by the detonation

For a set of initial pressure and specific volume conditions and a given detonation velocity, equation (4.1) provides the Rayleigh line, the linear relationship between all the possible states of pressure and volume which conserve mass and momentum and are consistent with the detonation velocity. Equation (4.2) describes the Hugoniot curve, the set of all pressure and velocity conditions which the detonation products may achieve from the undetonated high explosive at its initial pressure and velocity.

The Chapman-Jouget point (p_1, v_1), the point at the intersection of the Hugoniot curve and the Rayleigh line which uniquely determines the detonation velocity, can be found

by minimizing the derivative dp_1/dv_1 over the Hugoniot curve, producing the relationships

$$\begin{aligned} v_1 &= v_o \cdot \tfrac{\gamma}{\gamma+1} \\ p_1 &= \tfrac{D^2}{v_o(\gamma+1)} = (\gamma+1)\,\rho_o u_1^2 \\ E_1 &= Q + E_o + \left(\tfrac{D}{\gamma+1}\right)^2 \\ \gamma &= \left[-\tfrac{\partial \ln p_1}{\partial \ln v_1}\right]_S \end{aligned}$$

γ adiabatic exponent at the Chapman-Jouguet point

E_1 specific internal energy at the Chapman-Jouguet point

Using the Chapman-Jouguet (CJ) point to determine the behavior of the p–v relationship near (p_1, v_1), as well as providing correction terms that empirically model the experimentally-measured expansion of the detonation products at certain critical pressures, the combined adiabats which govern the Jones-Wilkins-Lee equation of state (Lee and Hornig 1968) are of the form

$$p = A\left(1 - \frac{v_0\omega}{vR_1}\right)e^{-R_1 v_o/v} + B\left(1 - \frac{v_o\omega}{vR_2}\right)e^{-R_2 v_o/v} + \frac{\omega}{v}e \tag{4.3}$$

$A,\ B,\ R_1,\ R_2,\ \omega$ empirical constants for a given explosive

This equation of state is valid for pressures higher than 0.1 MPa and lower than "significantly above the CJ value" (ANSYS Inc. 2011); for standard TNT, the Chapman-Jouget pressure is $p_1 = 18\,700$ MPa (Coleburn 1964). This range covers the expected behavior of typical explosive devices well; the peak pressures in blast simulations in later chapters are in the range of 0.75 MPa to 29 MPa, and below the lower limit of 0.1 MPa, the mix of product gases and atmosphere can be represented instead by the ideal gas equation of state.

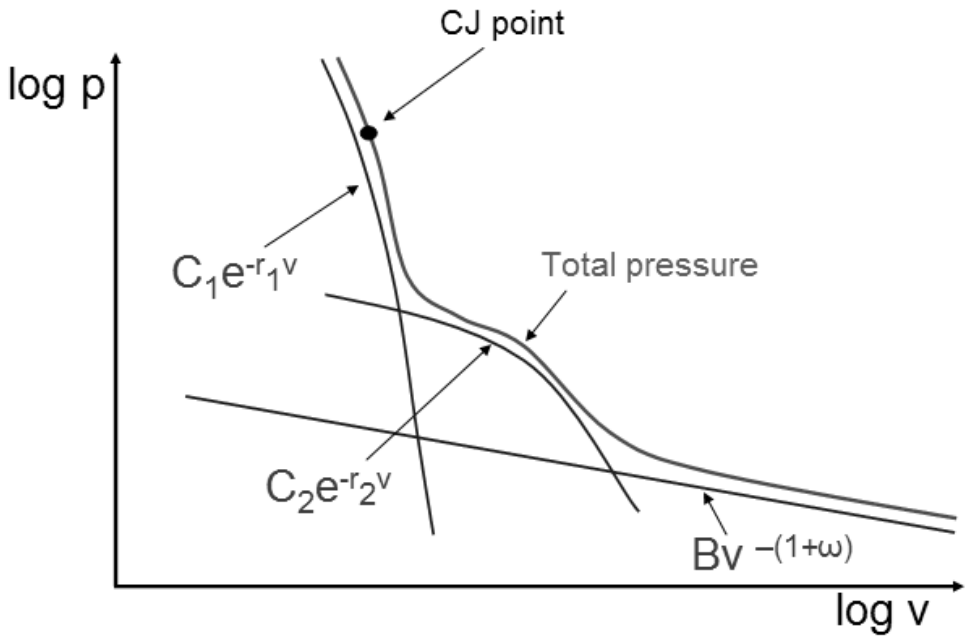

Figure 4.4 Contribution of various terms in the JWL equation to the total adiabatic pressure (ANSYS Inc. 2011).

4.2.5 Modified $P-\alpha$ Equation of State

The modified $P-\alpha$ equation of state is an augmentation of other equations of state used to model the behavior of porous materials undergoing compaction; the model is driven by the assumption that the specific internal energy of the porous material is constant for all densities; the porosity coefficient $\alpha = \upsilon/\upsilon_s$ is the ratio of the current specific volume to the specific volume of the completely compacted material. For a porous material with an equation of state defined as a function of specific volume and energy, such that $p = f(\upsilon, e)$, the modified $P-\alpha$ form of the equation of state will be $p = f^{\star}\left(\frac{\upsilon}{\alpha}, e\right)$. The modified $P-\alpha$ equation of state is equivalent to the standard EOS when $\alpha = 1$; that is, when the material is fully compacted and all pores have been crushed. The porosity is further defined as a function of pressure, the form of which depends on the specific material under consideration.

4.3 Strength Models

4.3.1 RHT Concrete Strength and Failure

The Riedel-Hiermaier-Thoma (RHT) model is a constitutive model which accounts for the increased shear strength under compression, strain hardening and strain rate hardening, and the third invariant dependence relationship between compression and tension behavior characteristic of brittle materials, while also tracking the effects of shear damage on material strength and the local failure that occurs over the course of a numerical analysis.

The general form of the limiting failure surface is

$$f\left(P, \sigma_{eq}, \theta, \dot{\varepsilon}\right) = \sigma_{eq} - Y_{TXC}\left(P\right) \cdot F_{cap}\left(P\right) \cdot R_3\left(\theta\right) \cdot F_{rate}\left(\dot{\varepsilon}\right)$$

P	normalized pressure, as a ratio of actual pressure to cylinder strength f_c'
σ_{eq}	deviatoric stress tensor
θ	Lode angle of the yield surface, where $\sin 3\theta = -\frac{3\sqrt{3}}{2}\frac{J_3}{J_2^{3/2}}$
J_2, J_3	second and third invariants of the deviatoric stress
$\dot{\varepsilon}$	strain rate tensor
Y_{TXC}	fracture surface relationship
F_{cap}	porosity effect coefficient
R_3	Willam-Warnke third invariant dependence surface relationship
F_{rate}	strain hardening relationship

Three failure surfaces are used by the RHT model to describe the behavior of a brittle material: the compressive strength relationship $Y_{TXC}\left(P\right)$, the rate factor $F_{rate}\left(\dot{\varepsilon}\right)$ and the invariant-dependent tension-compression relationship $R_3\left(\theta\right)$. The failure surface is then modified by a coefficient to represent the reduction in strength during porous compaction.

The RHT model is linear elastic until it reaches the plastic state, where strain damage begins to accumulate; the Johnson–Holmquist damage accumulation coefficient D is

the ratio of the sum of all previously experienced strains to the experimentally determined failure strain $\epsilon_{f,p}$, such that $D = 0$ represents undamaged, unstrained material, and $D = 1$ represents complete material failure. The accumulated damage reduces the fracture surface from Y_{TXC} to $(1 - D)\, Y_{TXC} + DY_{residual}$, where $Y_{residual}$ is the remaining strength of completely damaged material (Borrvall and Riedel 2011, Brannon and Leelavanichkul 2009, ANSYS Inc. 2011).

4.4 Boundary Conditions

4.4.1 Lagrange Transmit Boundary

The *Transmit* boundary in AUTODYN (also known as the impedance boundary condition in other finite element packages) allows for shock waves to be transmitted across the boundary of a body without reflecting at the material discontinuity. The shock wave behaves as if it continues to travel into a region of identical material on the opposite side of the boundary. This enables the approximate but more efficient simulation of shock waves in large bodies, by modeling the small region around the immediate area subject to shock and applying transmit boundaries along the cut planes.

4.4.2 Euler Flow Out Boundary

By default, the exterior surface of a Euler grid is modeled as a rigid, non-slip and impermeable boundary. Applying the *Flow Out* boundary to a region of the surface allows material within the Euler grid to travel into dummy elements outside the grid, removing the material from the actual Euler region; this is useful for reducing the size of the Euler region and reducing the time spent simulating material that has traveled out of the area of interest of the simulation.

4.4.3 Analytical Blast Boundary

A feature added to version 14 of ANSYS AUTODYN, the Analytical Blast boundary condition allows for the simulation of blast pressure loads on three-dimensional volume elements

caused by high explosive detonations, using the methods presented in the U.S. Army Technical Manual Fundamentals of Protective Design (Department of the Army 1986). The analytically-determined blast pressures and times of arrival, the same as those calculated by the blast analysis software package CONWEP, correspond well to those calculated by explicit finite element methods (Schwer et al. 2008). Using this boundary condition, the surfaces of a structure subject to blast can be "painted" with the Analytical Blast boundary condition and analyzed without needing to separately calculate the atmospheric pressures around the structure or set up a Lagrange-Euler interaction between the solid and the surrounding atmosphere.

The pressure applied to a given face depends on its scaled distance $Z = RW^{-1/3}$ from the blast center and the angle of incidence θ of the face (the angle between the face's surface normal vector and the vector connecting the center of the face to the blast center). From Z and θ, the peak incident pressure P_I, total head-on reflected impulse I_R and total incident impulse I_I are computed using the standard Kingery-Bulmash polynomial fit equations for open-air TNT blasts shown in Figure 4.6. The peak reflected pressure is found using the angle of incidence peak reflected pressure coefficient $C_{r\theta}$ relations in Figure 4.6, while the reflected impulse for oblique faces is found in terms of the incident impulse I_I and the reflected impulse I_R with the equation

$$I = I_I \left(1 + \cos\theta - 2\cos^2\theta\right) + I_R \cos^2\theta$$

The applied blast pressure function $P(t)$ is then calculated to be

$$P(t) = C_{\theta r} P_{so} \left(1 - \frac{t - t_a}{t_o}\right) \cdot e^{\lambda_R (t - t_a)/t_o} \tag{4.4}$$

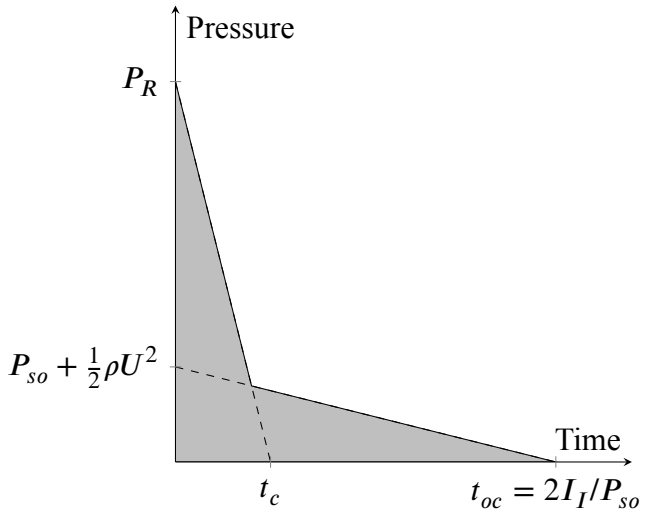

Figure 4.5 Fictitious pressure vs. time curve used to calculate the reduced impulse due to clearing effects.

P	applied blast load at time t
$C_{\theta r}$	peak reflected pressure coefficient
P_{so}	peak incident pressure
t_a	time of arrival
t_o	duration of overpressure phase
λ_R	decay parameter, chosen to set $\int_{t_a}^{t_a+t_o} P(t)\ \mathrm{d}t = I$

If it is enabled in the boundary condition settings, the applied blast boundary can be set to correct for the effects of *clearing* near the structure's edges, the reduction in reflected pressure caused by part of the blast wave propagating around and past the edges (Razaqpur et al. 2007). The clearing time $t_c = 3L/U$, where L is the distance to the nearest valid edge at which clearing can occur and U is the calculated Kingery-Bulmash shock front velocity; this clearing time is used to construct a fictitious pressure-time curve (Figure 4.5), the integral of which is the clearing-modified impulse I_c. The modified impulse is used to calculate λ_R in Equation 4.4.

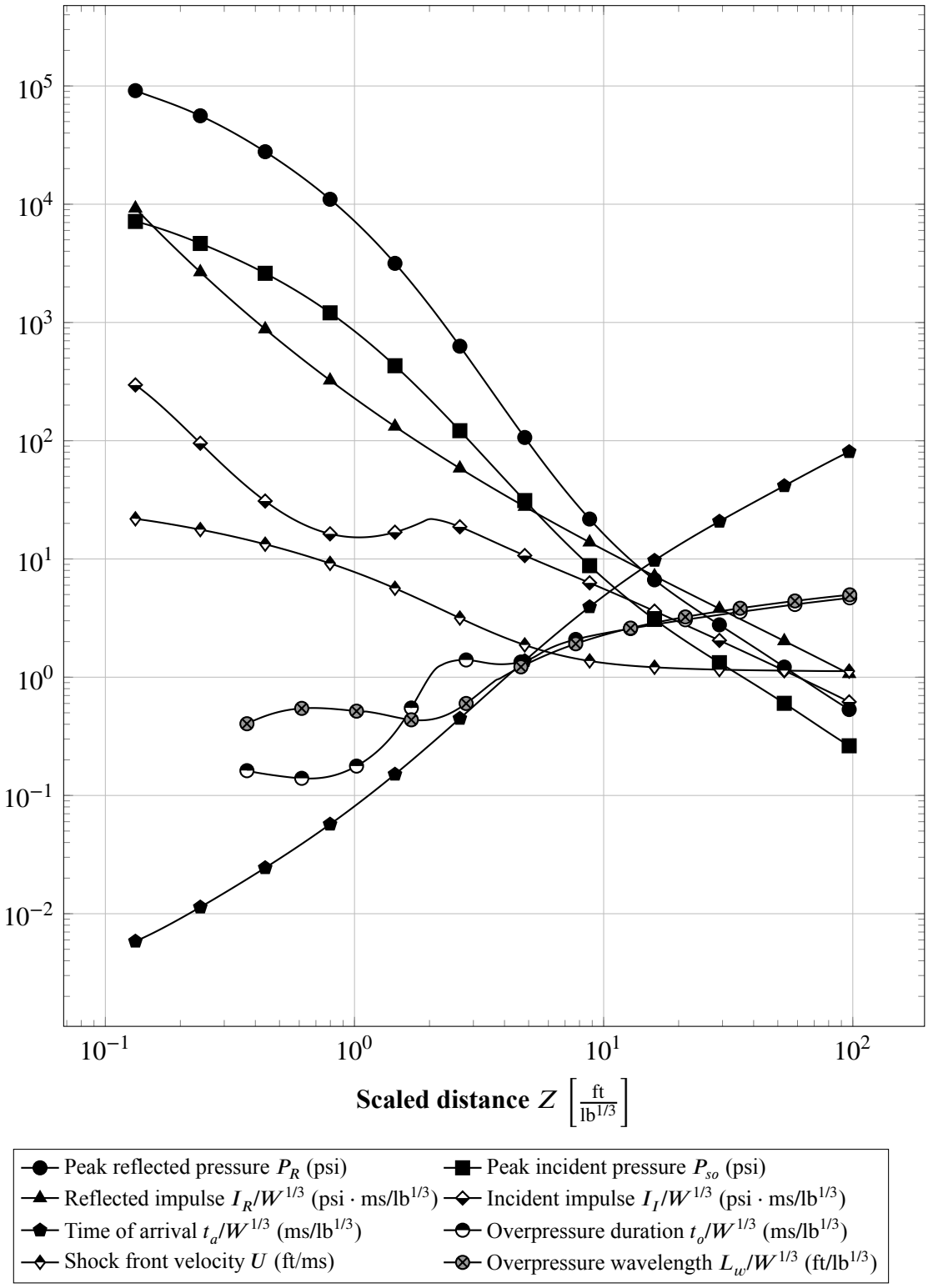

Figure 4.6 Kingery-Bulmash equations for blast parameters for a spherical TNT explosion in free air at standard atmospheric pressure, adapted from Figure 2-7 in UFC 3-340-02 (Dalton et al. 2008).

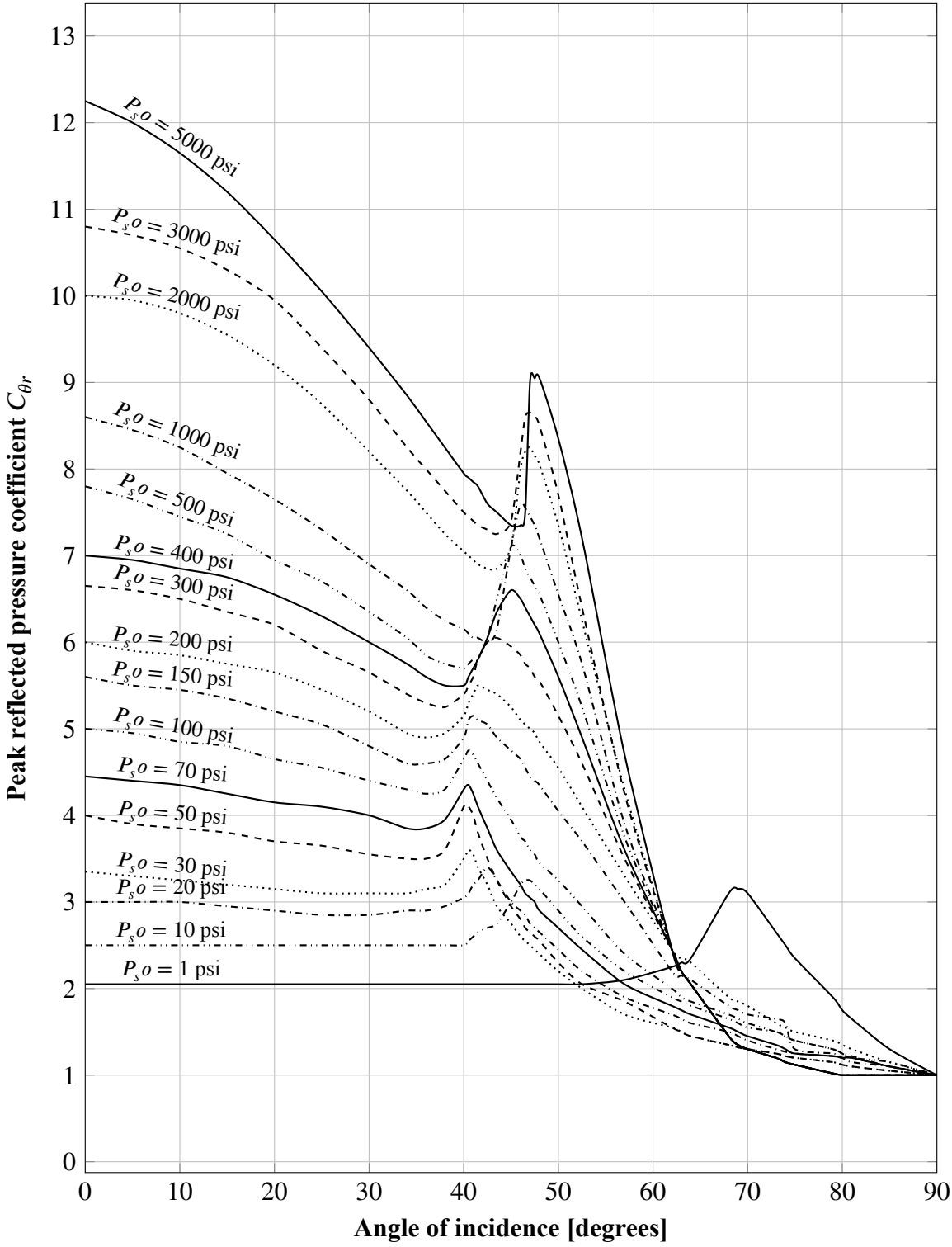

Figure 4.7 Reflected scaled peak pressure versus angle of incidence of blast, adapted from Figure 2-193 from UFC 3-340-02 (Dalton et al. 2008).

CHAPTER 5
INITIAL LABORATORY EXPERIMENTS

In this chapter, the laboratory experiments which provided the groundwork for the current research are recounted and discussed. Of note are the kinetic energy dissipation tests performed at NJIT, which measured the reduction in deflection of a protected beam subjected to an impact load at midspan, and the qualitative blast tests at Picatinny Arsenal which provided a limited but illustrative demonstration of the protective jacket's capacity to protect fragile structural elements from live blasts.

5.1 Qualitative Kinetic Energy Dissipation Tests

5.1.1 Initial Proof-of-Concept Tests

As a rough proof-of-concept experiment to explore the kinetic dissipation mode, the first laboratory tests, performed in December 2007 in the construction engineering technology laboratory at NJIT, qualitatively evaluated the effects of an impact from a falling drop-hammer (Figure 5.1a) on a stack of clay tiles protected by a commercial plastic storage bag filled with water (Figure 5.1b).

The stack of tiles without the protective water layer exhibited severe fragmentation (Figure 5.1c), while the protected stack fractured into relatively few pieces (Figure 5.1d), exhibiting less damage than the unprotected stack. This promising result led to the need to study the jacket's effect in a more rigorous manner.

5.1.2 Impact Testing Setup

The testing rig used for the following quantitative impact tests, which took place in the structural engineering laboratory at NJIT, consisted of a W 6×15 structural steel beam that was installed on a pair of floor-mounted supports set 9 ft apart (Figure 5.2), one unconstrained laterally to produce the "pinned-roller" end conditions required to make the beam

(a) Hammer with sample in place

(b) Protective layer on clay tiles

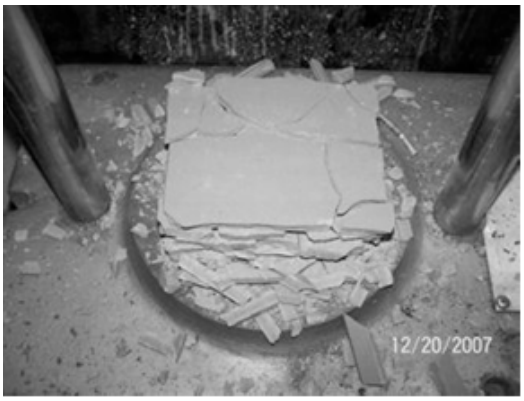

(c) Unprotected tiles after impact

(d) Protected tiles after impact

Figure 5.1 Proof-of-concept test setup and results.

structurally determinate. A 100 lb (45 kg) drop hammer mounted on vertical rails was installed above the beam's midpoint; thanks to a modification to the length of its uprights since the initial proof-of-concept tests, the weight could be raised 5.5 ft (1.67 m) above the beam's top flange.

The beam was fitted with a set of four strain gages and one direct-current linear displacement transducer (DC LVDT); the strains and displacements are measured by a Vishay Micro-Measurements System 6100 data acquisition system at a rate of 10 000 measurements per second per sensor. The System 6100 is operated using Vishay StrainSmart data acquisition and analysis software installed on a connected Windows PC (Figure 5.3). Initially, the System 6100 was set up to save the recorded data 0.5 s before and 1.0 s after the strain at the midpoint exceeds the expected static strain the beam would undergo if the hammer

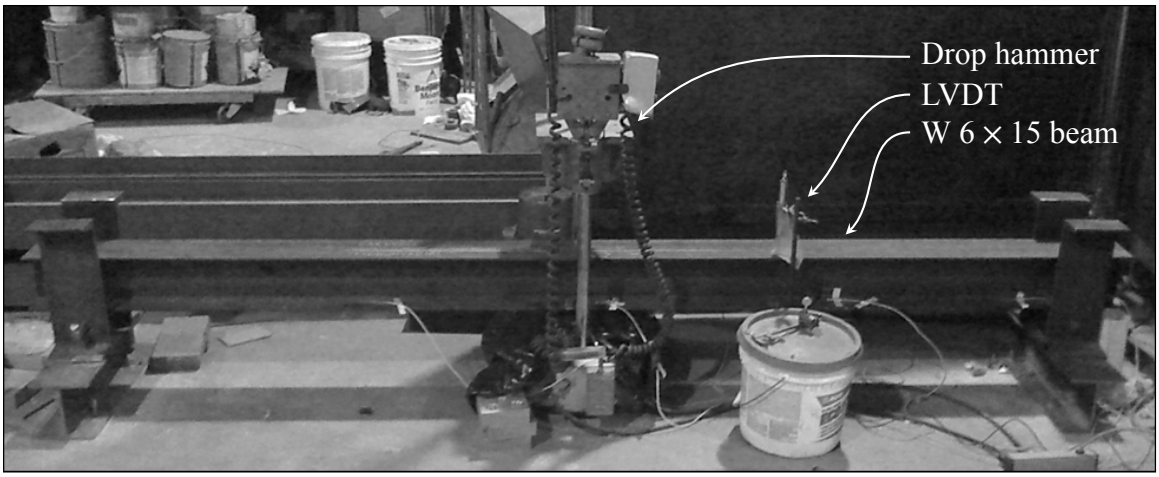

Figure 5.2 Completed impact testing setup.

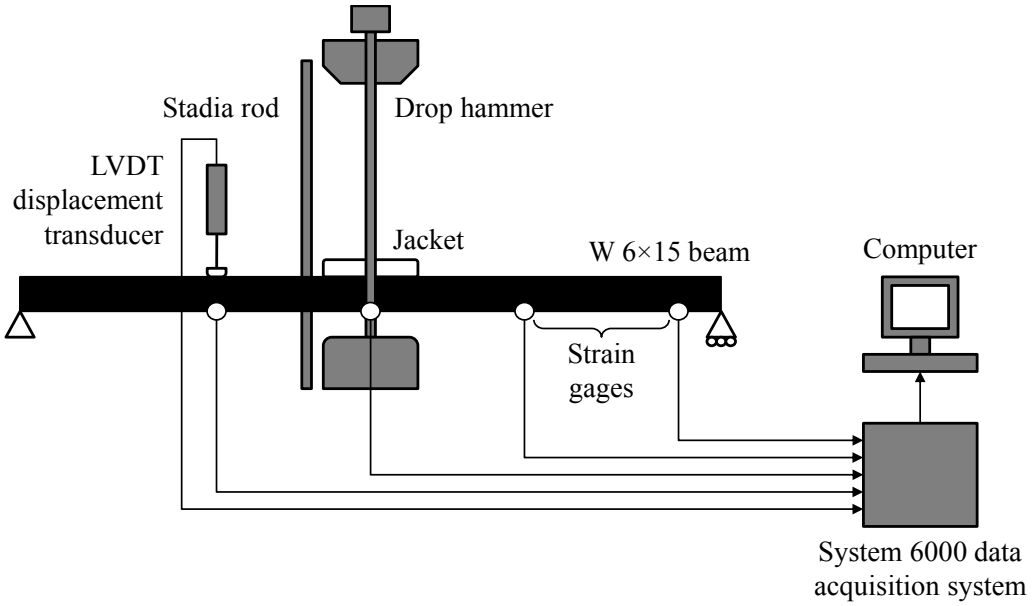

Figure 5.3 Schematic of impact testing setup (not to scale).

weight were placed statically on the beam. Through trial and error, this trigger condition was found to be sufficient to record the behavior of the beam during the impact event.

5.1.3 Initial Qualitative Beam Impact Tests

To test the beam after it was mounted but before the System 6100 arrived, a set of basic qualitative tests were performed using the beam impact rig. Three ½" jackets, composed of thermally sealed polyethylene bags containing the filler materials then under considera-

(a) Control rebound: 4.5 in

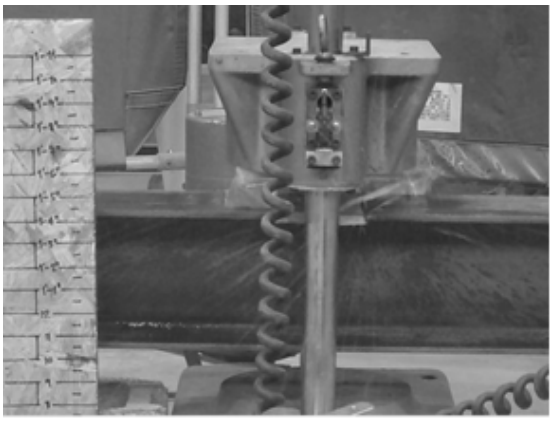

(b) Water rebound: 1 in

(c) Vermiculite rebound: 6 in

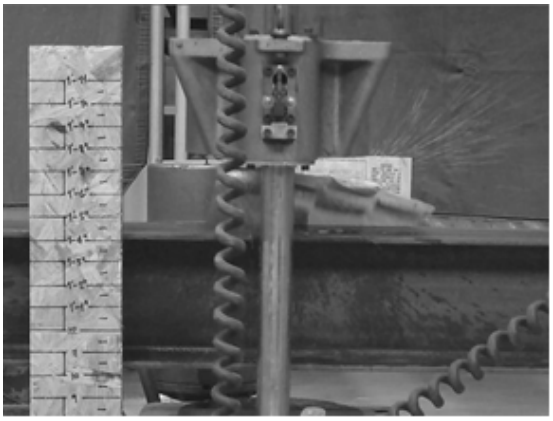

(d) Bentonite rebound: 3.5 in

Figure 5.4 Maximum hammer rebound for various jacket filler materials.

tion (water, bentonite powder and vermiculite granules), were tested. A hand-held digital camera was used to capture video of each impact event, and the video was analyzed to obtain an estimate of the maximum rebound height of the hammer (an approximation of the energy remaining in the beam-hammer system). The approximate rebound heights and corresponding video frames are shown in Figure 5.4.

From these initial results, it was decided that since neither the vermiculite nor the bentonite was able to reduce the rebound of the hammer as well as the water did, future experimentation would focus solely on water as the attenuation material.

5.2 Quantitative Kinetic Energy Dissipation Tests

5.2.1 First Beam Impact Tests

Once the instrumentation had been installed on the impact testing rig, the first set of tests were performed in March 2009. Six 8 in × 8 in (20.3 cm × 20.3 cm) protective jackets with a thickness of 3/8 in (1 cm) were assembled by pouring 13.5 oz (400 ml) of water into a 8 in × 10 in (20.3 cm × 25.4 cm) polyethylene bag, then partially sealing the top opening with a thermo-sealing device and leaving a small gap through which the excess air was mechanically expelled before completing the seal. Each of these jackets was then tested on the impact testing rig, and the maximum deflection of the beam LVDT during each impact event was recorded. Six control tests without a protective jacket, numbered C1 through C6, were also performed.

Of the six trials on the jackets, only four could be used; test E1 did not correctly trigger the System 6000's automatic data collection, and a second test was fouled when the hammer snagged on the guide cable on the way down, bursting the jacket but not hitting it at the same velocity as in the other tests. The maximum deflection recorded by the LVDT for both sets of trials are shown in Table 5.1, and example deflection records for two selected trials are shown in Figure 5.5. In the presence of the water-filled jacket, the beam deflection at the LVDT is about 18% smaller than without it.

Table 5.1 Maximum Recorded Deflection at LVDT for First Impact Tests

Test	$\Delta_{LVDT\cdot max}$ [mm]	Test	$\Delta_{LVDT\cdot max}$ [mm]
C1	5.59	E1	No measurement
C2	4.80	E2	No measurement
C3	5.55	E3	4.37
C4	4.74	E4	4.50
C5	5.91	E5	4.29
C6	4.95	E6	4.32
Mean	**5.27**	**Mean**	**4.37**

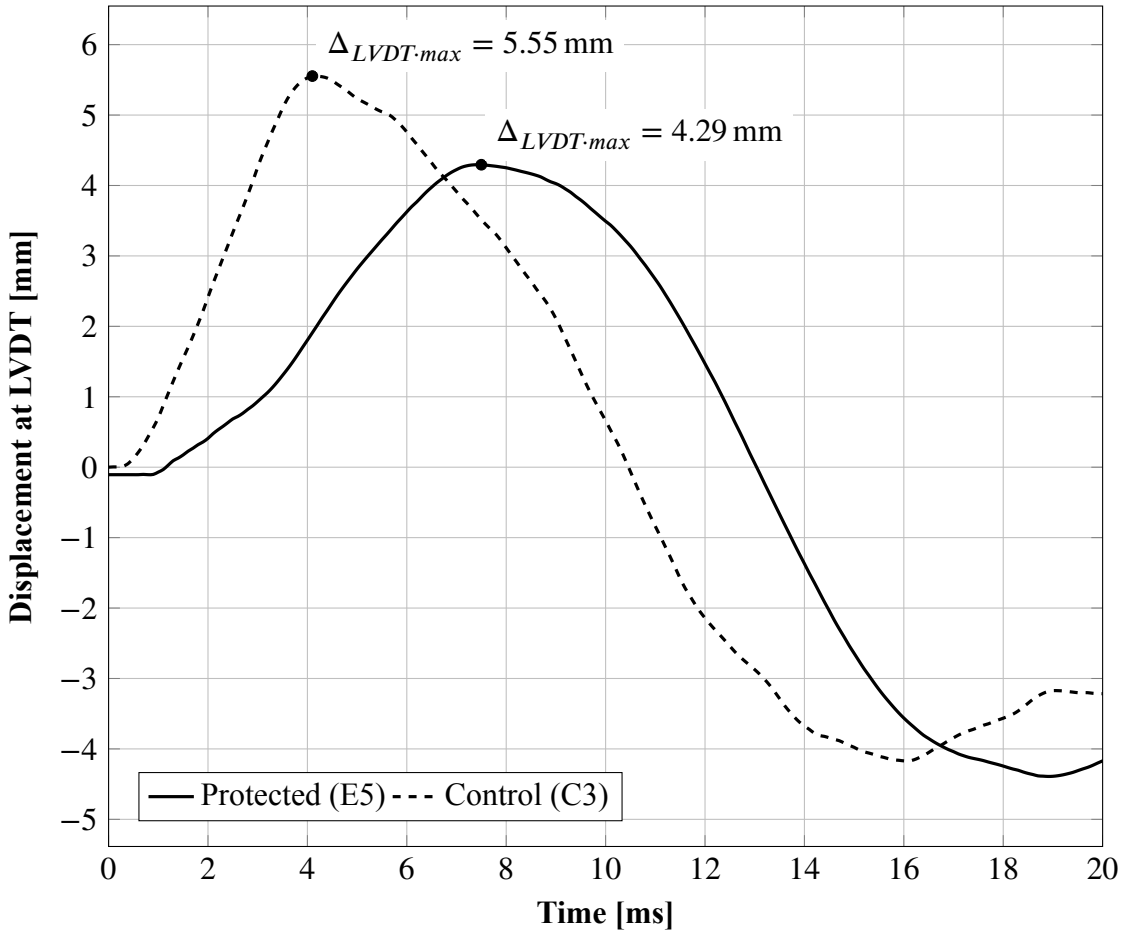

Figure 5.5 Comparison of measured deflection for selected unprotected and protected cases in first impact tests.

5.2.2 Second Beam Impact Tests

The second set of tests, performed in September 2009, added a video camera and a surveyor's stadia alongside the hammer to the instrumentation on the beam, to measure the maximum rebound height of the hammer as well as the beam deflection, with both taken together as a measure of the total energy remaining in the system that was not dissipated by the jacket. Eighteen impact tests were performed and recorded on video—three impacts each on the beam protected by jackets with volumes of 200 mL, 400 mL, 600 mL, 800 mL and 1000 mL, as well as three control impacts on the unprotected beam—with the tests otherwise being performed as they were in the first series of impact tests. The beam deflections and hammer rebound heights are summarized in Tables 5.2 and 5.3, and Figures 5.7 and 5.8.

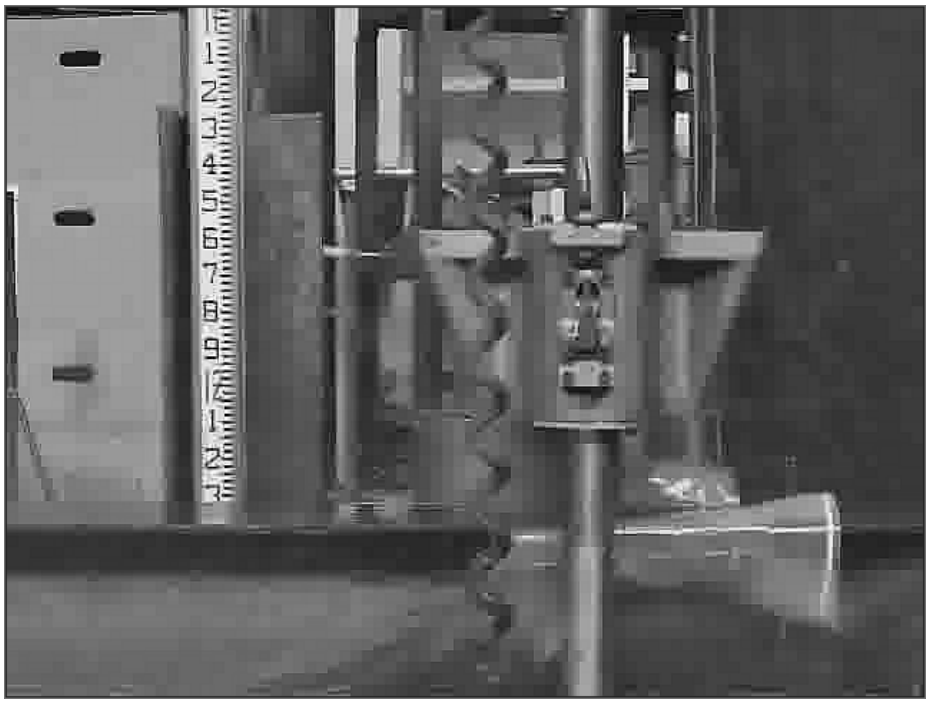

Figure 5.6 Frame from video taken during beam impact tests of hammer rebounding from beam protected by 1000 ml jacket.

Table 5.2 Maximum Recorded Deflection at LVDT for Second Impact Tests

	Deflection			
Volume [mL]	**Run 1 [mm]**	**Run 2 [mm]**	**Run 3 [mm]**	**Avg. deflection [mm]**
0 ml	5.39	5.62	5.48	5.50
200 ml	[a]	4.56	4.41	4.49
400 ml	4.29	4.22	4.24	4.25
600 ml	4.17	3.88	4.01	4.02
800 ml	3.88	3.79	3.75	3.81
1000 ml	3.68	3.39	3.68	3.58

[a] No clear maximum deflection was measured for this run

Table 5.3 Maximum Recorded Hammer Rebound for Second Impact Tests

	Rebound			
Volume [mL]	**Run 1 [mm]**	**Run 2 [mm]**	**Run 3 [mm]**	**Avg. rebound [mm]**
0 ml	201	174	195	190
200 ml	128	143	140	137
400 ml	119	91	98	103
600 ml	107	85	98	97
800 ml	85	73	82	80
1000 ml	76	70	82	76

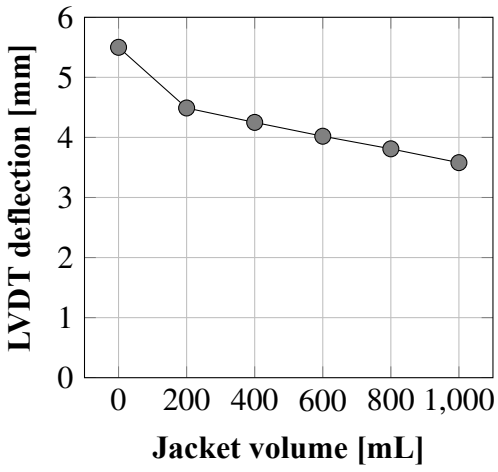

Figure 5.7 Average maximum deflection at LVDT vs. volume for second impact tests.

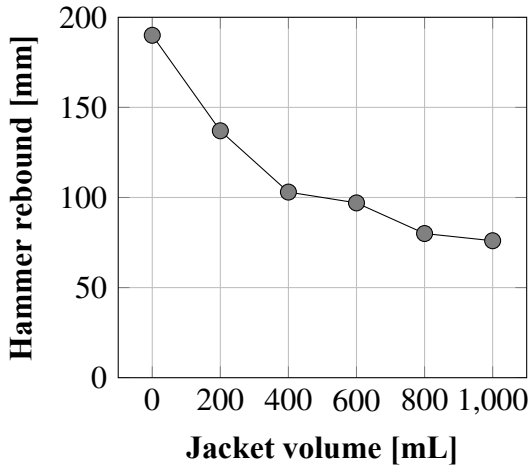

Figure 5.8 Average maximum hammer rebound vs. volume for second impact tests.

5.3 Live Blast Tests

5.3.1 Quantitative Peak Pressure and Time-of-Arrival Tests

Obtaining accurate measurements of explosive blast pressures is important for the development of realistic computer simulations that can be used to perform design refinement and testing. CONWEP, a conventional weapon effect calculation tool provided by the US Army Corps of Engineers Protective Design Center (2012), calculates blast pressures and times of arrival (the time elapsed between detonation and the arrival of the leading blast wave) for a given mass of explosive and standoff distance, but for this project, it was desired to compare these published CONWEP values with pressures measured in the field.

Blast pressure measurements were taken in December 2008 at the blast testing chamber located at the Armament Research, Development and Engineering Center (ARDEC) at Picatinny Arsenal. Piezoelectric pressure gages were mounted in the chamber's instrumentation ports; 1 lb (0.45 kg) spheres of Composition 4 (C-4) plastic explosive (figure 5.9) were then suspended at set standoffs from the ports, from 2 ft to 8 ft in 1 ft increments (figure 5.10), and detonated. The peak pressure and time of arrival could then be read directly from the time history recording from the piezoelectric pressure gages.

The results of the three runs are summarized in tables 5.4 and 5.5. While the times of arrival computed from the run 3 time histories correspond well with the values calculated by CONWEP, the measured peak pressures are much higher than the predicted theoretical value. Additionally, the measurements for standoffs of 3 ft or less may be unreliable, given the conditions of the testing chamber and the capabilities of the piezoelectric pressure gages. Additional work would be necessary to either confirm or dismiss the differences between the measured and theoretical values, or to determine the sources of the discrepancy.

Figure 5.9 1 lb C-4 spheres.

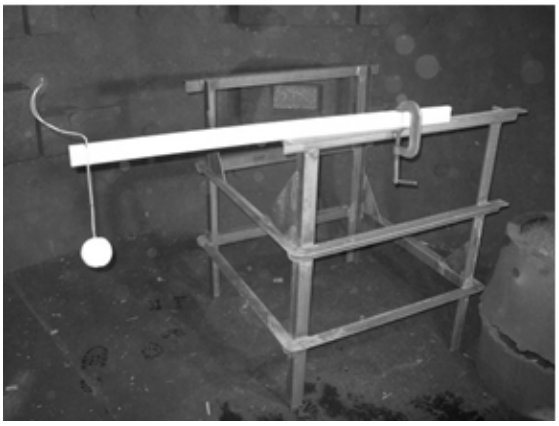

Figure 5.10 Blast test setup for quantitative blast tests; gage ports visible behind frame.

Table 5.4 Measured Peak Pressures of Quantitative Blast Tests

Standoff	Run 1 (psi)	Run 2 (psi)	Run 3 (psi)	CONWEP (psi)
2 ft [a]	3041.4	8744	4915	1736
3 ft [a]	2118.9	2543	[b]	555.6
4 ft	799.5	[c]	628.0	236.1
5 ft	421.6	[c]	358.5	121.8
6 ft	206.9	[c]	209.6	72.16
7 ft	137.34	[c]	139.2	47.27
8 ft	80.93	[c]	91.2	33.37

[a] Sensor readings may not be reliable at this standoff
[b] No clear peak pressure could be determined from the test results
[c] No test performed at this standoff distance for this run

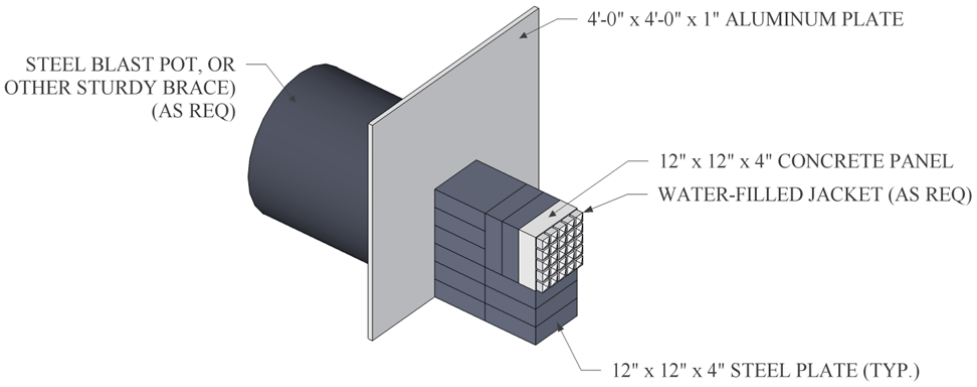

Figure 5.11 Proposed blast testing setup.

5.3.2 Qualitative Protective Capability Blast Tests

To obtain a rough estimate of the protective capability of the prototype jackets (discussed in Section 1.5 on page 5), the ARDEC Picatinny blast chamber was used again in a similar configuration. The proposed test setup (Figure Proposed blast testing setup.), due to material constraints and limitations of the testing chamber, was modified into the deployed setup (Figure Qualitative Protective Capability Blast Tests) where for each test, a 1 lb sphere of C-4 was suspended at a fixed distance above a pair of 12 in × 12 in × 2 in (30.5 cm × 30.5 cm × 5.1 cm) concrete paver blocks, then detonated. One of the two blocks was placed on a steel support so that it would react principally in compression, while the other block spanned between two steel supports with a free span of 10 in (25.4 cm) so as to act principally in flexure.

The pairs of blocks were subjected to blast loads at increasing standoff distances until the damage sustained by the blocks was judged to be just at the point of rupture, then water-filled prototype jackets would be fixed mechanically to a new pair of blocks and subjected to a detonation at the same standoff, to observe whether the shell prevented the block from surpassing its rupture strength. The piezoelectric pressure sensors were not installed for these tests; the chamber operator did not want to subject the sensors to flying debris from the paver blocks or to excess water released by the rupture of the jackets.

The results of the tests are depicted in Figure 5.12. An unprotected block (block #8,

Table 5.5 Leading Wave Time of Arrival of Quantitative Blast Test, Run 3

Standoff	Run 3 (ms)	CONWEP (ms)
2 ft	0.234 95	0.2492
3 ft	[a]	0.526
4 ft	0.852 22	0.905
5 ft	1.370 58	1.373
6 ft	1.899 95	1.916
7 ft	2.572 27	2.523
8 ft	3.278 12	3.182

[a] No clear time of arrival could be determined from the test results

(a) Unprotected blocks 8 and 9, before

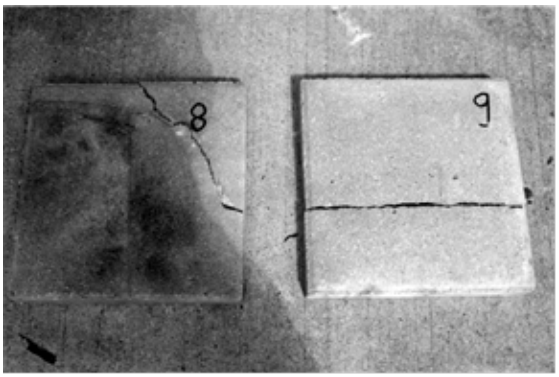

(b) Blocks 8 and 9, after

(c) Protected blocks 10 and 11, before

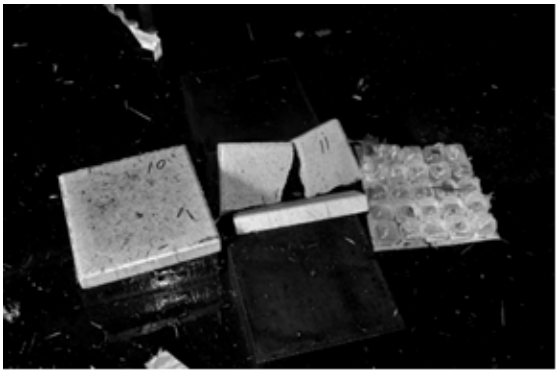

(d) Blocks 10 and 11, after

Figure 5.12 Qualitative protective capacity blast test setup and results.

Figure 5.12a) reacting in compression was found to just fracture when subjected to a blast at a standoff of 2.5 ft (Figure 5.12b); when covered by a jacket, another block (block #10, Figure 5.12c) successfully survived an equivalent blast without sustaining damage (Figure 5.12d).

However, both the protected (block #9) and unprotected (block #11) cases subjected to flexure sustained similar amounts of damage. This is likely due to the very low flexural strength of the concrete blocks: the pressure required for the block to fail in flexure is 20 psi (138 kPa), while the theoretical incidental and reflected pressures calculated by CONWEP for this blast condition are 165 psi (1.1 MPa) and 941 psi (6.5 MPa), respectively. The pressure required to fracture the brick in this set-up is likely too low to realistically expect the jacket to provide the required level of reduction.

CHAPTER 6

INITIAL FINITE ELEMENT SIMULATIONS

As an extension of the laboratory tests, simulations of the various cases from the above set of tests were performed. A nonlinear explicit finite-element model of the laboratory simulation was implemented and refined using ANSYS Workbench to build and mesh the model and ANSYS AUTODYN to perform the simulation. The explicit finite element method implemented in AUTODYN has been shown to lend itself well to realistic modeling the results of blast and impact loads (Chapman 1995, Malvar and Tancreto 1998), in particular in evaluating the total blast impulse energy inflicted upon a structure and producing results near to those predicted by the CONWEP blast effects calculator (Schwer et al. 2008).

6.1 Preliminary Simulation of Impact Tests

The first formulation of an AUTODYN model (Figure 6.1) reproduces the laboratory setup from Section 5.1 as closely as possible, though unlike the laboratory test, the water layer is unconstrained by a flexible container, because of the difficulty of successfully modeling the interaction of the thin shell elements with the hammer, water and beam elements. It is assumed that since the container is intended to be sacrificial, fails almost immediately upon the hammer's impact, and would contribute additional energy dissipation through heat absorption and melting, the effect of omitting it on the total energy absorption should be slightly conservative. The far edges of the lower flanges are constrained by a boundary condition that only permits movement parallel to the span, which creates a roller-roller end condition that is similar but not identical to the experimental setup's pinned-roller condition.

Three simulations were created: the control test, without a water layer, and two experimental tests, with water layer volumes previously tested in the laboratory experiments of 400 mL and 800 mL. A gauge point at the quarter-point of the beam, 2.25 ft (68.9 cm) from the support, records the vertical deflection of the beam over the duration of the simu-

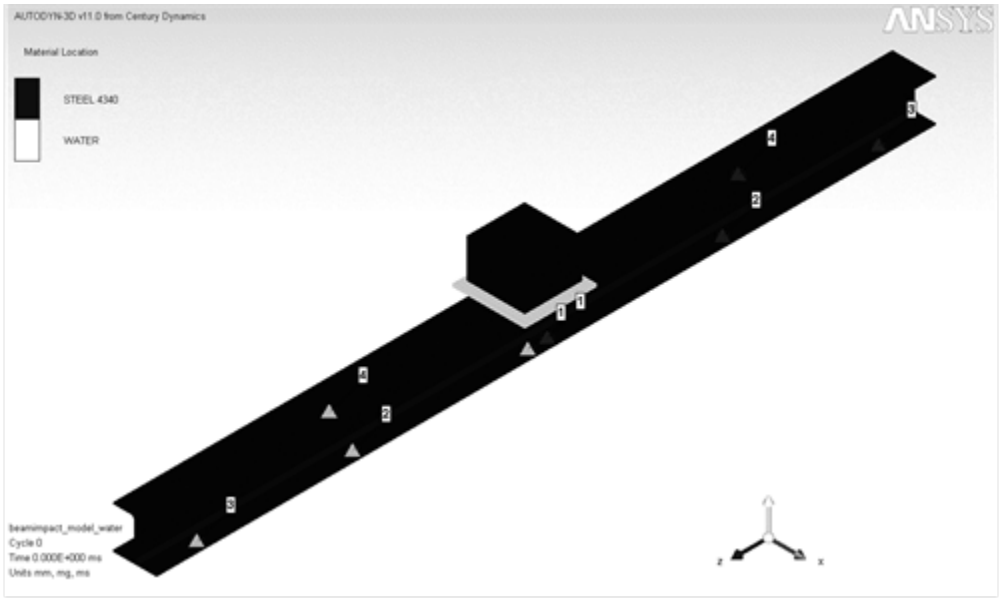

Figure 6.1 Preliminary ANSYS AUTODYN model of the impact testing equipment.

lations, similar to the role of the LVDT in the laboratory experiment. Deflection histories for each of the three simulations are shown in Figure 6.2.

The 400 mL jacket reduces the simulated deflection from 9.43 mm to 8.34 mm; an additional 400 mL of water reduces it further to 7.19 mm. The absolute deflections in the simulation are much greater than the recorded experimental deflections. This is likely due to a pair of reasons: first, the simulation assumes no damping and a frictionless, perfectly rigid roller condition at the ends, both of which will increase the deflection response of the beam; second, the water is less well represented by a Lagrange mesh than by other possible methods, and the water layer in the simulation exhibits some artificial stiffness, such that it does not disperse and travel as dramatically as in the laboratory experiments, demonstrating a lower transfer of kinetic energy from the hammer to the jacket. However, the relative reduction between the control test and the beam protected with 400 mL of water is similar, as shown in Table 6.1.

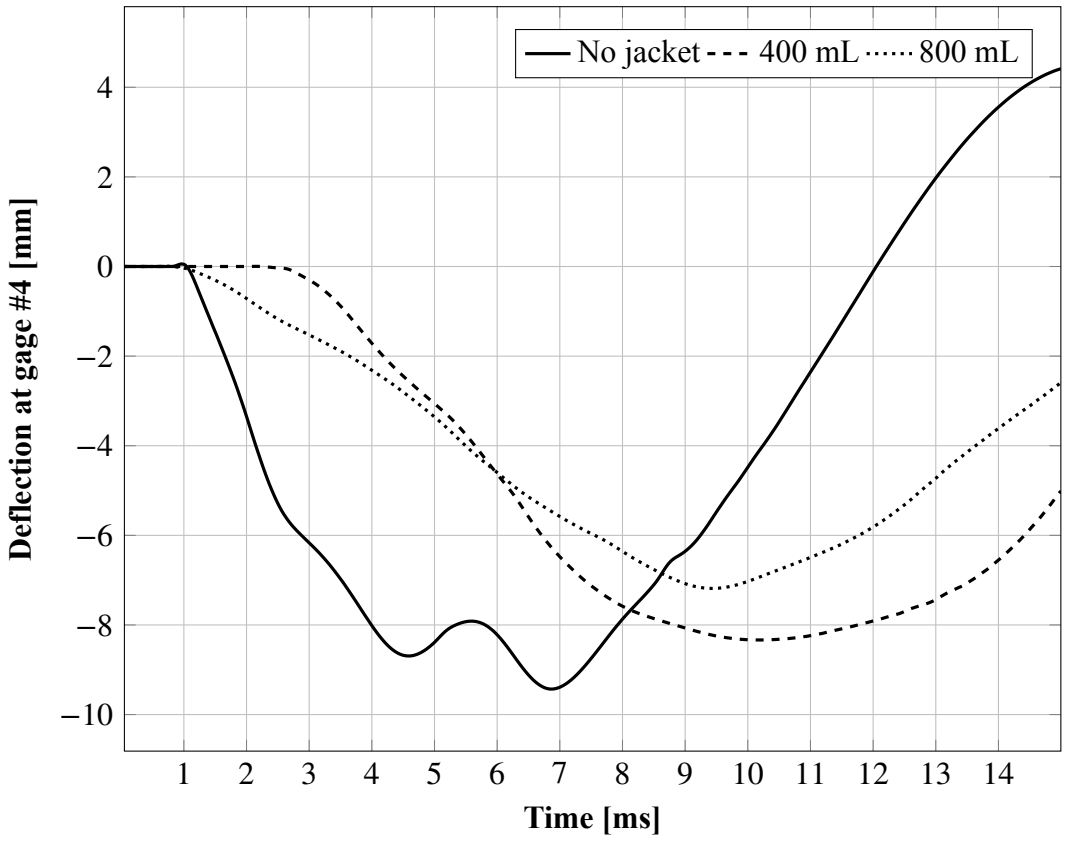

Figure 6.2 Comparison of measured deflection for unprotected and protected cases.

Table 6.1 Comparison of Absolute and Relative Deflection Reduction for Second Impact Tests and Finite Element Simulations

Volume	Experimental $\Delta_{LVDT \cdot max}$ [mm]	% reduction	Simulation $\Delta_{gage4 \cdot max}$ [mm]	% reduction
No jacket	5.50	—	9.43	—
400 mL	4.25	22.7%	8.43	18.2%
800 mL	3.81	30.7%	7.19	40.7%

6.2 Meshless Simulation of Water

The formulation of the finite element model was modified to better reflect the real behavior of water – the steel beam and hammer are still modeled using swept hex Lagrangian elements and the shock equation of state, but now the water is modeled using a smoothed-particle hydrodynamics (SPH) meshless Lagrangian method; SPH models, which simulate the behavior of fluids by dividing them into discrete, unconnected particles, do not suffer from "mesh tangling" caused by excessive displacement like traditional meshed Lagrange models, which makes them suitable for modeling the complex, free-surface behavior and large deformation expected of the water jacket (Carlson and Saadeghvaziri 2010a). The revised models are shown in Figure 6.3.

The simulations predict an energy absorption by the jacket of about 12% solely due to the kinetic dissipation mode. Assuming that the beam behaves elastically as a 1-DOF dynamic system, the energy absorbed by the jacket is directly proportional to the square of the reduction in deflection, corresponding to an approximately 35% reduction in beam deflection, a closer fit to the experimental data than the original Lagrange mesh jacket. Repeating this simulation with a wider range of jacket thicknesses and hammer velocities on a structural member less subject to local deformation is the objective of Chapter 7.

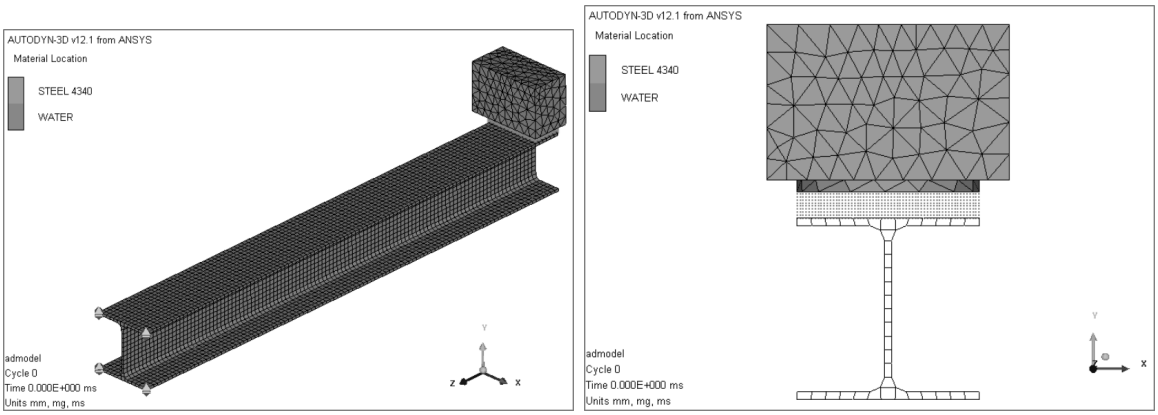

(a) Isometric view. **(b)** Section at midspan.

Figure 6.3 Second ANSYS AUTODYN model of the impact test equipment; the SPH model of water is visible in 6.3b.

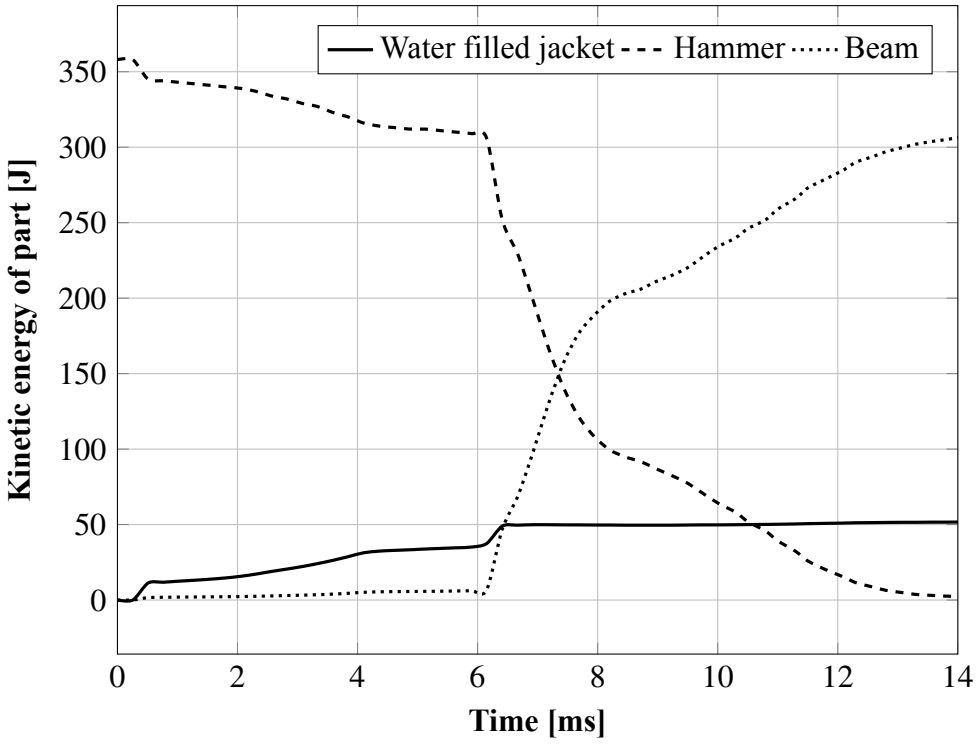

Figure 6.4 Simulation results, showing predicted energy absorption of 800 mL jacket.

6.3 Finite Element Simulation of Blast Tests: General Blast Modeling

To complement the live explosives testing discussed in Section 5.3, a finite element model analysis of blast events was performed with the software packages LS-DYNA and ANSYS AUTODYN and compared to the theoretical values calculated by CONWEP.

The models simulate the effects of a free-air blast of a known amount of an unshaped explosive device occurring in an infinite volume of ideal gas, and record the transient pressures at various standoffs from the blast center. These simulation results were then compared with the calculated CONWEP values for maximum blast pressure, time of arrival and impulse (the time integral of incident pressure) for the same initial conditions. The results from LS-DYNA corresponded poorly with the CONWEP values, while the AUTODYN results matched well in terms of time of arrival and maximum incident pressure, but not total impulse.

The relationship between pressure and time from a typical AUTODYN simulation,

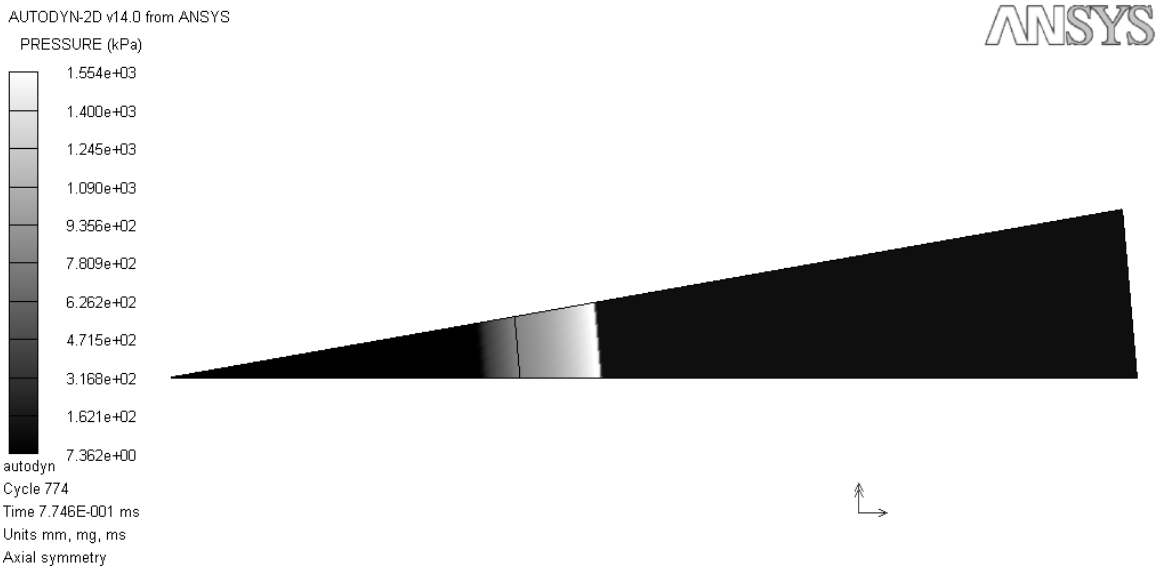

Figure 6.5 Example ANSYS AUTODYN model of a one-dimensional "wedge" of a free-air blast in progress.

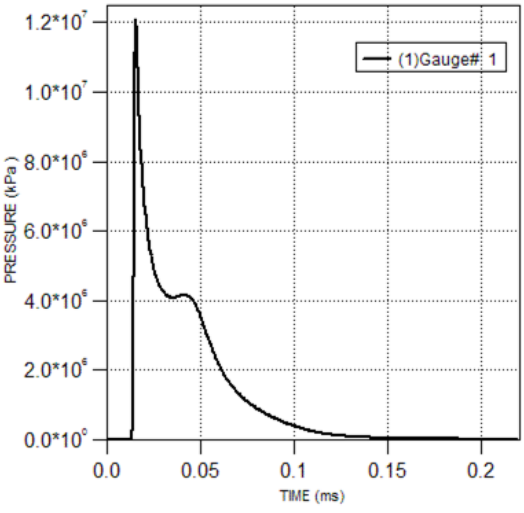

Figure 6.6 Example graph of pressure vs. time for an AUTODYN blast simulation.

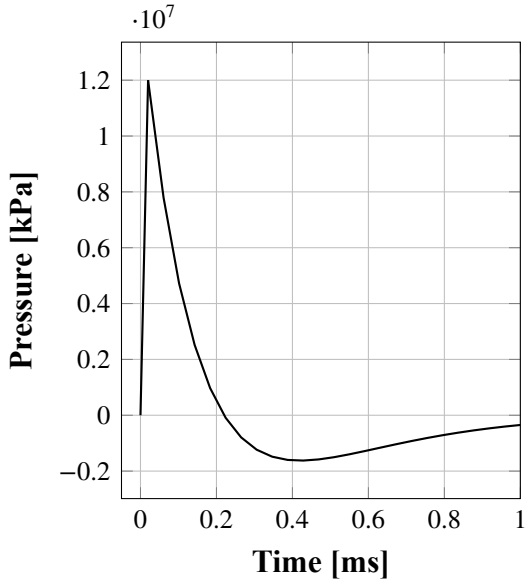

Figure 6.7 Example graph of pressure vs. time generated by an empirical CONWEP analysis of a blast.

such as the one-dimensional simulation in Figure Example ANSYS AUTODYN model of 1D "wedge" of a free-air blast, is shown in Figure 6.6; CONWEP's basic theoretical blast pressure curve shown in Figure 6.7, the Friedlander equation, is a simple exponential curve of the form (Chun 2004)

$$p(t) = p_s^+ \left(1 - \frac{t - t_a}{t_0}\right) e^{\left(-\alpha \frac{t-t_a)}{t_0}\right)} \tag{6.1}$$

p_s^+	peak overpressure
t_a	time of arrival of blast wave
t_0	duration of overpressure phase
α	decay coefficient

The small "bump" in the AUTODYN pressure graph near 0.05 ms may be occurring for one of two reasons:

1. The modeled interface between the explosion product material and the ideal gas material acts as a barrier off of which the pressure waves behind the blast front reflect; the pressure wave then reflects again from the starting point of the blast, creating a lagging secondary peak, or

2. The simulation takes into account that the pressure differential between the leading edge of the blast and the evacuated area inside the blast front is so high, that there is a transient motion of the explosion product back towards the center of the blast to bring the local pressure behind the leading edge towards equilibrium.

While this difference in the simulation does not affect the time of arrival or the maximum pressure, it does cause a difference in total impulse between the AUTODYN simulation and the CONWEP calculated value.

CHAPTER 7

FINITE ELEMENT ANALYSIS OF IMPACT LOADING

In this chapter, the performance of the protective layer against impact loads is studied numerically using finite element analysis. When used to mitigate the impact of a steel hammer on a concrete slab, the jacket significantly reduces the damage and stress in the protected structural elements. The total kinetic energy in each part—the impact hammer, the structural member and the water layer—is also measured and plotted, demonstrating the effective transfer of energy from the hammer to the layer.

7.1 Two-dimensional Analysis of Impact on a Concrete Slab

To make an initial estimate of the kinetic energy dissipation capacity of the water layer, a set of two-dimensional, axially symmetric finite element simulations of blunt hammers of varying speeds impacting a concrete slab was developed for analysis with the AUTODYN explicit finite element solver. While not a common building material, unreinforced bulk concrete was chosen as the target material because of its relative brittleness and susceptability to shock loading, and thus its suitability as a material which would benefit from an ablative protection mechanism, and the ready availability of sophisticated material models for brittle materials, such as the Riedel-Hiermaier-Thoma (RHT) constitutive model and Johnson-Holmquist (JH) damage model (described in Appendix 4.3.1).

The initial configuration and conditions of the protected slab are shown in Figure 7.1, depicting the moment just before the hammer, at its slowest speed traveling at 10 m/s and thus having a kinetic energy of $\frac{1}{2}mv^2 = 4.37$ kJ, impacts the protective layer (if present) and the slab underneath it. Assuming that the damage to the slab will be local compared to the size of the slab and radially distributed through the slab about the perpendicular axis passing through the impact point, the components have been modeled in a finite element analysis package as a two-dimensional axisymmetric mesh.

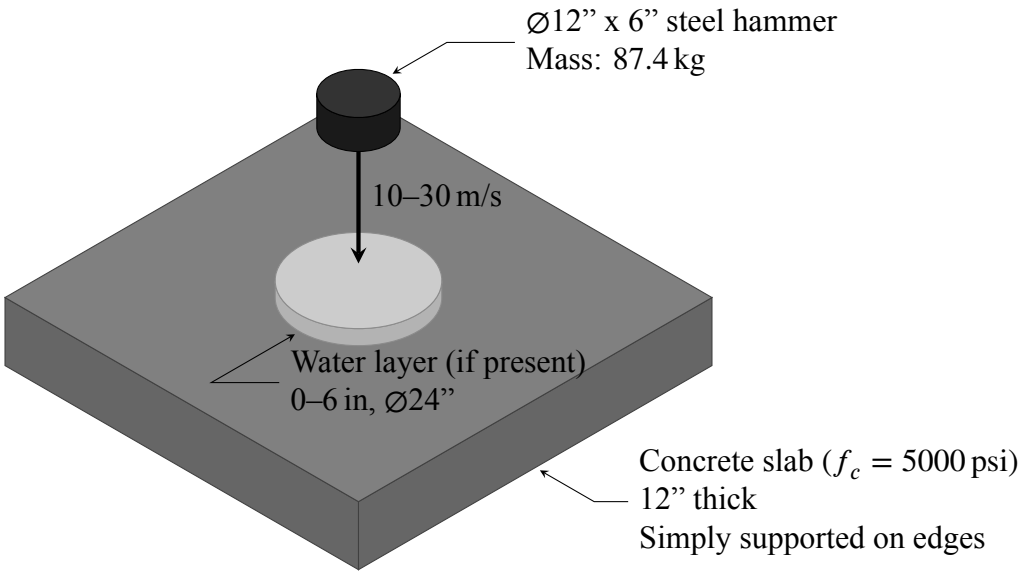

Figure 7.1 General model of impact on concrete slab.

Using ANSYS Workbench to manage the interconnections between components, the solid components were sketched in ANSYS DesignModeler, then imported into ANSYS Explicit Dynamics to generate a suitable tetragonal mesh and establish the boundary conditions to ensure axisymmetry and the initial velocity condition of the hammer. The meshed model was replicated once for each different jacket thickness to be analyzed, and each duplicate was sent to ANSYS AUTODYN for analysis, where the material models were applied. For the control simulation of the unprotected slab, the solid components were simulated as-is, while for the test simulations where the jacket is present, an Euler multi-material mesh was added between the hammer and slab and filled with water to the desired thickness in the region where the jacket is initially present. For each hammer velocity from 10 m/s to 30 m/s in increments of 5 m/s, five simulations were created from the Explicit Dynamics geometry and meshes—one control case with an unprotected slab, then four slabs protected by water jackets up to 6 in (152.4 mm) thick, in increments of 1.5 in (38.1 mm). The maximum speed of 30 m/s was chosen because at this velocity, the slab damage is so severe that the tributary area below the impact surface is knocked free from the rest of the slab.

The aforementioned RHT material model and JH damage model were used to model the behavior of the concrete slab; to model the behavior of water, the Rankine-Hugoniot shock equation of state and the hydrodynamic P_{min} tensile failure model were employed. Since the hammer is only important in that it is used to deliver a shock to the concrete slab, making the detailed internal behavior of the hammer during the impact event relatively unimportant, its material behavior is represented with a simple linear elastic equation of state to simplify calculations. For all materials, the material coefficients and parameters provided by the AUTODYN material library were used, as per the recommendations from Birnbaum et al. (1998), Cheng et al. (2005), Hayhurst et al. (1996)

While the simulation of the impact on the unprotected slab is a straightforward case of solid element interactions, the addition of the water layer complicates the components' interactions. Since the solid elements are best represented as a material-centered Lagrangian mesh and the fluid is more suited to an spatial Eulerian representation, the interaction between the three components is handled by Euler-Lagrange coupling, where the overlap of the Lagrange element and the Euler reference mesh create a dynamic boundary that modifies the volumes of the Euler cells on the interaction boundary, which causes a stress field on the Euler cells and traction forces on the exterior of the Lagrange mesh. Since Lagrange elements often require a smaller time step to accurately model than Euler parts due to the inverse relationship between sound speed and maximum timestep, AUTODYN automatically couples the two reference frames' timesteps, allowing the Lagrange parts to take multiple time steps concurrent with a single Euler time step, then exchanging coupling information at the end of the Euler time step.

For this simulation, an Euler multi-material mesh large enough for the water layer's expected large deformation is placed overlapping the Lagrange elements representing the hammer and slab. The initial configuration of the three elements' meshes are shown in Figure 7.2. Figure 7.3 depicts the partial three-dimensional representation of the initial conditions, produced by revolving the mesh 90° about the axis of symmetry.

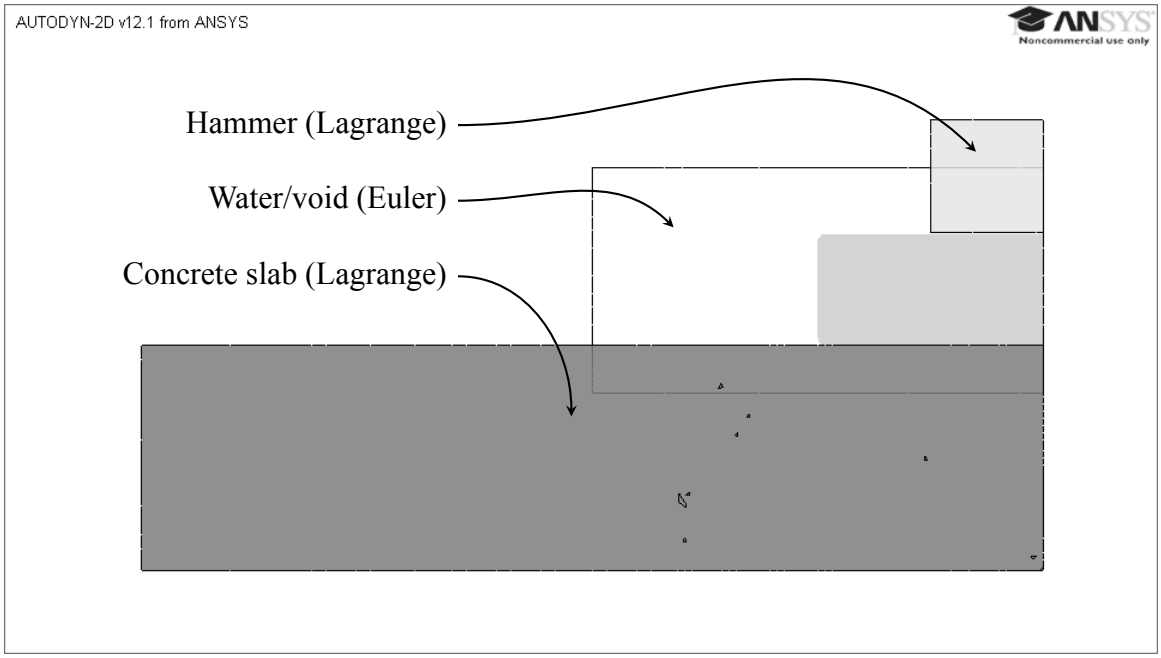

Figure 7.2 Euler-Lagrange mesh coupling in overlapping elements' meshes.

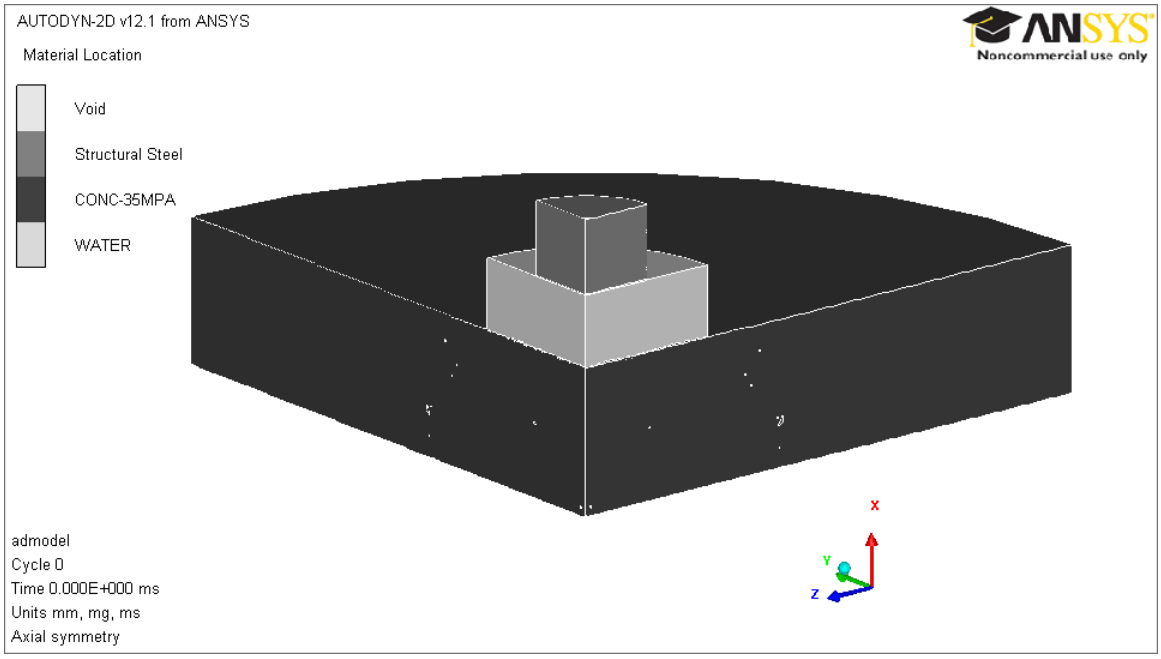

Figure 7.3 Initial conditions of simulation of impact on concrete slab. Two-dimensional mesh is rotated 90˚ about the axisymmetric axis for clarity.

7.2 Qualitative Analysis: Bulk Damage

AUTODYN uses the Johnson-Holmquist to model the reduction in material strength of brittle materials weakened by plastic deformation. The strength and material strain depend dynamically on the Johnson-Holmquist damage parameter D, the normalized ratio of current plastic strain to the pressure-dependent fracture strain, such that $D = 0$ for intact concrete within the elastic limit; $D = 1$ at fractures within the slab, and $0 < D < 1$ for varying states of strain-induced brittle weakening in between. Using the AUTODYN visualization tools, a contour plot of D over the cross-section of the slab provides a straightforward depiction of the location and extent of cracks within the slab at any time in the impact simulation.

The simulations of the 10 m/s hammer impacting the unprotected slab and the slab protected by the 6 in jackets were chosen first for an initial qualitative comparison. The unprotected slab (Figure 7.4) exhibits the typical damage expected in a sudden impulse event: a large volume of crushing failure directly below the impact site, diagonal shear cracking along the boundaries of the stress discontinunity propagating through the slab, and spalling at the base of the slab due to the tensile stresses caused by the reflection of the stress wave at the material boundary. The damage to the slab around the impact area is critical, significantly reducing its effective strength.

The slab protected by the 6 in jacket (Figure 7.5), in comparison, suffers much less damage. Only a very small superficial area near the center of the impact area is damaged completely, with some small regions of mild plastic strain induced weakening underneath the impact area; none of the shear cracks or spalling inflicted on the unprotected slab are present in the protected slab. The post-event strength of the protected slab is, by visual inspection of the damage patterns, much closer to its original strength than that of the unprotected slab.

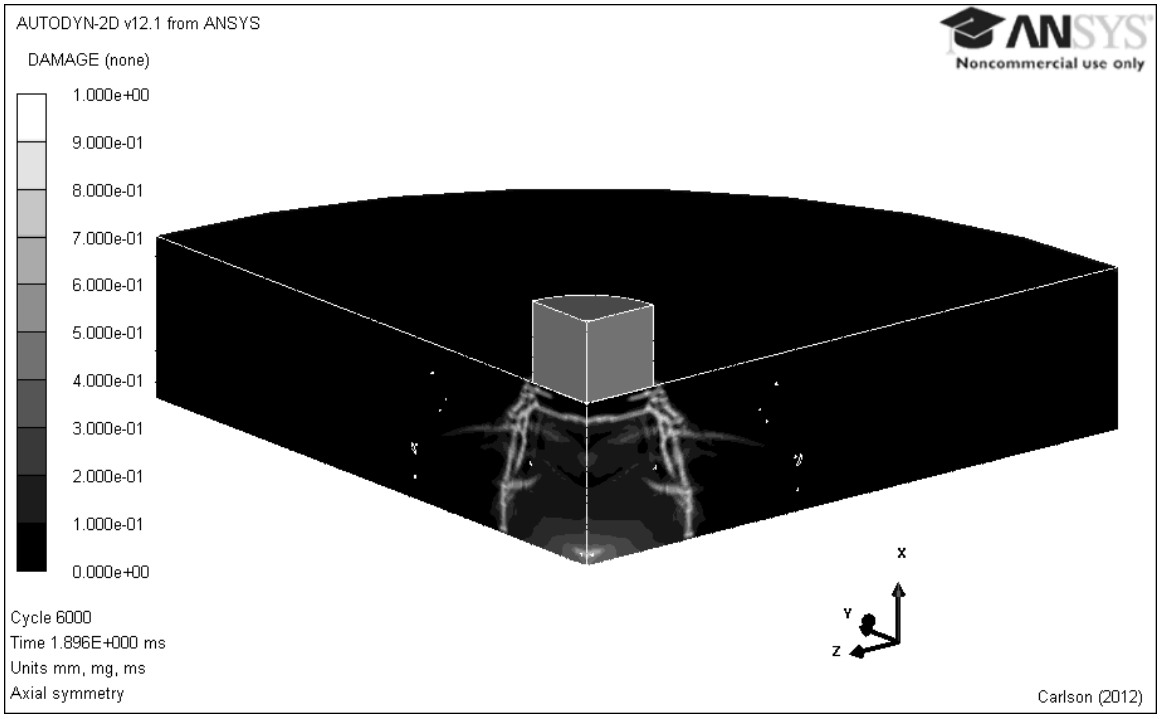

Figure 7.4 Three-dimensional representation of damage in slab caused by 10 m/s hammer impact without water layer present. Lighter-colored regions sustained more damage than darker-colored regions.

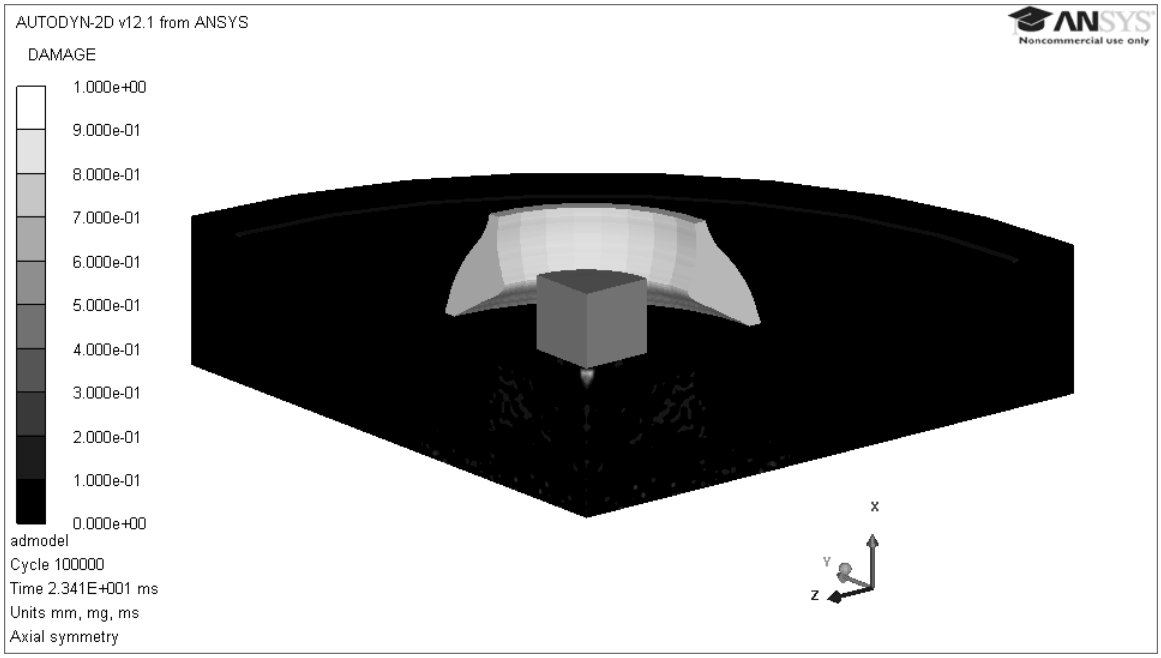

Figure 7.5 Three-dimensional representation of damage in slab caused by 10 m/s hammer impact with 6 in thick water layer present.

After the comparison of the first pair of simulations, the qualitative analysis was extended to hammer speeds from 10 m/s to 30 m/s and jacket thicknesses from 1.5 in to 6 in, with 25 simulations performed in all. The cross-sections through the slab at the moment the hammer is either arrested or rebounding, showing a contour plot of relative Johnson-Holmquist damage, are shown side-by-side in Figures 7.6 to 7.10. For example, the comparisons of damage in the slabs struck by the 30 m/s hammer in Figure 7.10 show how the jackets effectively reduce the catastrophic punching shear and large deflections suffered by the unprotected slab to milder shear cracking which does not penetrate the slab and could temporarily hold its shape and transfer loads across it long enough to satisfy the life-safety evacuation requirements of a building's performance criteria.

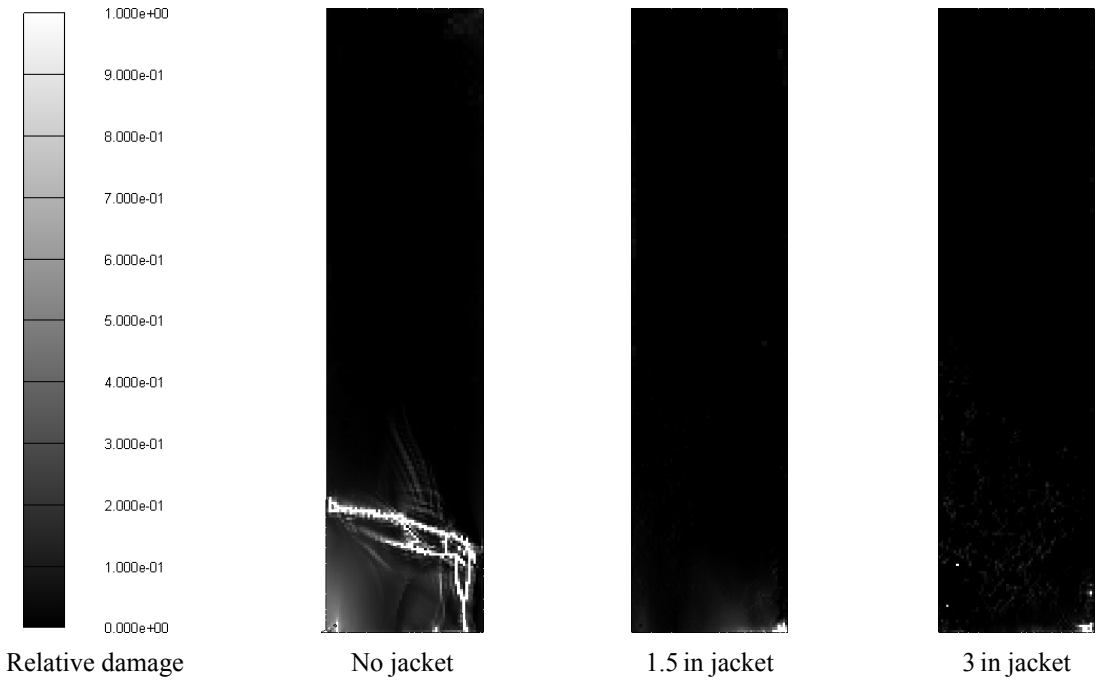

Figure 7.6 Comparison of damage in slab caused by 10 m/s hammer to unprotected and protected concrete slabs. The hammer impact point is at the bottom right corner of the cross-section.

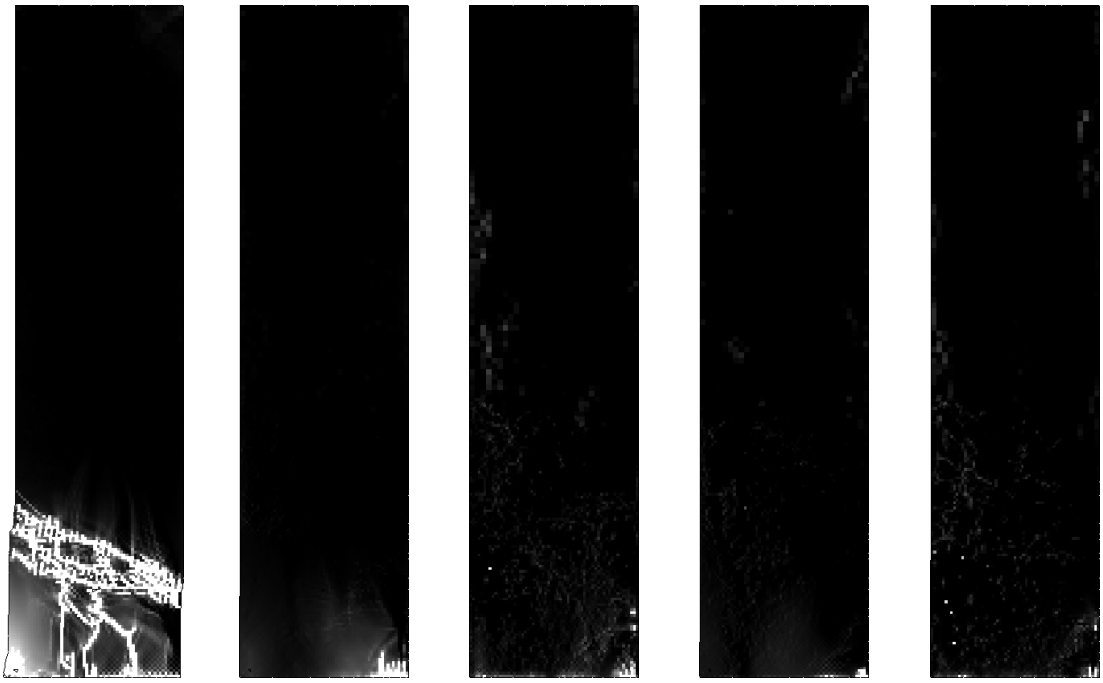

Figure 7.7 Comparison of damage in slab caused by 15 m/s hammer to unprotected and protected concrete slabs.

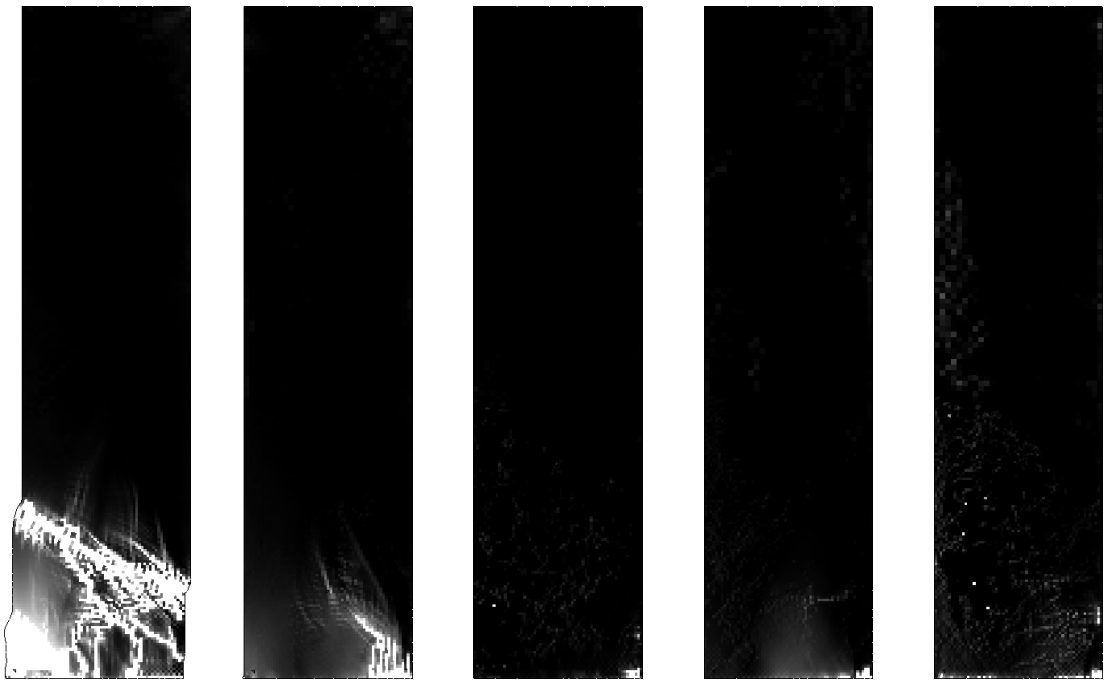

Figure 7.8 Comparison of damage in slab caused by 20 m/s hammer to unprotected and protected concrete slabs.

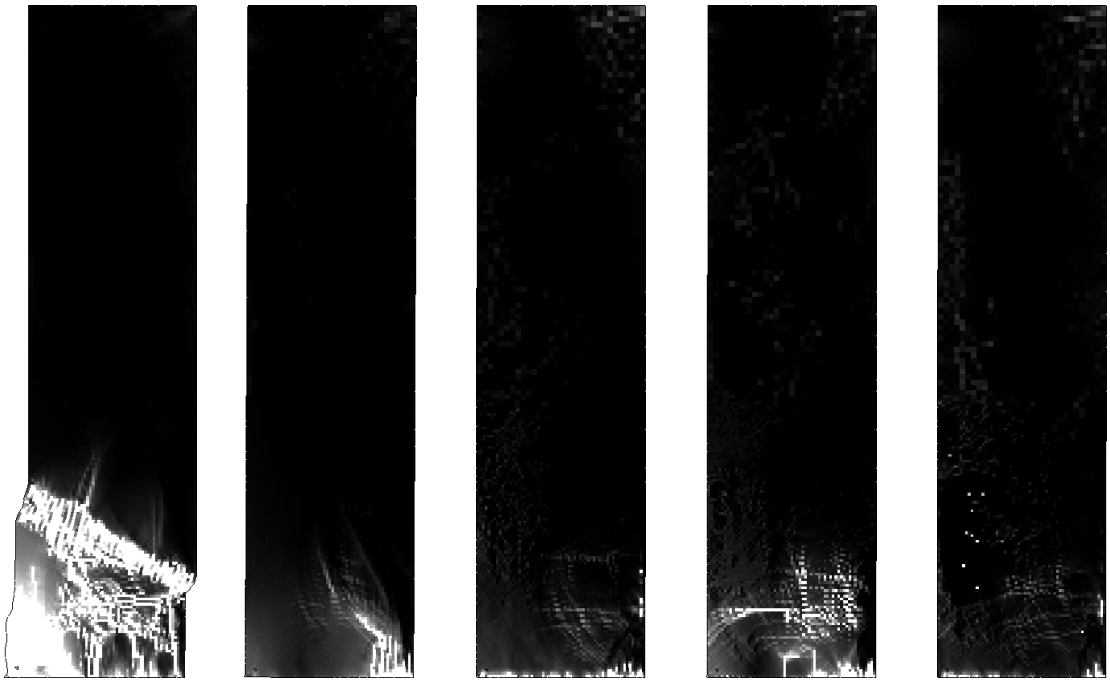

Figure 7.9 Comparison of damage in slab caused by 25 m/s hammer to unprotected and protected concrete slabs.

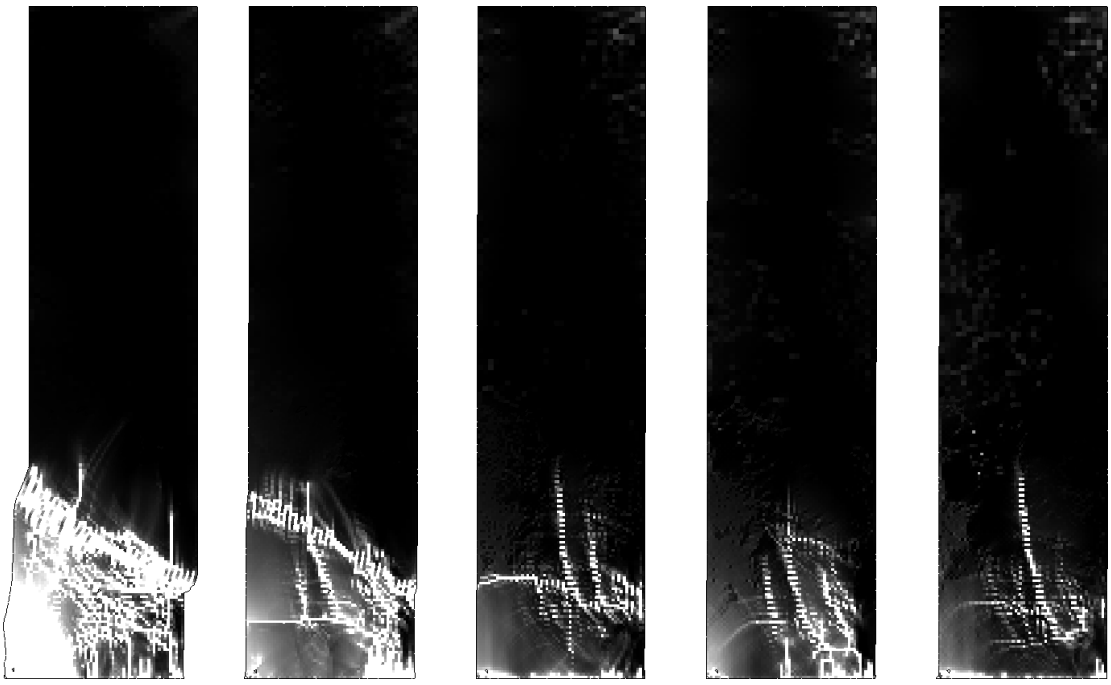

Figure 7.10 Comparison of damage in slab caused by 30 m/s hammer to unprotected and protected concrete slabs.

7.3 Quantitative Analysis: Energy Transmitted to Slab

While the visual inspection of the damage patterns in the slabs are a valuable qualitative measurement of the protective capacity of the jackets in the kinetic dissipation mode, it is necessary to analyze the quantitative material properties of the slab to calculate the amount of energy dissipated by the jacket and the commensurate reduction in the structural response of the slab. The measure chosen to quantify the protective capacity of the water jackets was the amount of total energy (both kinetic and strain) present in the slab after the hammer had either rebounded from or come to rest on the slab's surface.

The total kinetic and internal energy in each part in the prior impact simulations were tracked over time; additional simulations with a jacket thickness of 0.75 in was added for each hammer velocity to investigate the energy transmission of very thin jackets. Figures 7.11 through 7.15 show the significant effect of the kinetic dissipation mode of the water jacket for impact; for every combination of jacket thickness and hammer velocity, the water dissipates at least 65% of the energy—and in many cases, nearly all of the energy—of the hammer by transforming it to kinetic energy. For each hammer velocity, the energy dissipation peaks at a jacket thickness of approximately 3 in with rapidly diminishing returns for larger amounts of water.

Because of the excellent performance of the protective jacket under an impact load, the simulations were modified and updated to simulate the capacity of the jackets under blast loading conditions and measure the underlying structural members' response; these simulations and their results are presented in the following chapter.

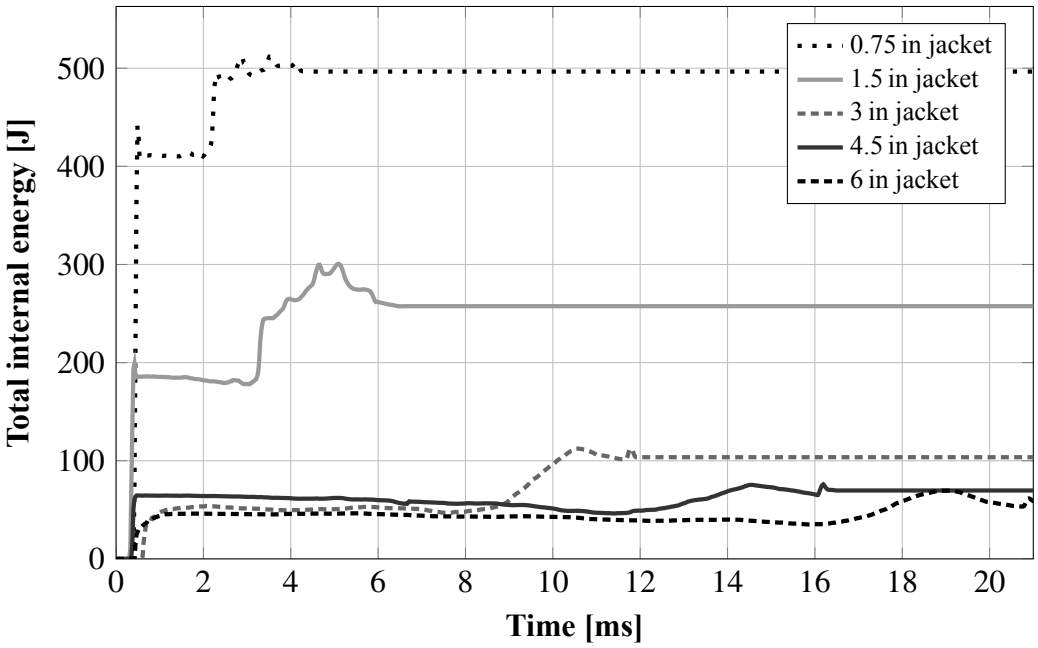

Figure 7.11 Energy transmitted to slab during impact event, 10 m/s hammer with 4.37 kJ kinetic energy.

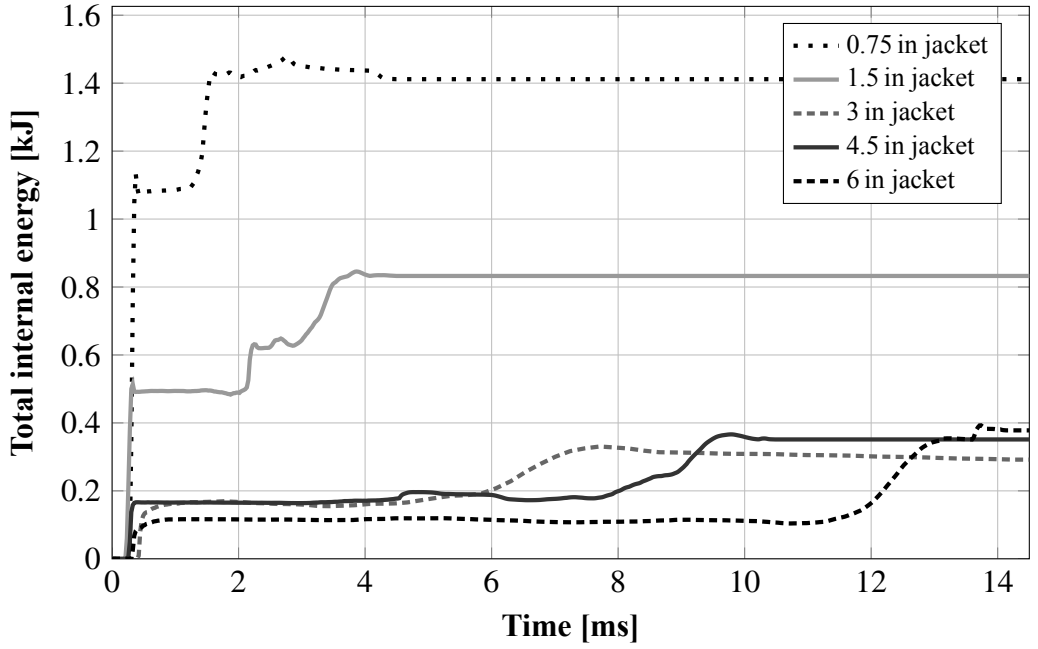

Figure 7.12 Energy transmitted to slab during impact event, 15 m/s hammer with 9.83 kJ kinetic energy.

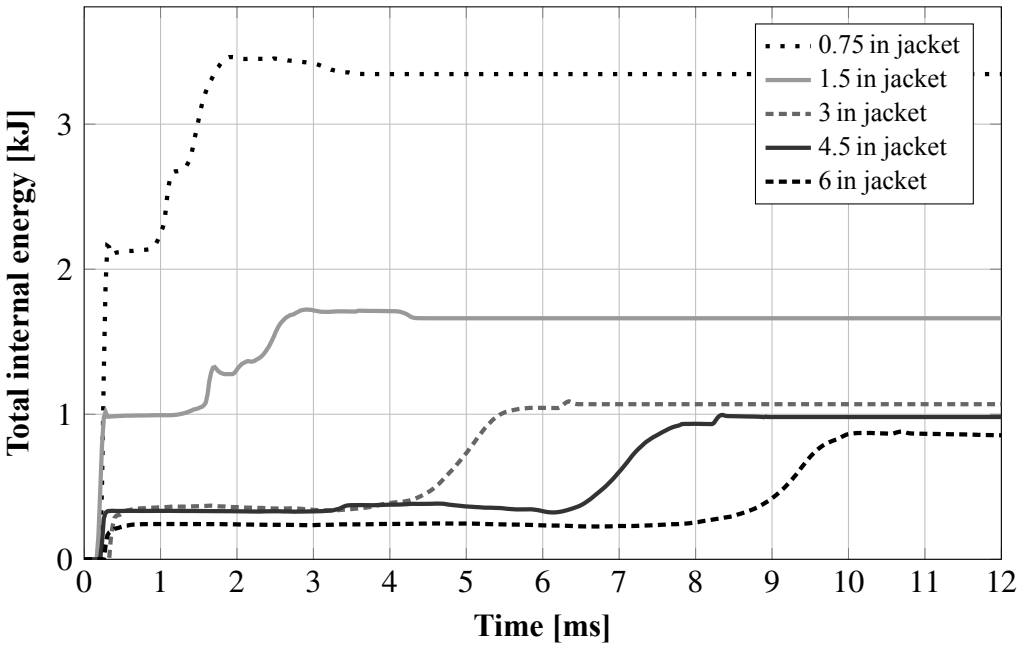

Figure 7.13 Energy transmitted to slab during impact event, 20 m/s hammer with 17.48 kJ kinetic energy.

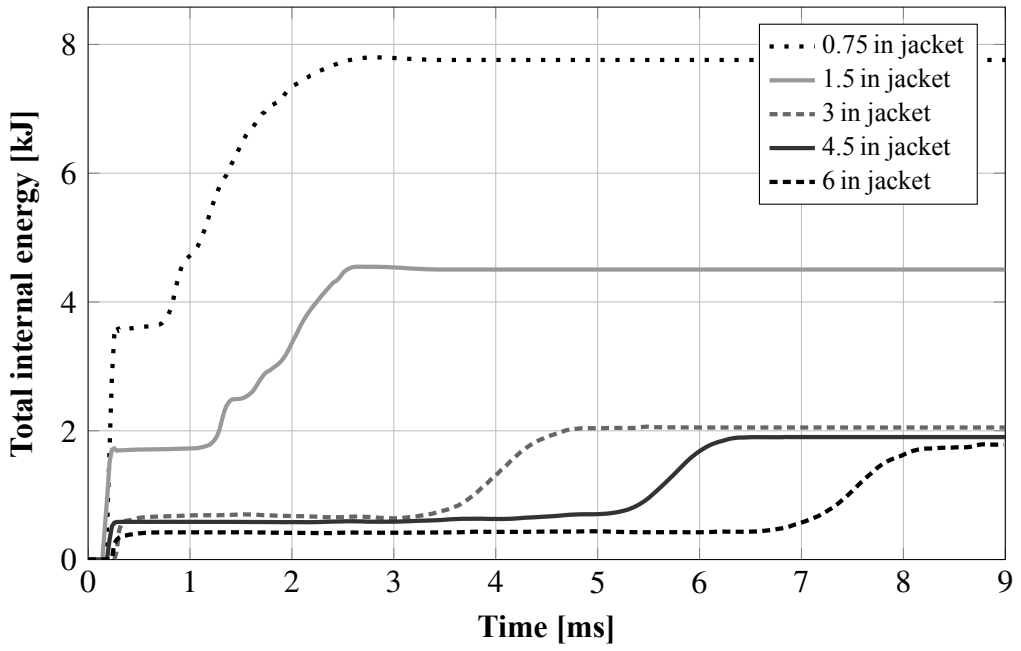

Figure 7.14 Energy transmitted to slab during impact event, 25 m/s hammer with 27.31 kJ kinetic energy.

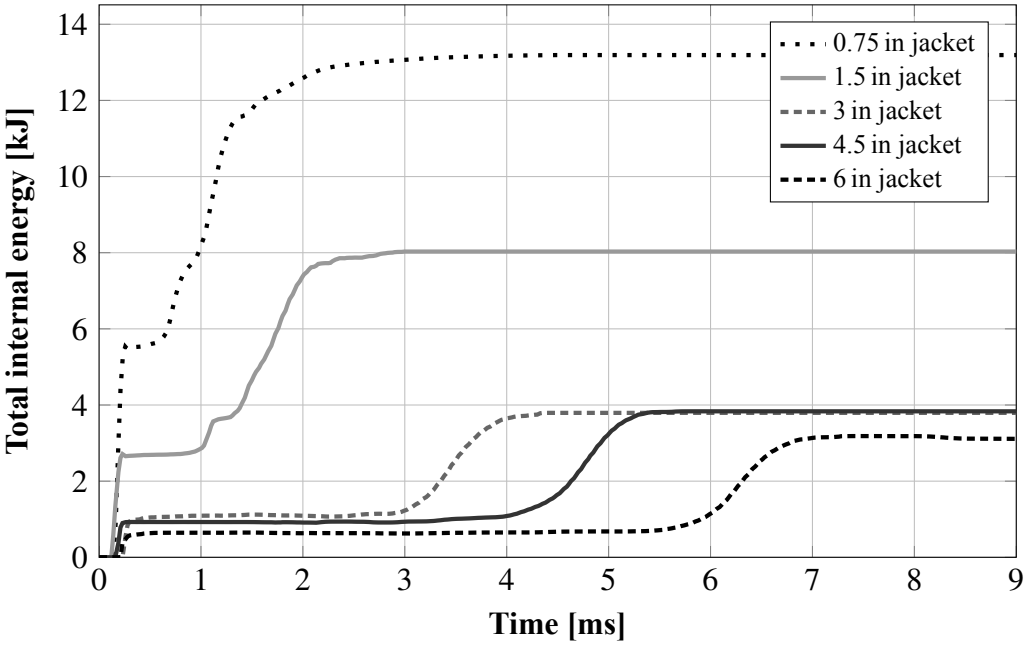

Figure 7.15 Energy transmitted to slab during impact event, 30 m/s hammer with 39.33 kJ kinetic energy.

Table 7.1 Peak Energy Transmission to Slab During Impact Event

	Transmitted energy through jacket				
Jacket thickness	**10 m/s**	**15 m/s**	**20 m/s**	**25 m/s**	**30 m/s**
No jacket	4.36 kJ	9.81 kJ	17.34 kJ	24.65 kJ	35.26 kJ
0.75 in	0.50 kJ	1.47 kJ	3.46 kJ	7.78 kJ	13.19 kJ
1.5 in	0.30 kJ	0.85 kJ	1.72 kJ	4.55 kJ	8.03 kJ
3.0 in	0.11 kJ	0.33 kJ	1.09 kJ	2.06 kJ	3.79 kJ
4.5 in	0.08 kJ	0.37 kJ	1.00 kJ	1.90 kJ	3.83 kJ
6.0 in	0.07 kJ	0.39 kJ	0.88 kJ	1.79 kJ	3.18 kJ

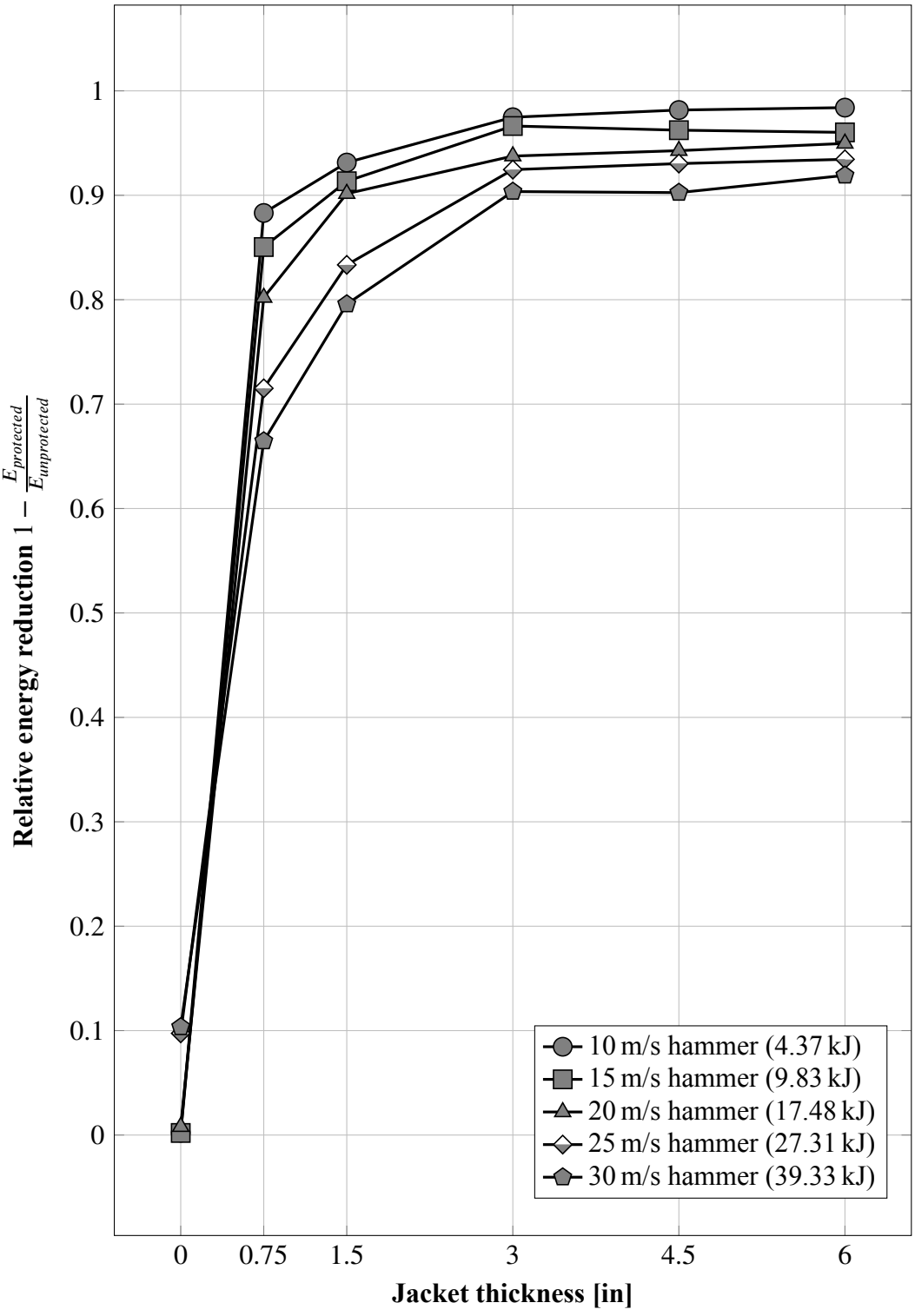

Figure 7.16 Relative peak energy reduction during impact event of protected and unprotected slabs for varying jacket thicknesses.

CHAPTER 8

FINITE ELEMENT ANALYSIS OF BLAST LOADING

In this chapter, the simulations performed in the previous chapter are adapted to predict the structural response to given blast loads and measure the analytical blast damage reduction capacity of the protective layer. The Analytical Blast boundary condition for Lagrange volumes is described and its applied pressure and impulse are found to compare well to those of a traditionally-modeled free air blast in an Euler volume. The Analytical Blast boundary is then used in simulations of blast loading on protected and unprotected structural elements, demonstrating both qualitatively and quantitatively the ablative properties of the protective jacket.

8.1 Comparison of Analytical Blast Boundary to Euler Blast Simulation

Traditionally, to model a blast event, a two-dimensional Euler mesh with a multi-material processor is used to model the volume of a theoretical semi-infinite atmosphere centered on an explosive device at a given setback from a rigid wall; the boundary conditions set the floor and wall of the chamber and the boundary of the rigid wall to be adiabatic and rigid with no outflow, while the other sides allow outflow. A typical configuration of the modeled area is shown in Figure 8.1. Often, to increase the accuracy of the simulation, a high-resolution one-dimensional spherical-symmetric Euler simulation of a blast was formulated and simulated up until the point where the leading edge of the blast wave would reach a reflecting surface, then remapped into a two-dimensional axisymmetric plane or a three-dimensional volume using the finite element software's preprocessing fill remapping functions; one example of this method follows the procedure laid out by Century Dynamics (2006) in their AUTODYN tutorial on two-dimensional blast simulation. This avoids the need to perform complicated preparation like inserting higher-resolution subgrids or repeatedly dezoning the mesh as the blast propagates through the Euler volume.

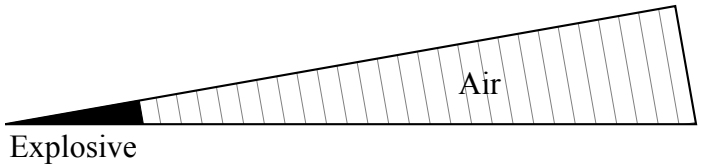

(a) Initial 1D wedge simulation.

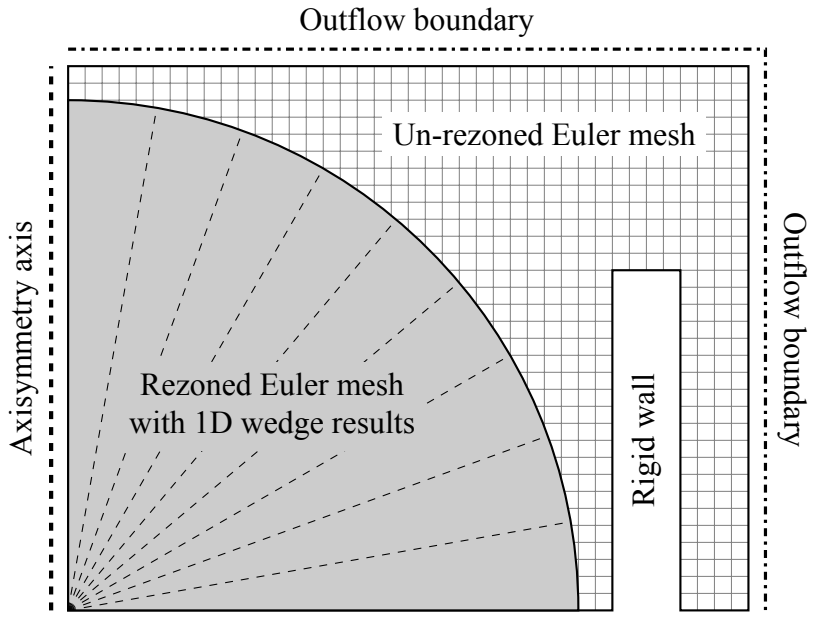

(b) Wedge simulation remapped to 2D axisymmetric plane.

Figure 8.1 Typical configuration of Euler mesh for blast simulation.

However, as described in Chapter 4, the Analytical Blast boundary condition allows for the simulation of blast pressure loads on three-dimensional volume elements caused by high explosive detonations using the numerical methods presented in the U.S. Army Technical Manual *Fundamentals of Protective Design* (Department of the Army 1986), rather than the explicit finite element simulation of an Euler volume. This significantly reduces the amount of numerical computation required to simulate the effects of a structure subject to a blast, since it is no longer necessary to simulate and couple the Euler mesh containing the surrounding atmosphere. The analytically-determined blast pressures and times of arrival, the same as those calculated by the blast analysis software package CONWEP, correspond well to those calculated by explicit finite element methods (Schwer et al. 2008). Additional information about the Analytical Blast boundary can be found in Section 4.4.3.

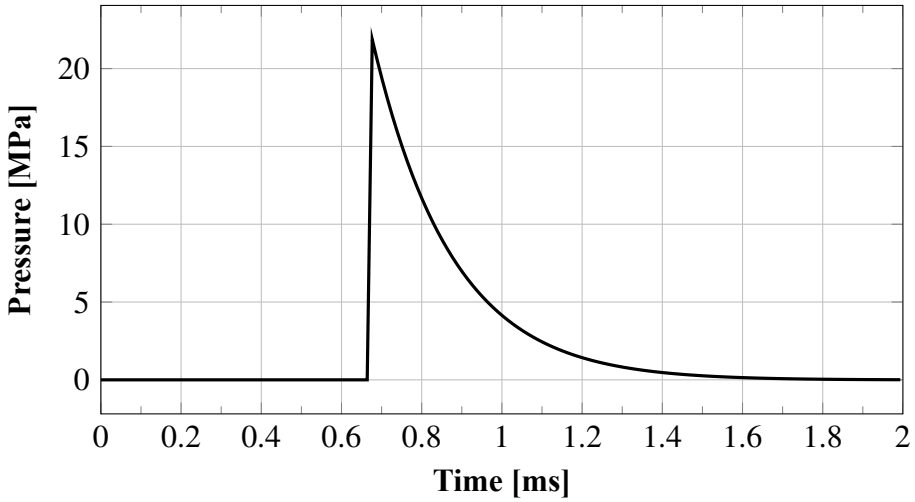

Figure 8.2 Example reflected blast pressure generated by the Analytical Blast boundary condition for a 45 kg TNT bomb at a 2.5 m standoff from a wall perpendicular to the blast wave trajectory.

Using this boundary condition, the surfaces of a structure subject to blast can be "painted" with the Analytical Blast boundary condition and analyzed without needing to separately calculate the atmospheric pressures around the structure or set up a Lagrange-Euler interaction between the solid and the surrounding atmosphere. An example plot of the generated blast pressure applied at the Analytical Blast boundary condition is shown in Figure 8.2; compare to Figures 6.6 and 6.7.

To test the results of the Analytical Blast boundary condition as compared to a traditional remapped Euler blast simulation, a continuation of the work done by Allahverdi (2010) (previously discussed in Section 2.4) on measuring the effect of cross-sectional shape on the peak reflected pressures on the boundaries of columns was performed, using the Analytical Blast boundary condition along the exterior of a Lagrange column rather than the original remapped Euler mesh simulation of an open-air blast.

The column shapes and dimensions and explosive weights and standoffs are the same as those used in the simulations in Allahverdi (2010)—the square columns have a cross-section of 1000 mm × 1000 mm, where the orthogonal square column is oriented with its windward side perpendicular to the blast trajectory and the rotated square column is

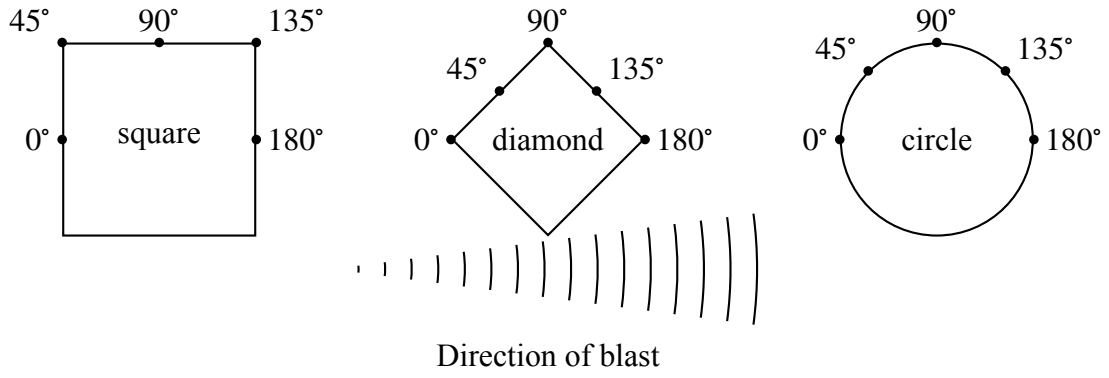

Figure 8.3 Radial locations of gauge points on column cross-sections.

rotated 45° about its center so a corner is at the most windward point, and the circular column has a diameter of 1000 mm. The simulated blast is caused by a detonation of 45.4 kg of TNT equivalent at a standoff of 2500 mm from the centerline of the column, a scaled distance of $Z = 0.56\,\mathrm{m/kg^{1/3}}\ \left(1.41\,\mathrm{lb/ft^{1/3}}\right)$.

A one-element thick slice from the center of the column is modeled, due to the requirement that the Analytical Blast condition be placed on a 3D volume element, rather than the 2D area elements used in the original Euler simulation. Gauges are placed at each element on the exterior of the column and set up to record the blast pressures at each timestep of the simulation. Figure 8.4 shows the variation in reflected pressures along the windward side of the columns' exteriors ; the gauge at 0° is placed at the windward point of the column nearest the blast, receiving the maximum reflected pressure, while the gauge at 90° is placed at the lateral side of the column, where it is only subject to the incident pressure. Figure 8.5 compares the open-air simulation results to the analytical blast approximations for each column configuration. The boundary condition is set to consider the effects of clearing near geometric discontinuities and reduce the peak reflected pressures and impulses accordingly, following the fictitious-pressure method described in Section 4.4.3 of Chapter 4.

According to the simulation using the Analytical Blast boundary, the rotated square column is subjected to a peak pressure of 19.3 MPa at its windward point, a reduction of about 15% compared to the peak pressure of 22.5 MPa in the same location on the orthog-

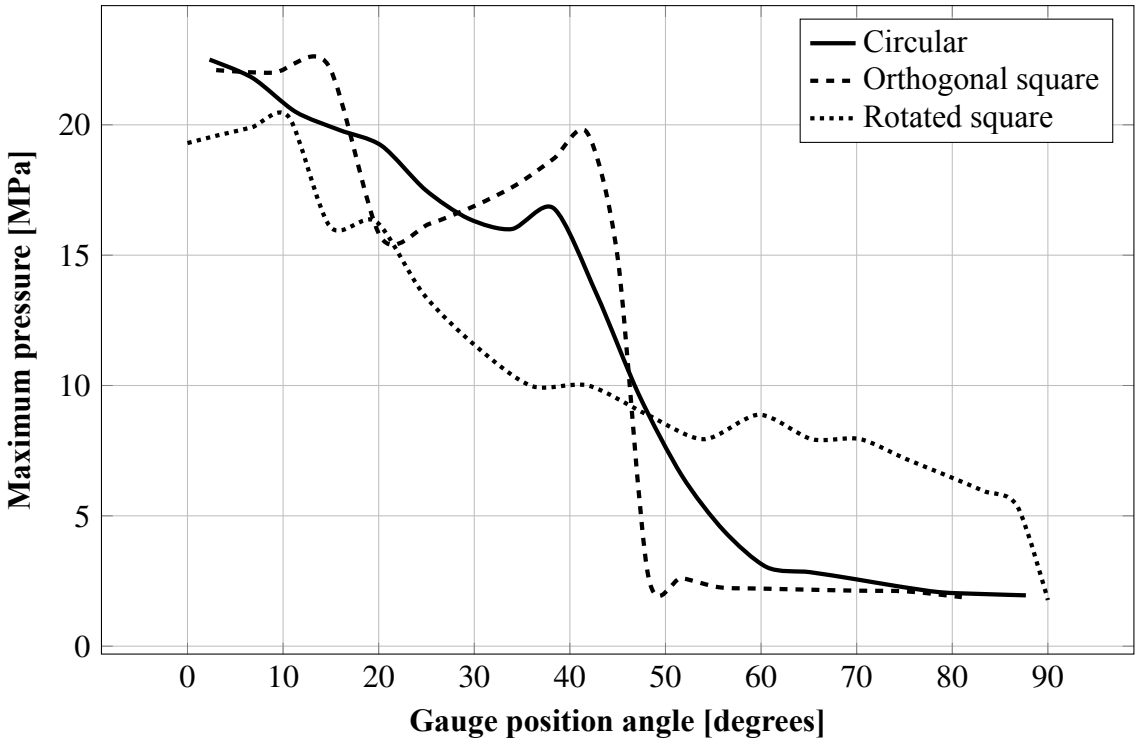

Figure 8.4 Peak reflected pressures at points along the circumferences of various column cross-section shapes subjected to a detonation of 45.4 kg of TNT equivalent at a standoff of 2500 mm (scaled distance $Z = 0.56\,\mathrm{m/kg^{1/3}}$).

onal square column. This is a lesser reduction compared to the open-air simulation, where rotating the column reduces the peak pressure at the windward point of the square column by about 30%. The difference in the measured reflected pressures at the windward point and the smaller effect of column rotation on the maximum pressure are due to the open-air model's ability to directly model the flow-field interactions around the column, including the expansion fans that form at geometric discontinuities which cause commensurate reductions in reflected pressure. The analytical blast model does not take these flow interactions into consideration, causing it to generate a more conservative estimate of the reflected pressures closer to the windward side of the column; however, away from the geometric discontinuity at the windward edge, the effects of the expansion fans is less important, and the two models come into very close agreement.

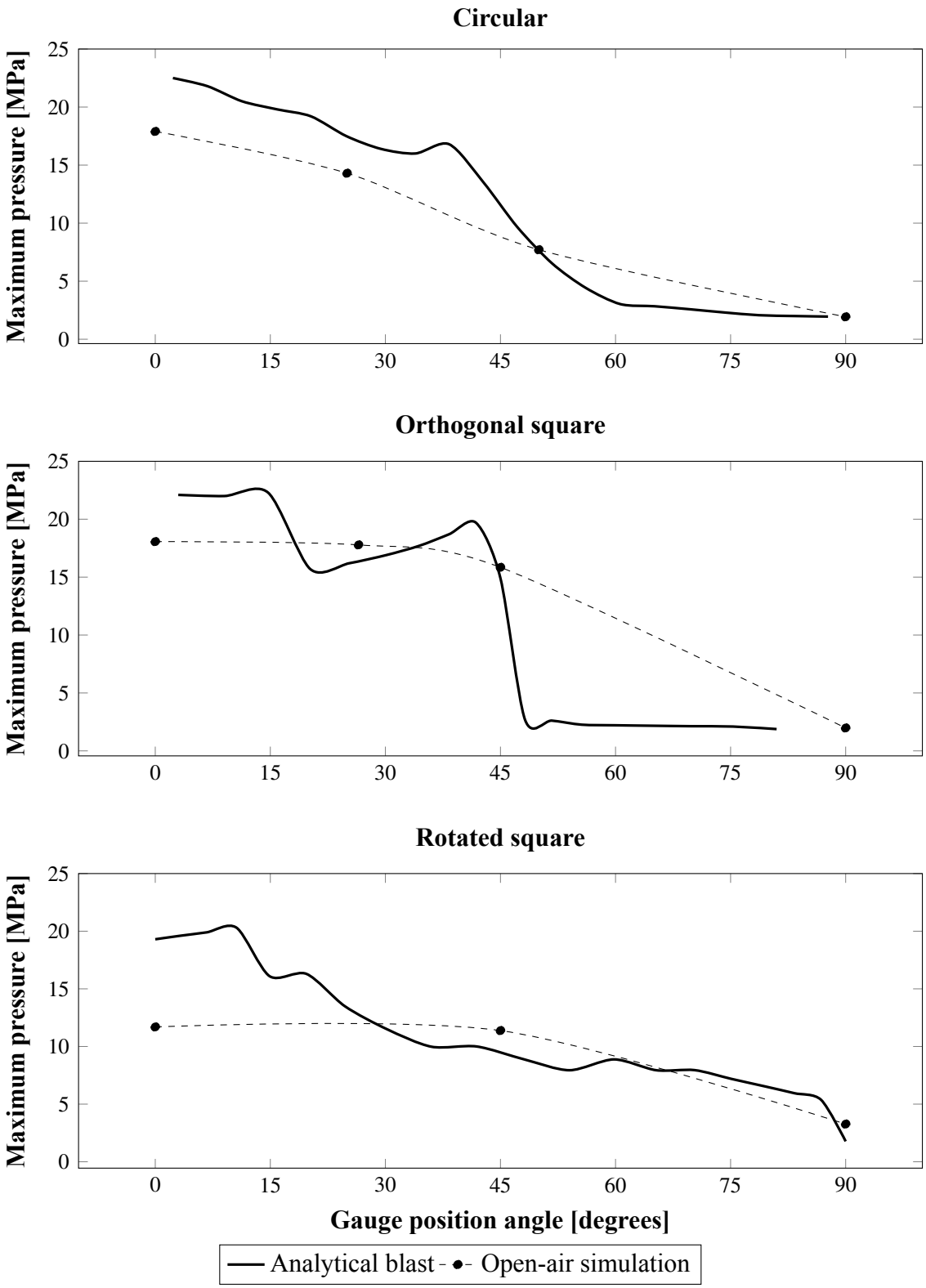

Figure 8.5 Comparison between peak reflected pressures for analytical blast simulation and open-air simulations by Allahverdi (2010).

8.2 Qualitative Analysis of Blast on a Concrete Slab

As a precursor to the quantitative analyses performed in the following section (Section 8.3), a set of qualitative simulations were run to observe the severity and location of damage in a concrete slab, simply supported on its edges and spanning 3 m, subject to a given blast loading. The setup is similar to the bulk damage simulations in Section 7.2, as shown in Figure 8.6; the concrete's failure behavior is simulated with the Johnson-Holmquist accumulated damage model, with the relative damage parameter D used to measure the severity of damage in each element, the water is again modeled with the Rankine-Hugoniot shock equation of state and the hydrodynamic P_{min} tensile failure model, and the Analytical Blast boundary condition is used to apply the blast loads to the slab and jacket.

Cross-sections of each slab approximately 1.3 ms after the blast event showing the accumulated damage in each element are shown in Figure 8.7. The jackets effectively reduce the damage and deflection demand in the slab, preventing the punching failure and reducing the large deformations caused in the unprotected case.

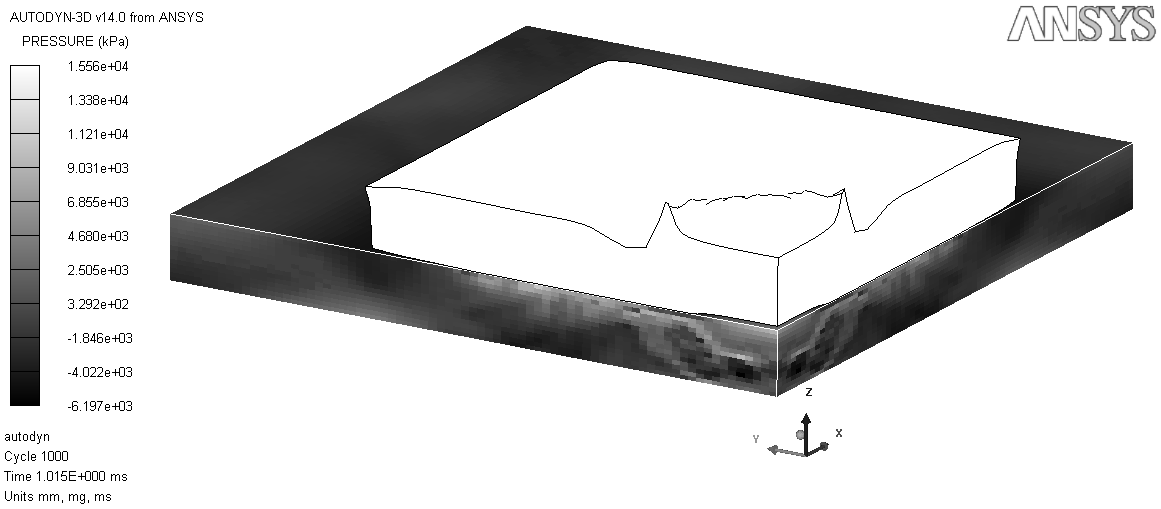

Figure 8.6 Configuration of qualitative analysis simulation.

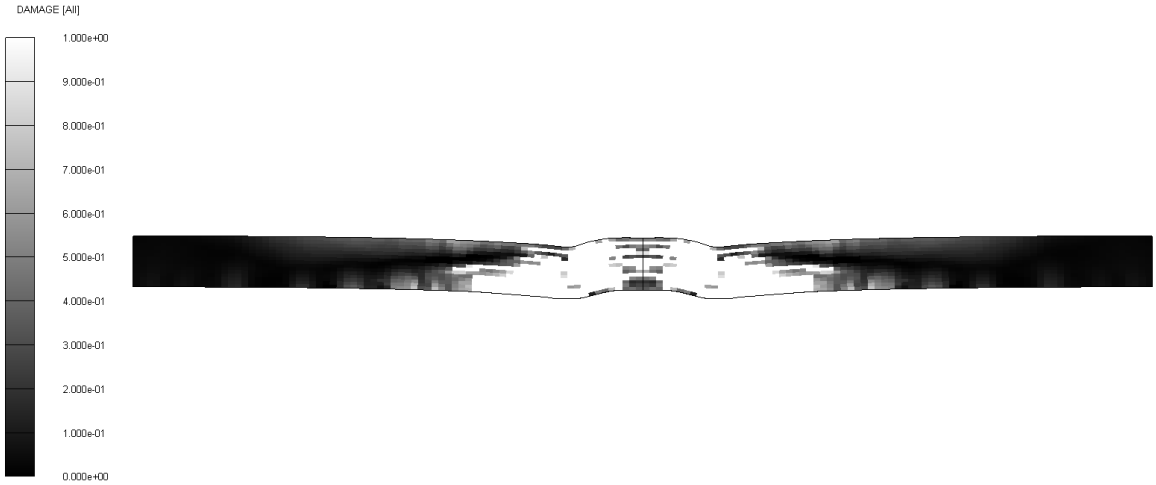

(a) No jacket: major bulk failure and large deflections.

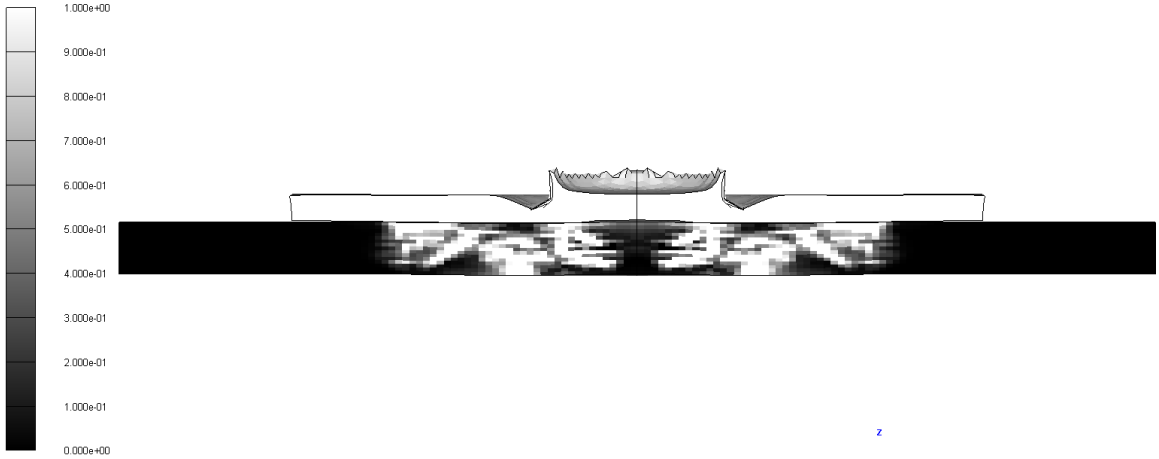

(b) 3 in jacket: major shear failure, but less deflection demand than the unprotected case

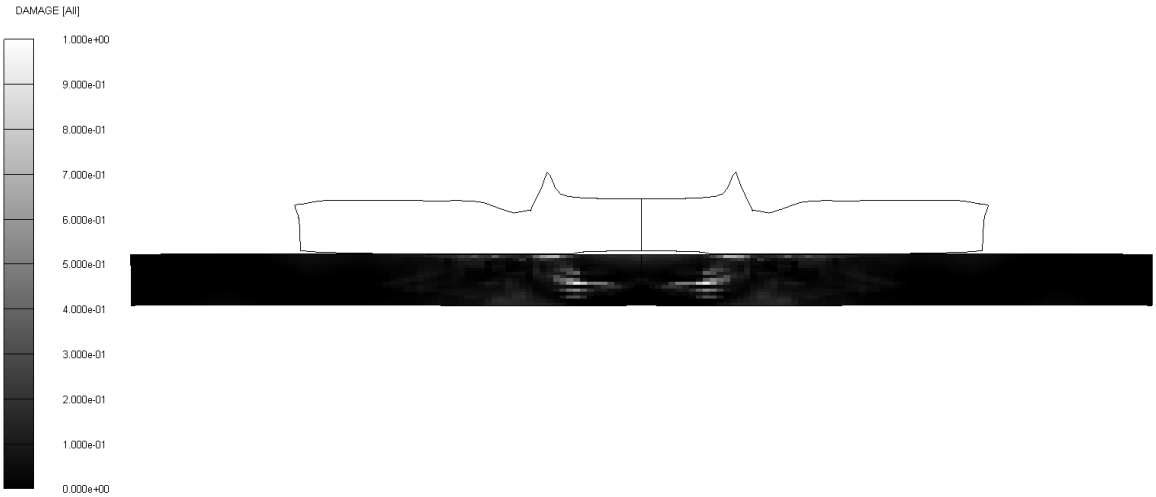

(c) 6 in jacket: minor surface damage and shear failure.

Figure 8.7 Damage and deflection along centerline of slab caused by 20 kg TNT at 1.0 m standoff, equivalent to $Z = 0.37\,\mathrm{m/kg^{1/3}}$ scaled standoff. (Lighter-colored regions sustained more damage than darker-colored regions.)

8.3 Quantitative Analysis of Blast on a Concrete Slab

8.3.1 Implementation and Formulation

A series of models similar to those analyzed in section 7.1, consisting of a three-dimensional bulk concrete slab subject to varying analytically-determined blast pressures on its windward face and completely supported on its leeward face, with blast loading either directly applied to the surface of the concrete or through protective water layers of various thicknesses, were created, meshed and analyzed in ANSYS AUTODYN to measure the pressure and impulse imparted to the top face of the concrete slab.

Because of limitations with how the Analytical Blast boundary condition can be applied, the slab and water layer needed to be modeled as 3D planar Lagrange-formulation planar-symmetric bodies, rather than the interacting 2D axisymmetric Lagrange and Euler meshes used for the impact simulations. The water is modeled with the meshfree Lagrange smooth particle hydrodynamics method previously seen in section 6.2, while the concrete

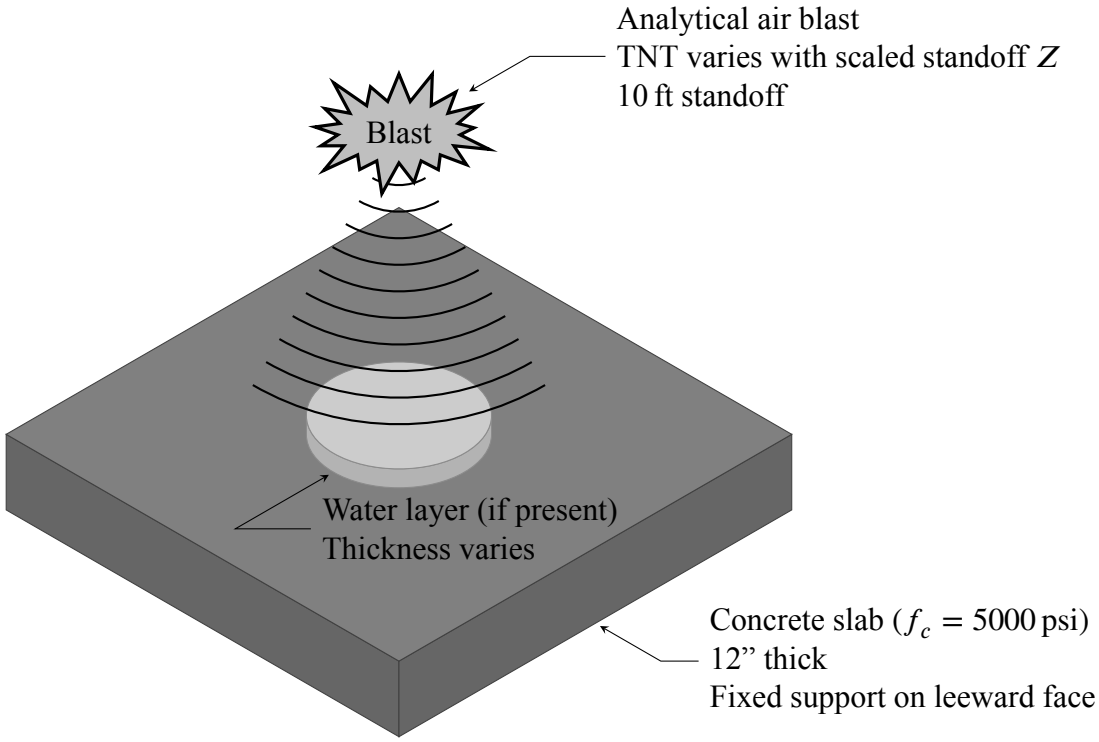

Figure 8.8 General model of analytical blast on concrete slab.

Table 8.1 Explosive Weights and Standoffs Equivalent to Simulated Blast Loadings

Scaled distance $Z = R/W^{1/3}$ $\left[\text{ft/lb}^{1/3}\ \left(\text{m/kg}^{1/3}\right)\right]$	**Equiv. TNT weight @ 5 ft standoff [lb (kg)]**	**Equiv. TNT weight @ 10 ft standoff [lb (kg)]**	**Equiv. TNT weight @ 20 ft standoff [lb (kg)]**
$1.25\,\text{ft/lb}^{1/3}\ \left(0.5\,\text{m/kg}^{1/3}\right)$	64.0 lb (25.4 kg)	512 lb (203 kg)	4100 lb (1625 kg)
$2.5\,\text{ft/lb}^{1/3}\ \left(1\,\text{m/kg}^{1/3}\right)$	8.00 lb (3.63 kg)	64.0 lb (29.0 kg)	512 lb (232 kg)
$5\,\text{ft/lb}^{1/3}\ \left(2\,\text{m/kg}^{1/3}\right)$	2.37 lb (1.08 kg)	8.00 lb (3.63 kg)	64.0 lb (29.0 kg)

slab remains a typical Lagrange mesh.

A new element, a polyurethane sheet modeled using shell elements placed over atop the water, serves the dual roles of more accurately modeling the confinement of the water in a typical deployment of the protective jacket and providing a surface onto which the Analytical Blast condition can be applied, since it cannot be applied directly to the meshfree elements making up the water. When subject to large blast loads, the polyurethane sheet undergoes very large deformations, so to reduce the effects of large mesh deformations and mesh tangling on the model's energy error, AUTODYN is set to erode away (remove from the simulation) those elements which have a geometric strain of 1.5 or more; that is, they have been stretched to 150% their original length in the course of the simulation, under the assumption that they have either torn or melted under the force of the blast. While this is not strictly physically accurate, it is preferable to the errors introduced when Lagrange elements are subject to high shear deformations and the reduction in the maximum timestep that the solver can iterate over..

In these simulations, scaled standoff distances of $Z = 1.25\,\text{ft/lb}^{1/3}$, $2.5\,\text{ft/lb}^{1/3}$ and $5\,\text{ft/lb}^{1/3}$ ($0.5\,\text{m/kg}^{1/3}$, $1\,\text{m/kg}^{1/3}$ and $2\,\text{m/kg}^{1/3}$) have been chosen, representing scaled blast pressures corresponding with varying levels of structural damage to unreinforced buildings (Department of the Navy 1999). Choosing a standoff distance of 10 ft to be used in the simulations, these scaled distances correspond to actual explosive weights of 512 lb, 64.0 lb

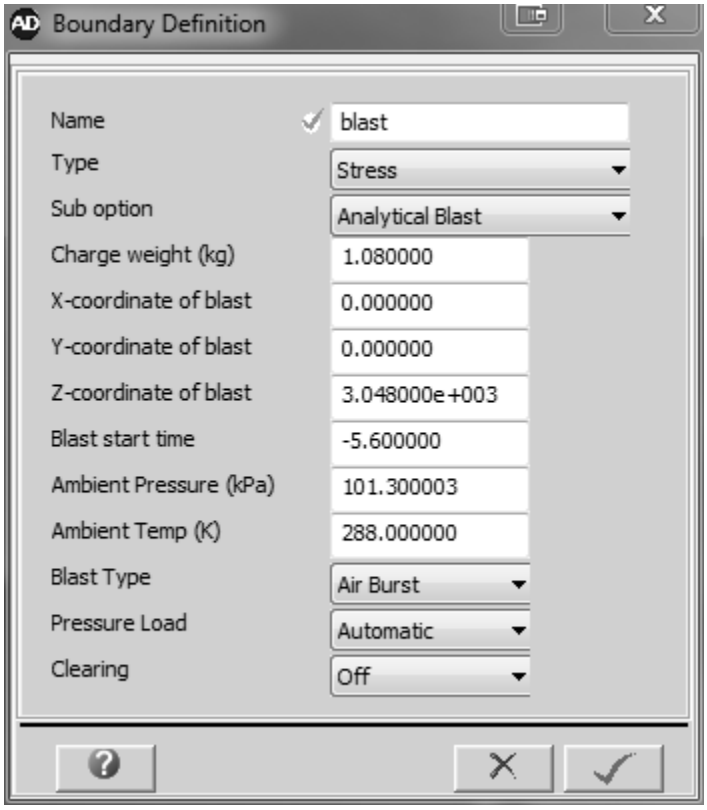

Figure 8.9 Boundary definition settings for the analytical blast condition, representing a blast with a scaled standoff distance of $Z = (3.048\,\text{m})\,(1.08\,\text{kg})^{-1/3} = 3\,\text{m/kg}^{1/3} = 7.5\,\text{ft/lb}^{1/3}$. The *blast start time* is set to -5.6 ms since the time of arrival is approximately 5.7 ms, preventing the unnecessary simulation of the slab's state for the long period before the shock wave's arrival.

and 8.00 lb of TNT (Table 8.1). These chosen scaled distances, while only requiring the simulation of three different blast cases, represent a broad assortment of typical blast events a designer may wish to consider in designing a protective system – from small hand-carried or backpack-sized concealed explosive devices placed near the targeted structure, to larger vehicle-borne ones weighing in the tons parked along a curb or behind security bollards.

8.3.2 Analysis of Results

In total, 15 simulations were performed, covering every combination of jacket thicknesses (0 in, 1.5 in, 3 in, 4.5 in and 6 in) and scaled blast distances (1.25 ft/lb$^{1/3}$, 2.5 ft/lb$^{1/3}$ and 5 ft/lb$^{1/3}$). The range of blast intensities creates a variety of structural responses in the

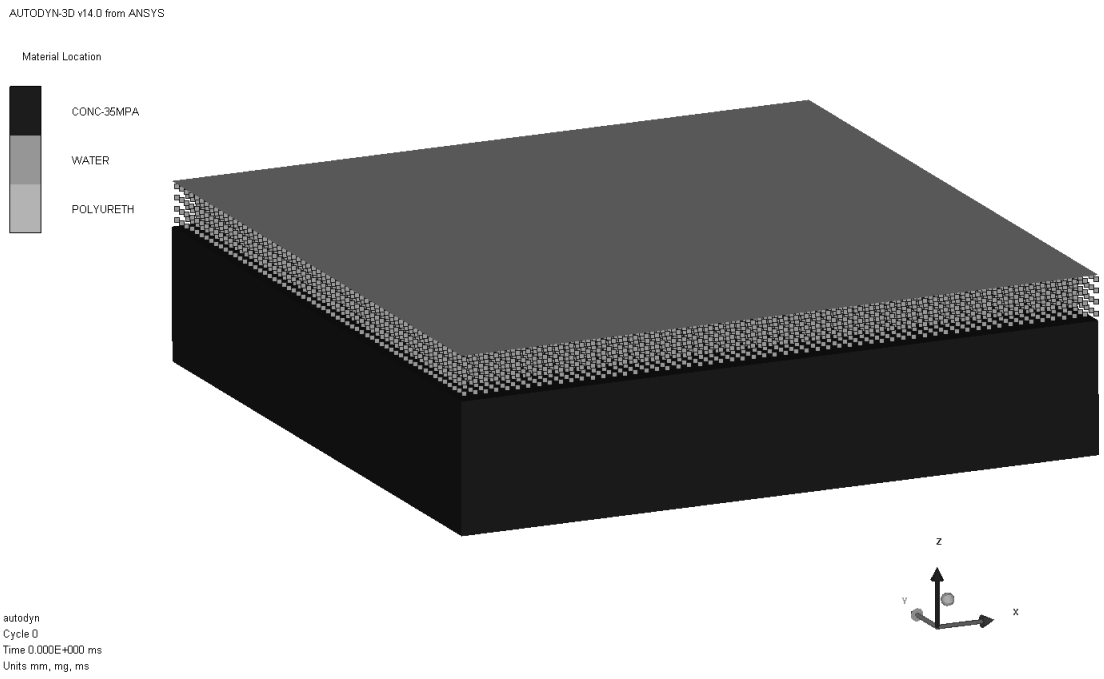

Figure 8.10 ANSYS AUTODYN model of analytical blast on a 12 in thick concrete slab with 3 in protective jacket. Model is symmetric about the XZ and YZ planes. Gauge points are placed on face exposed to blast.

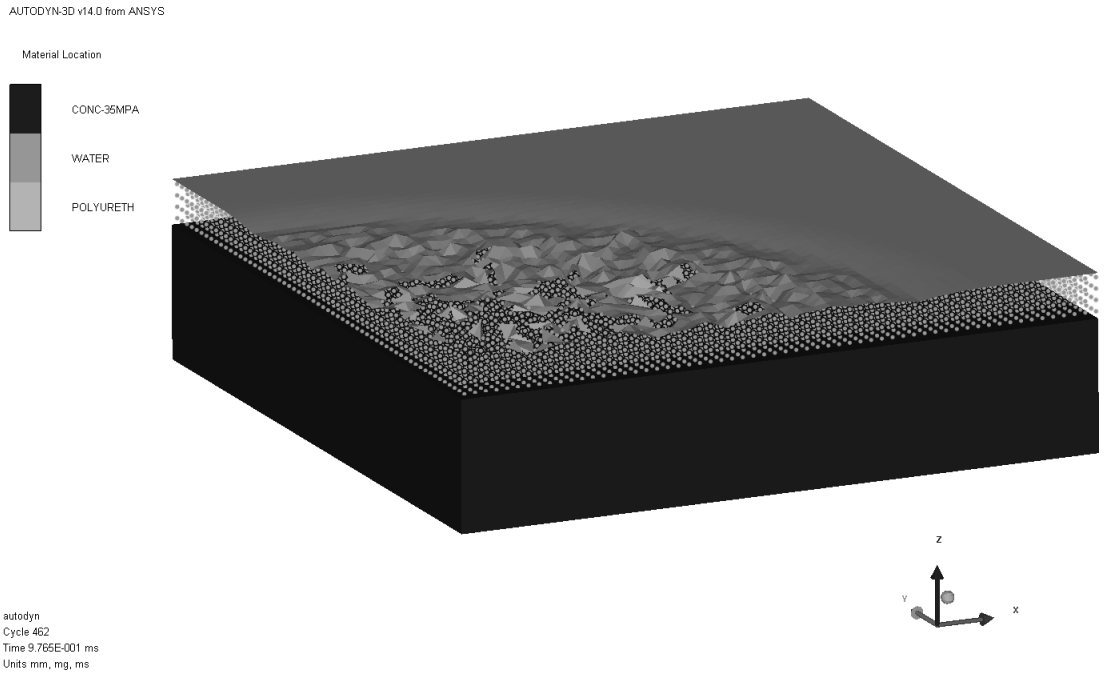

Figure 8.11 AUTODYN analytical blast model shortly after arrival of blast wave corresponding to $Z = 2.5\,\text{ft/lb}^3$; polyurethane shell eroding at geometric strains exceeding 150% to simulate the burning/tearing of the jacket's outer sheet.

unprotected concrete slab. At $Z = 5\,\text{ft/lb}^3$ the slab predominantly deforms elastically; at $Z = 2.5\,\text{ft/lb}^3$ spalling occurs at the leeward face of the slab, and at $Z = 1.25\,\text{ft/lb}^3$, bulk crushing and shear failures are predominant.

The ablative effects of the protective jackets of the tested thicknesses are shown in the mean gauge pressure vs. time graphs in Figures 8.13, 8.14 and 8.15, and the peak pressures for each case are summarized in Table 8.3 and Figure 8.16. Similarly, the total impulse imparted to the slab, taken as the numerical integral of the mean gauge pressure vs. time curves, are shown in Figures 8.17, 8.18 and 8.19, with the total impulses summarized in Table 8.4 and Figure 8.20. The pressure at selected elements around the point of arrival of the blast wave on the windward face of the slab were taken and averaged to produce a representative windward pressure and impulse.

The summarized pressure and impulse results show that for this configuration, the pressure reduction/magnification effect is generally more prounounced for less powerful (longer scaled standoff) blasts. The smallest jacket often provides no additional protection and can even magnify the pressure and impact imparted on the slab for the blasts with larger scaled distances.

For the blast loads chosen, there is an optimum jacket thickness around 4.5 in at which both the transmitted pressure and impulse are minimized, but at thicknesses beyond the optimum, the jacket's ablative capacity diminishes rapidly. Note that the relationship between jacket thickness is unlike the strictly-increasing energy dissipation effect that occured in the impact test simulations in Section 7.3, demonstrating that for the thickness of jackets studied, the behavior of the jacket under blast loading will not be well-represented by laboratory impact testing.

Simulations of the 2.5 $\text{ft/lb}^{1/3}$ blast on thicker jackets confirm the performance continues to degrade past the optimum; at 7.5 in, for example, the peak pressure on the slab is 5.23 MPa, only an 8% reduction in the peak reflected pressure on the jacket. Jackets larger than the optimum thickness appear to be more resistant to the break-up process, causing

them to behave as a rigid body that collides with the underlying structural element, transmitting the blast energy directly to the element with little mitigation occurring, rather than break up in front of it.

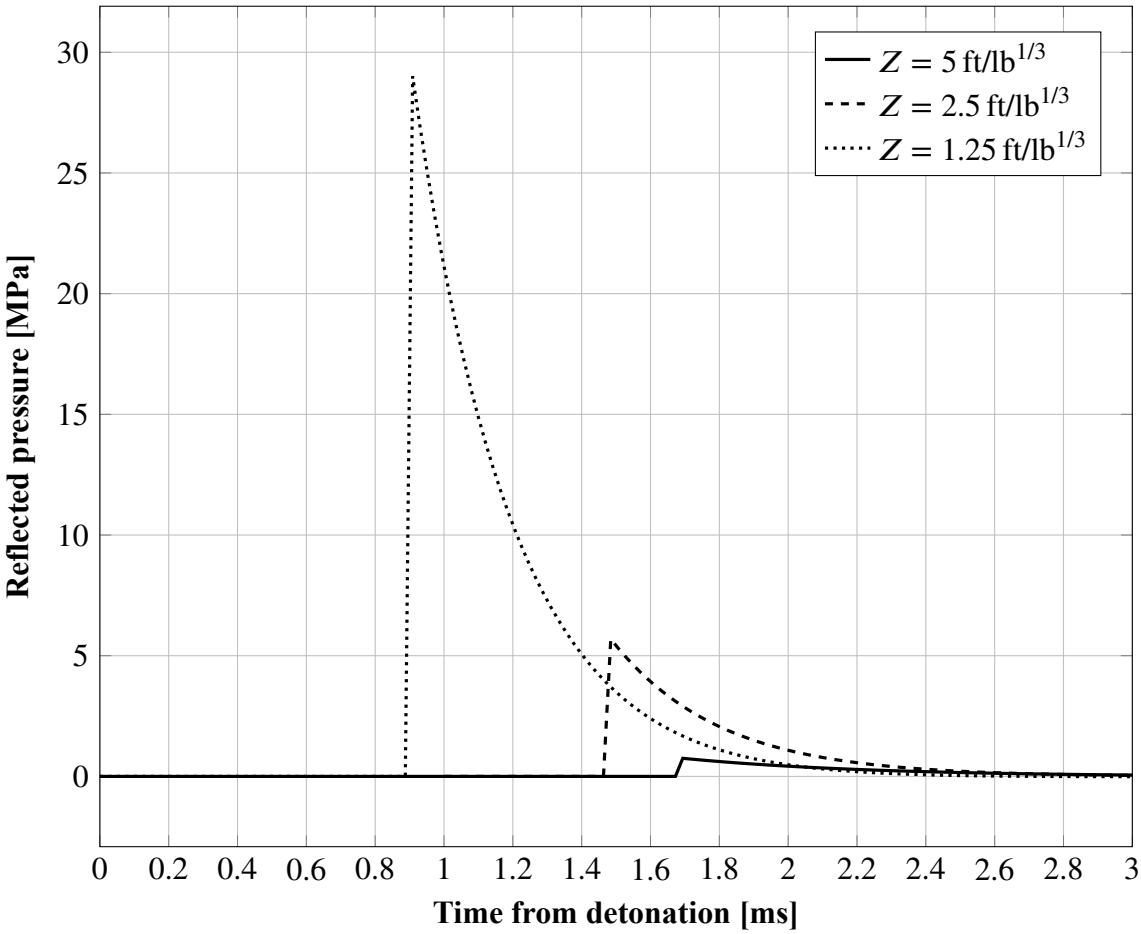

Figure 8.12 Reflected pressure histories of simulated blasts corresponding to Z =1.25 ft/lb$^{1/3}$, 2.5 ft/lb$^{1/3}$ and 5 ft/lb$^{1/3}$ at 10 ft standoff.

Table 8.2 Selected Parameters for Simulated Blasts at 10 ft Standoff

Scaled distance $Z = R/W^{1/3}$ **[ft /lb $^{1/3}$]**	**TNT mass** [kg]	**Time of arrival** [ms]	**Peak reflected pressure** [MPa]	**Positive impulse** [kN · s/m^2]
1.25 ft /lb $^{1/3}$	203 kg	0.909 ms	29.00 MPa	8.390 kN · s/m^2
2.5 ft /lb $^{1/3}$	29.0 kg	1.485 ms	5.69 MPa	1.828 kN · s/m^2
5 ft /lb $^{1/3}$	3.63 kg	1.694 ms	0.75 MPa	0.392 kN · s/m^2

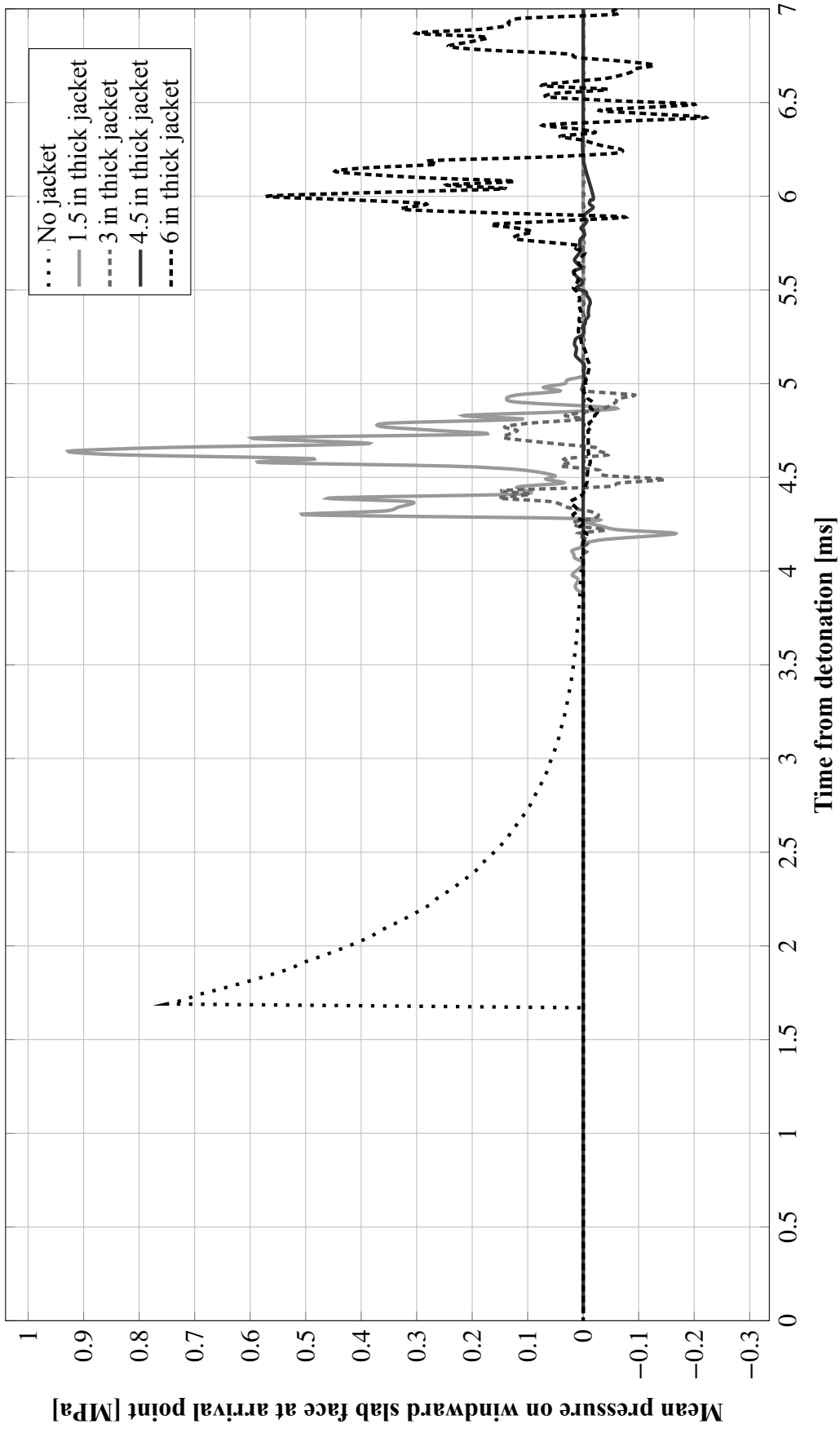

Figure 8.13 Comparison of pressure at top face of slab for protected and unprotected simulation cases, $Z = 5\,\mathrm{ft/lb^{1/3}}$.

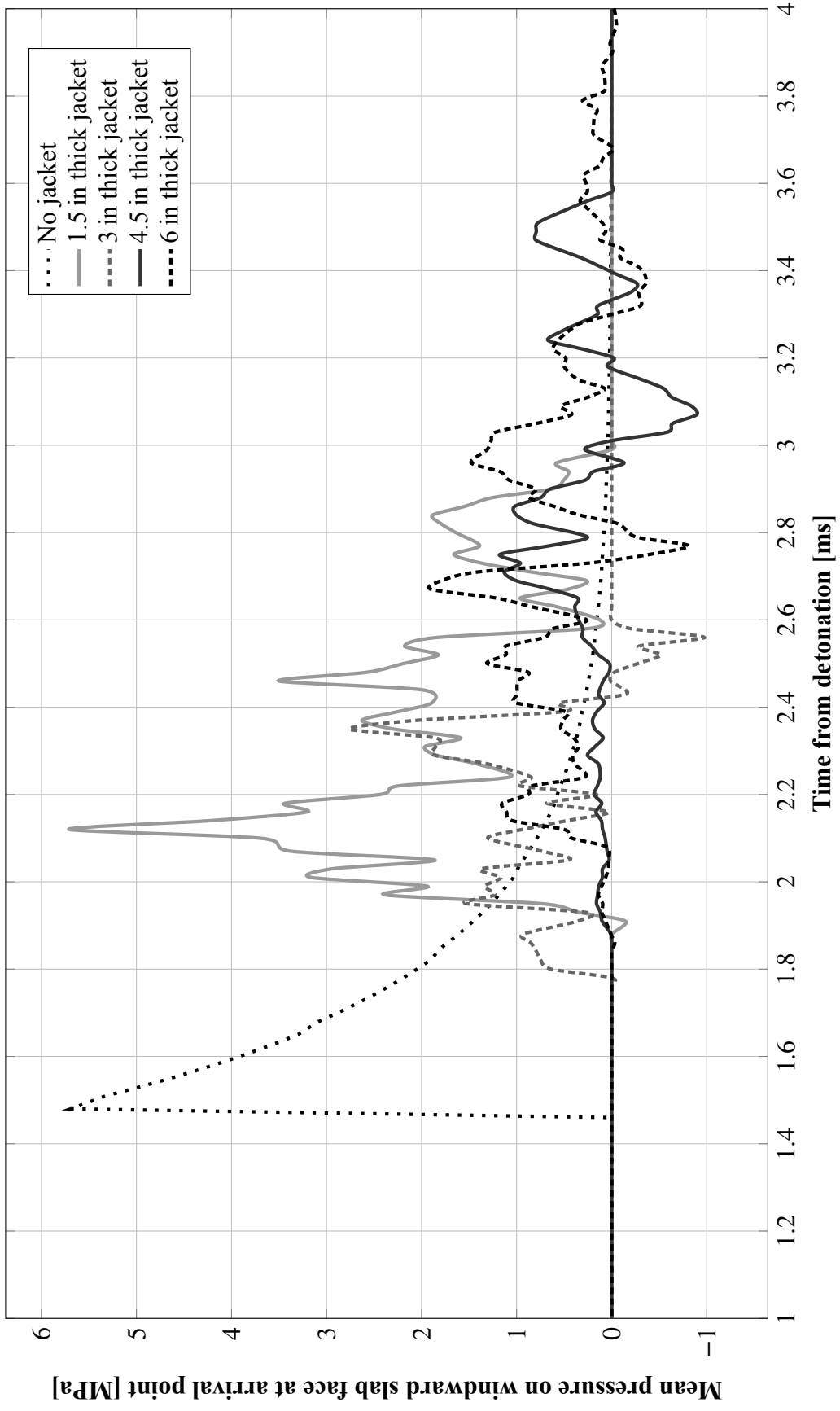

Figure 8.14 Comparison of pressure at top face of slab for protected and unprotected simulation cases, $Z = 2.5\,\mathrm{ft/lb^{1/3}}$.

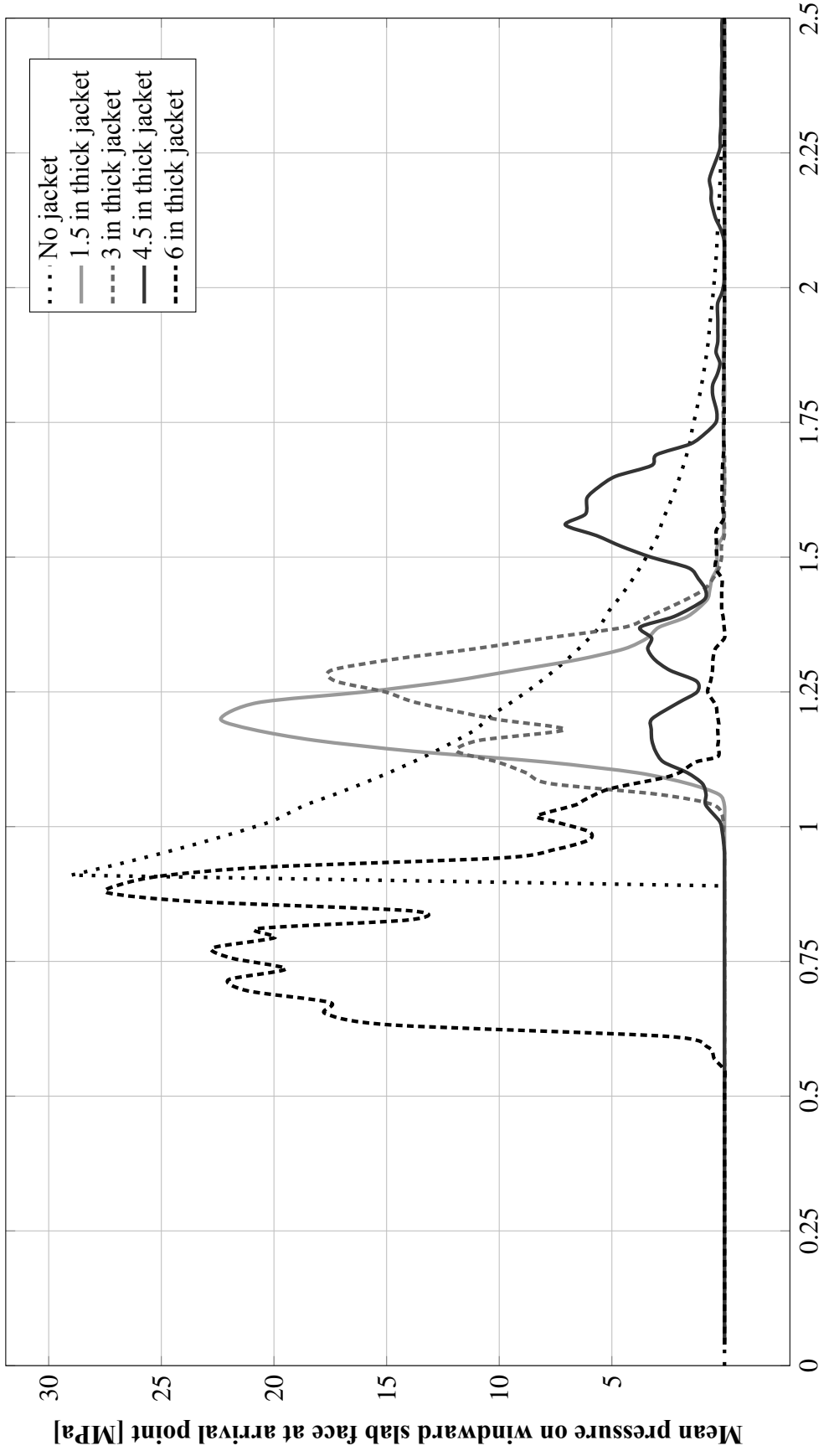

Figure 8.15 Comparison of pressure at top face of slab for protected and unprotected simulation cases, $Z = 1.25\,\mathrm{ft/lb^{1/3}}$.

Table 8.3 Peak Pressures at Top Face of Unprotected and Protected Slabs

	Jacket thickness				
Z	**None**	**1.5 in**	**3 in**	**4.5 in**	**6 in**
5.0 ft/lb$^{1/3}$	0.750 MPa	0.925 MPa	0.152 MPa	0.017 MPa	0.568 MPa
2.5 ft/lb$^{1/3}$	5.69 MPa	4.34 MPa	2.86 MPa	1.18 MPa	1.90 MPa
1.25 ft/lb$^{1/3}$	29.0 MPa	22.4 MPa	17.5 MPa	7.07 MPa	27.4 MPa

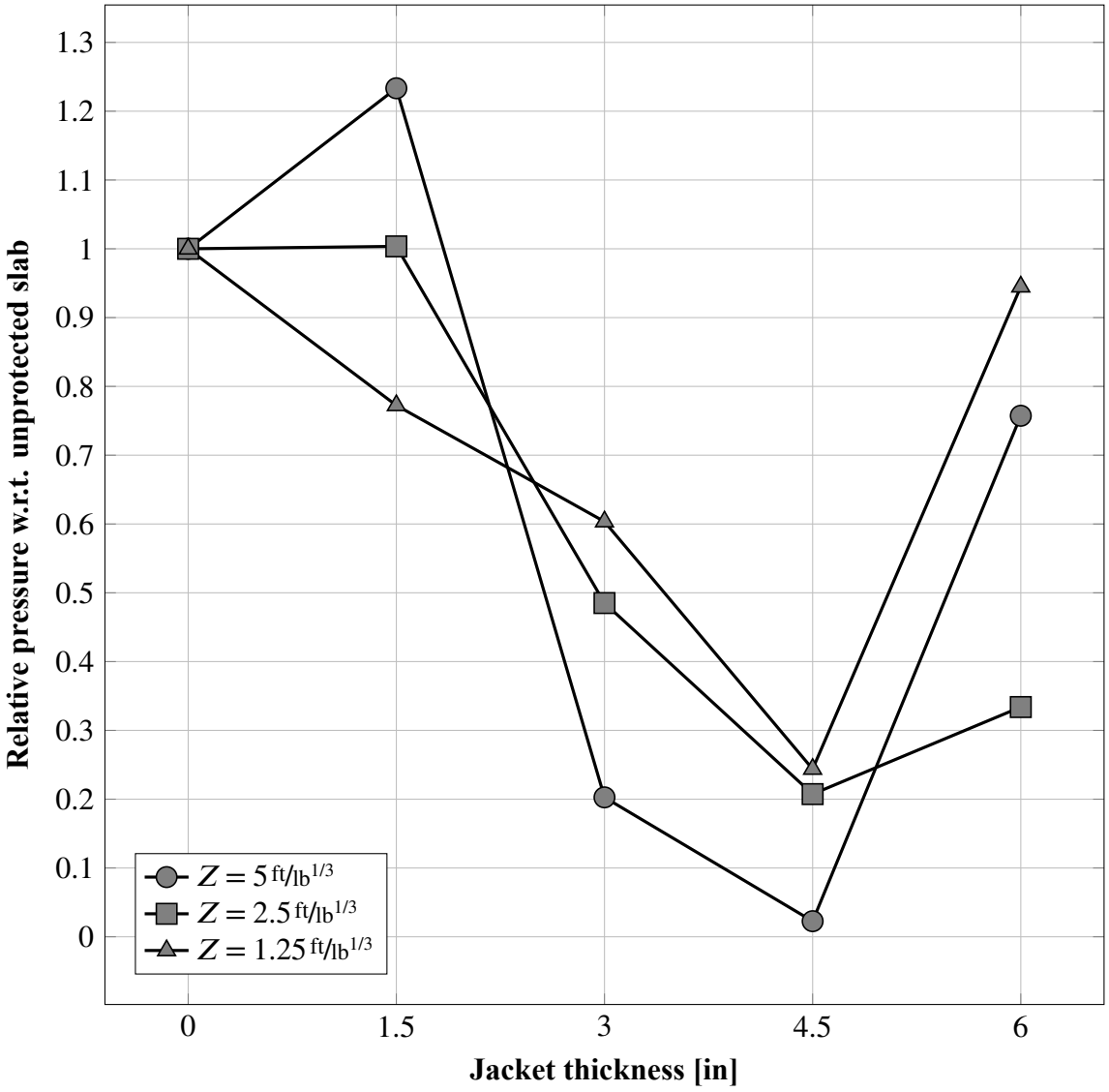

Figure 8.16 Relative peak pressure reduction at top face of protected and unprotected slabs for varying jacket thicknesses and scaled blast standoffs.

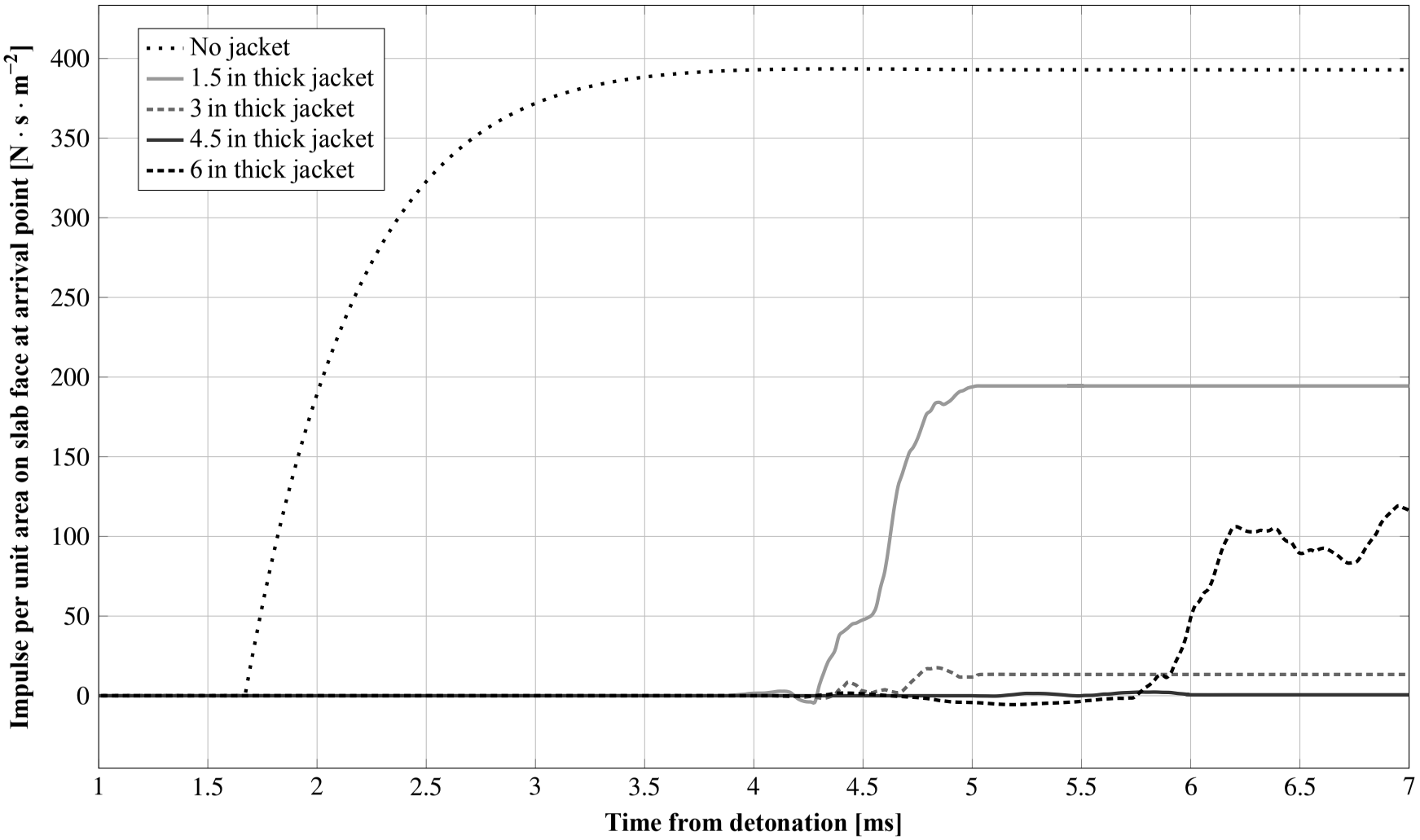

Figure 8.17 Comparison of impulse imparted on top face of slab for protected and unprotected simulation cases, $Z = 5\,\mathrm{ft/lb^{1/3}}$.

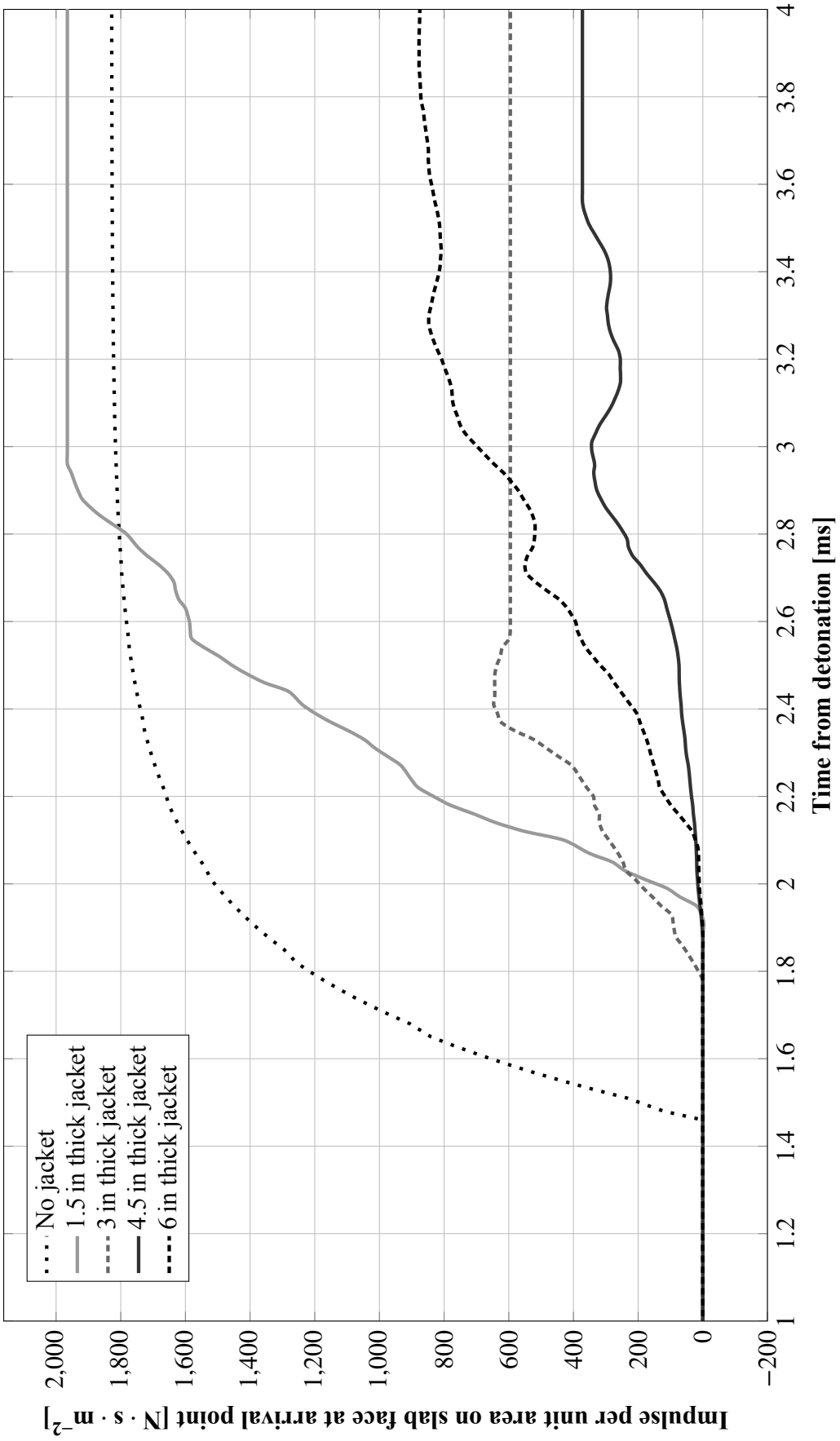

Figure 8.18 Comparison of impulse imparted on top face of slab for protected and unprotected simulation cases, $Z = 2.5\,\mathrm{ft/lb^{1/3}}$.

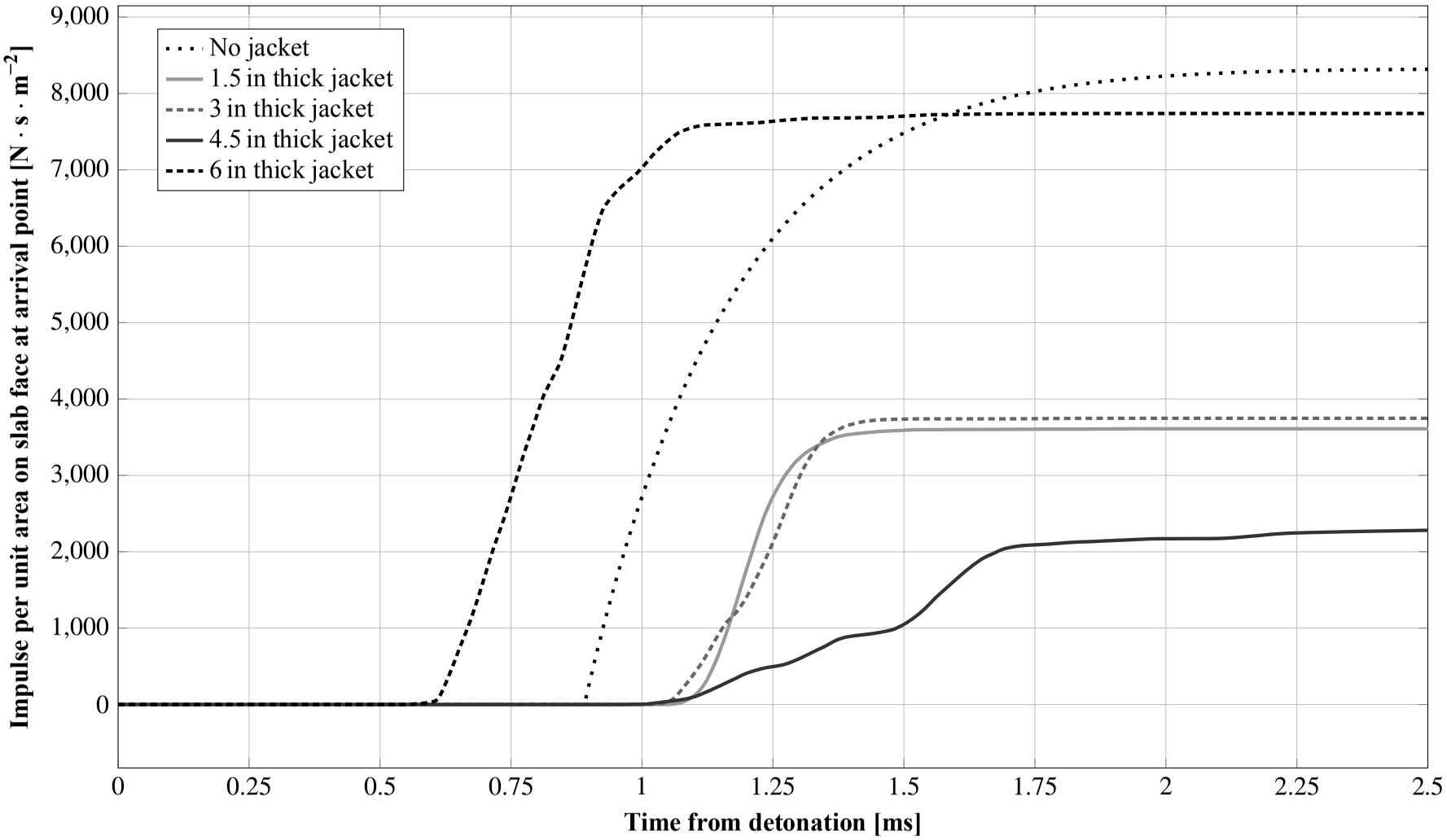

Figure 8.19 Comparison of impulse imparted on top face of slab for protected and unprotected simulation cases, $Z = 1.25\,\mathrm{ft/lb^{1/3}}$.

Table 8.4 Total Impulse per Unit Area On Top Face of Unprotected and Protected Slabs

	Jacket thickness				
Z	**None**	**1.5 in**	**3 in**	**4.5 in**	**6 in**
$5.0\,\mathrm{ft/lb^{1/3}}$	$393\,\mathrm{N\cdot s/m^2}$	$194\,\mathrm{N\cdot s/m^2}$	$17.6\,\mathrm{N\cdot s/m^2}$	$2.3\,\mathrm{N\cdot s/m^2}$	$119\,\mathrm{N\cdot s/m^2}$
$2.5\,\mathrm{ft/lb^{1/3}}$	$1830\,\mathrm{N\cdot s/m^2}$	$1965\,\mathrm{N\cdot s/m^2}$	$595\,\mathrm{N\cdot s/m^2}$	$375\,\mathrm{N\cdot s/m^2}$	$955\,\mathrm{N\cdot s/m^2}$
$1.25\,\mathrm{ft/lb^{1/3}}$	$8320\,\mathrm{N\cdot s/m^2}$	$3610\,\mathrm{N\cdot s/m^2}$	$3745\,\mathrm{N\cdot s/m^2}$	$2360\,\mathrm{N\cdot s/m^2}$	$7750\,\mathrm{N\cdot s/m^2}$

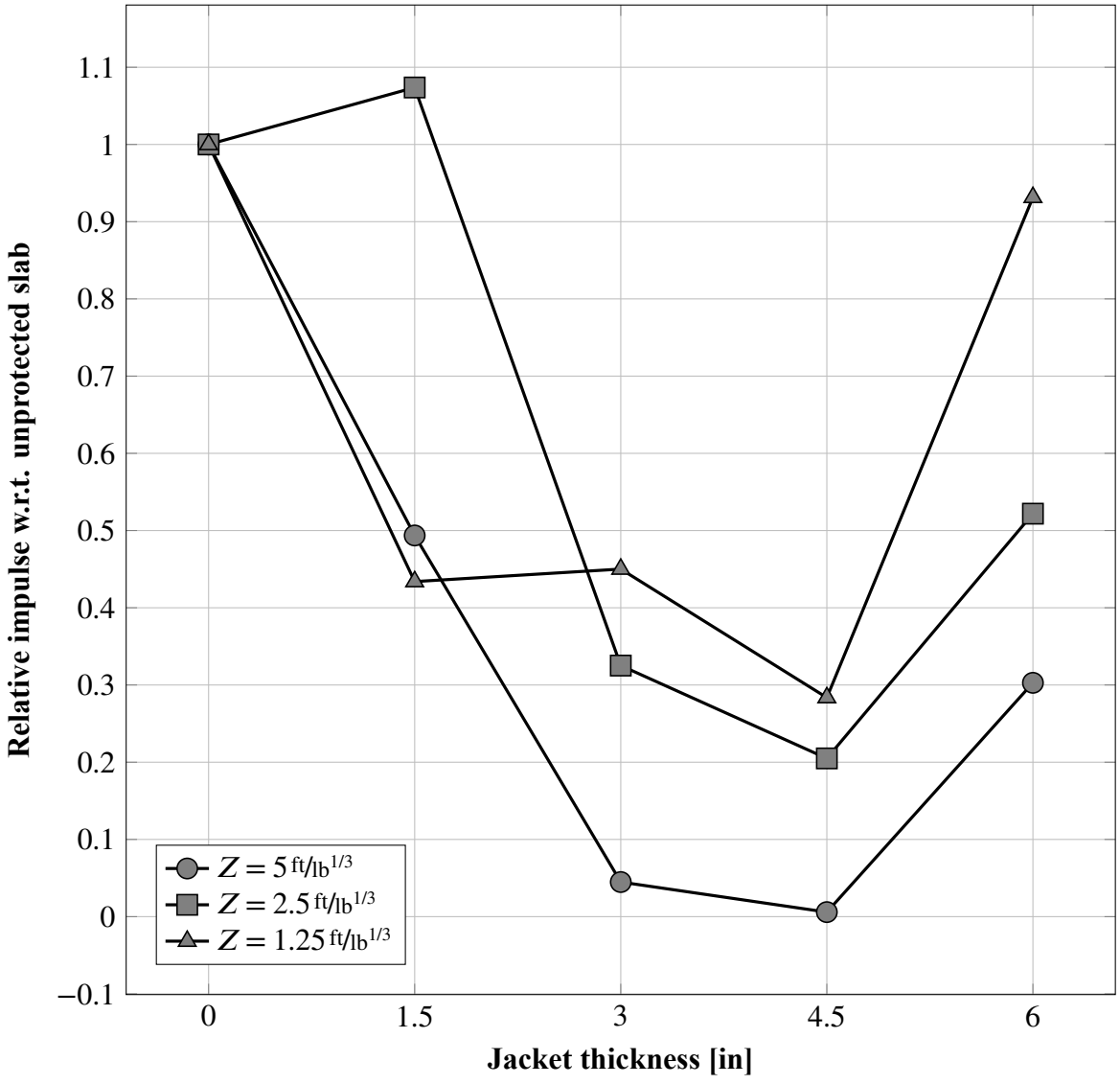

Figure 8.20 Relative impulse reduction at top face of protected and unprotected slabs for varying jacket thicknesses and scaled blast standoffs.

CHAPTER 9

EMPIRICAL MODEL FORMULATION

This chapter takes the results from the prior two chapters and develops them into an empirical model suitable for design engineers to employ for calculating the predicted relative pressure reduction of a given protective jacket at a design scaled standoff. Additionally, a suggested method on how to apply the empirical model to blast mitigation design is provided.

9.1 Proposed Empirical Energy Dissipation Model

For use in engineering design, a relationship between the required relative energy dissipation ψ, the scaled blast standoff chosen for design Z and the corresponding jacket thickness T_j is desired, so a designer can empirically choose an appropriate protection system for a given situation. As a proposed model, a multivariate fit to the simulation data was performed, using the Curve Fitting Toolbox in MATLAB 2012a to fit a polynomial surface to the relative impulse reductions measured in Section 8.3 and summarized in Table 9.1.

The chosen surface fit is linear in Z and cubic in T_j and the boundary conditions of the surface are defined so that $\psi(Z, 0) \equiv 0$. The equation for the surface is

$$\psi\left(Z, T_j\right) = 0.187T_j + 0.0272T_j^2 - 0.0097T_j^3 + 0.0237T_j Z, 0 \leq \psi \leq 0.95 \qquad (9.1)$$

Table 9.1 Relative Impulse Reduction by Simulated Jacket Thicknesses

	Relative impulse reduction at blast arrival point				
Z	**None**	**1.5 in**	**3 in**	**4.5 in**	**6 in**
5.0 ft/lb$^{1/3}$	0.00	0.51	0.96	0.99	0.70
2.5 ft/lb$^{1/3}$	0.00	−0.07	0.67	0.80	0.48
1.25 ft/lb$^{1/3}$	0.00	0.57	0.55	0.72	0.07

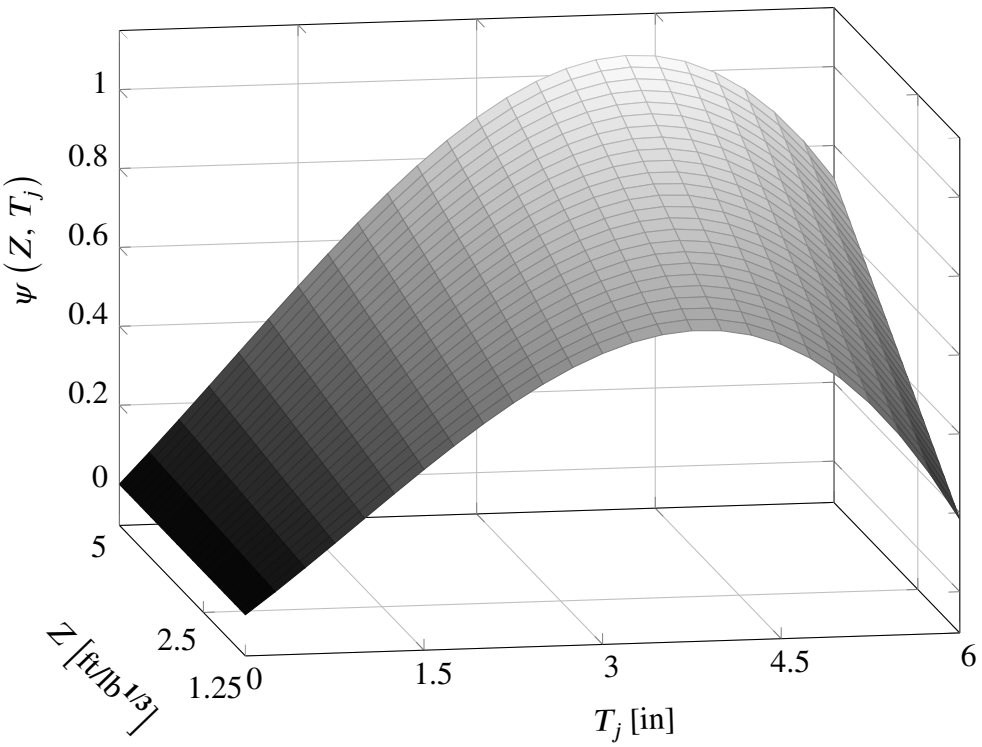

Figure 9.1 Empirical relationship for the relative pressure reduction of a protective jacket at a given scaled standoff and jacket thickness, from Equation 9.1.

This surface has an R-square goodness-of-fit value of $R^2 = 0.873$ and a root-mean square error of RMSE = 0.1527. This empirical equation is valid over the range of the simulated cases, $1.25 \leq Z \leq 5$ and $0 < T_j \leq 6$; T_j is a length in inches and Z is a scaled blast standoff in units of ft/lb$^{1/3}$. The value of ψ is capped at 0.95 because at the extremes of the graph, the predicted impulse reduction can exceed unity. The relationship is shown graphically over the valid range in Figure 9.1.

9.2 Suggested Method for Applying the Empirical Model to Design

1. Choose a set of blast performance objectives and corresponding scaled blast standoffs based on the probability and intensity of blast events the building is at risk of sustaining. For example, the National Earthquake Hazards Reductions Program's performance guidelines define the structural performance levels of *Collapse*, *Collapse Prevention*, *Life Safety*, *Immediate Occupancy* and *Operational* (Figure 9.2),

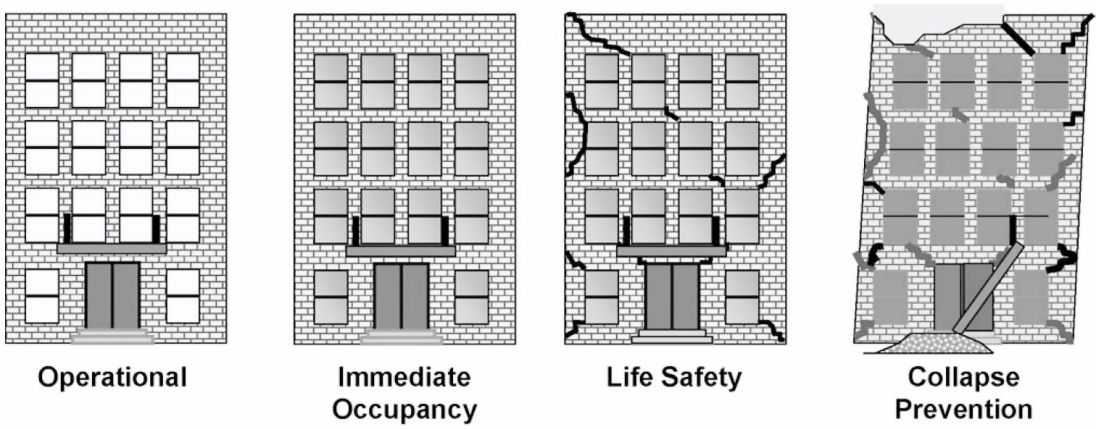

Figure 9.2 Graphical representation of post-disaster building performance meeting the NEHRP structural performance levels (Federal Emergency Management Agency 2004).

with corresponding qualitative descriptions of the building's resilience and quantitative structural and nonstructural component acceptance criteria; depending on the structure's importance factor, historical threat data, stochastic predictions of future threats, and the availability of passive protection systems and active security on site, probable blast loadings which correspond to each scenario can be chosen for analysis.

2. Use nonlinear analysis methods, such as those in the Departmen of Defense's Unified Facilities Criteria (Dalton et al. 2008) or the FEMA design handbooks (FEMA 2003), to determine the deflection and ductility demands of the structure, and calculate the total amount of energy dissipated through plastic deformation of critical members using the area under the element's pushover ($P-\Delta$) curve.

3. For each critical member that fails to meet its structural performance level's acceptance criteria, calculate the volumetric energy dissipation to the point where the critical performance criterion governs, and use that to find the ratio of external energy dissipation required to bring it into compliance.

4. Using the scaled blast standoff and the required energy dissipation ratio, calculate the minimum thickness of the protective jacket, and apply a safety factor if required.

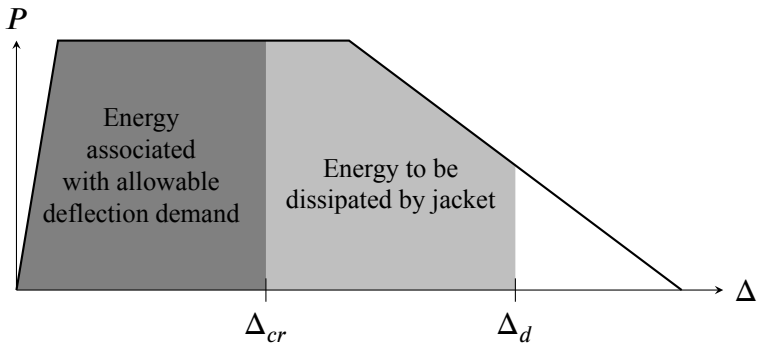

Figure 9.3 Suggested graphical method for finding required energy dissipation ratio using the area underneath the pushover curve.

5. Considering the historical threat data, the structure's importance, and the accessibility and strength of the critical members that require extra ablative dissipation, decide if the protective jackets should be deployed full-time or only during periods of elevated risk of blast events exceeding those corresponding to an *Immediate Occupancy* class of performance level.

6. If the required energy dissipation is not possible with any jacket thickness, other blast mitigation methods will need to be used either in lieu of or in concert with the protective jacket.

As a basic illustrative example, consider a column with the simple pushover curve shown in Figure 9.3, subject to a chosen design blast with scaled standoff distance Z_d. The deflection demand Δ_d placed on the column exceeds the critical performance criterion Δ_{cr}, so it is a critical element that requires additional energy ablation. The required energy dissipation ratio is equal to

$$\psi_{req} = 1 - \frac{\int_0^{\Delta_{cr}} P\, d\Delta}{\int_0^{\Delta_d} P\, d\Delta} \tag{9.2}$$

and would be provided by a jacket of thickness T_{jd} that satisfies the equation $\psi_{req} = \psi\left(T_{jd}, Z_d\right)$. If an additional safety factor Ω is required of the energy dissipation, then a jacket thickness that satisfies $\Omega\psi_{req} = \psi\left(T_{jd}, Z_d\right)$ would suffice.

CHAPTER 10

CONCLUSIONS AND RECOMMENDATIONS

This final chapter summarizes the findings and observations recorded over the course of this study, as well as suggesting directions for further research based on the ablative protective jacket concept.

10.1 Summary

The thesis begins by discussing the objectives behind developing a temporary blast protection system, and briefly summarizes the prior research on the use of water as a blast mitigation material and the reasons behind the choices that led to the design of the jacket prototype. The importance of preventing progressive collapse in existing structures via protecting vulnerable structural elements that, for whatever reason, cannot be strengthened is the main motivation behind the design of the jacket.

The theoretical reasoning behind the kinetic and thermodynamic energy dissipation modes is laid out, with example calculations to demonstrate the theoretical capacity of a layer of water to absorb a significant amount of energy through droplet formation and evaporation. The mitigation capacity of the water layer during a blast event is estimated, and drawing on the existing research literature to show that the assumptions of enthalpy capacity, mist formation and evaporation time required to mobilize the mitigation potential of the water are valid, the jacket is found to have a significant capacity for energy ablation. The initial investigations on the water-filled jackets demonstrated that the hypothetical use of the jackets to dissipate dynamic loading had practical merit.

The foundations of the finite element method and the equations of state and material models used to discretize and analyze the capacity of the jackets are laid out briefly, including the important topics of smoothed particle hydrodynamics, the Johnson-Holmquist damage parameter and the AUTODYN Analytical Blast boundary condition, all of which

were important components of the following simulations. The first attempts at producing finite element simulations of the protective effects of the jacket are discussed.

The simulations of impact loading validate the theorized kinetic dissipation mode, demonstrating a significant ablative effect at even very small thicknesses of water, and the ability to effectively redirect a dynamic loading that would otherwise cause catastrophic damage to a structural element.

The discussion of blast loading simulations begins by comparing the empirical Analytical Blast boundary condition to a prior set of simulations performed with the traditional Euler remapping method of simulating blast loading, and the results from the Analytical Blast simulations are found to be slightly conservative but to largely agree with the more computationally complex method. The Analytical Blast boundary and the smoothed particle hydrodynamics meshless model are then used to modify the previous chapters' simulations to study the effects of blast loading, where the jackets are again found to have a significant capacity for energy absorption and structural protection. However, unlike the impact tests, the jackets are found to have an optimal thickness near 4.5 in for the selected blast loads and structural configuration, meaning that the results of impact testing would not correspond well to the capacity of the jackets under blast load.

An empirical model for calculating the energy reduction provided by a jacket of given thickness for a design blast load is then presented, along with a proposed method for applying the protective jackets in a situation where the performance demands of a building are greater than the required performance criteria.

10.2 Conclusions

From this research, the following conclusions can be made:

- The use of water as an integral part of a blast or impact mitigation system is effective at dissipating energy and preventing damage to the underlying structural members.
- For water to be able to mitigate the effect of blast loads through phase change, the

water would need to be broken up into an ultra-fine mist with a very high surface area for the evaporation to take place; a review of the literature confirms that the mist forms and evaporates in milliseconds, within the typical time scale of a blast event.

- Modifying a structural element's cross section so that the windward face of the column is curved or has a leading edge reduces the peak pressure and total impulse imparted to the element during a blast event. This shape modification could be built into the protective jackets.

- Over the simulated jacket thicknesses evaluated, the optimum thickness of the water layer that minimizes both the peak reflected pressure and total impulse of a blast event on the underlying structural member is approximately 4.5 in.

- However, in the case of impact loading, no optimum thickness for energy dissipation is evident. While it is qualitatively effective at dissipating energy in both cases, unfortunately, a given jacket's behavior and response during impact is not a good predictor of its quantitative behavior during a blast event.

- The Analytical Blast condition, compared to the traditional method of remapped Euler simulations, produces simulation results that are conservative near geometric discontinuities where flow-field interactions cause pressure reductions through the generation of expansion fans, but are in close agreement otherwise. Additionally, they are much less computationally intensive, allowing for more rapid simulations and lending its use to design iteration.

- The empirical model chosen to represent the relationship between jacket thickness $T_j \in [0\,\text{in}, 6\,\text{in}]$, scaled blast distance $Z \in \left[1.25\,\text{ft/lb}^{-1/3}, 5\,\text{ft/lb}^{-1/3}\right]$ and energy dissipation relative to the unprotected case ψ is Equation 9.1,

$$\psi\left(Z, T_j\right) = 0.187T_j + 0.0272T_j^2 - 0.0097T_j^3 + 0.0237T_j Z, 0 \leq \psi \leq 0.95$$

- Designers can calculate the required layer thickness of the protective jacket required for a member to meet a given structural performance criterion during a blast event with scaled standoff Z_d by using the member's pushover curve to calculate the ratio of the energy absorbed by the unprotected member during the blast event to the allowable energy absorption that brings the member to the specified ductility demand, then finding the value of T_{jd} that satisfies $\psi\left(Z_d, T_{jd}\right) = \psi_{req}$.

10.3 Recommendations for Future Research

The following are some possible directions for research to expand on this investigation. Many of the recommendations involve topics that would benefit from interdisciplinary investigation.

10.3.1 Extension and Verification of the Empirical Models

Additional simulations in the vein of those performed in Chapters 7 and 8, performed with a wider variety of scaled blast standoffs, jacket thicknesses and configurations, and types of structural members, can be performed to extend and verify the proposed empirical model for determining the energy dissipation properties of the protective jacket systems. Additional thermodynamic modeling of the water jacket, performed with computational fluid dynamics packages or multiscale methods, could be performed to study the micro- and mesoscale behavior of the water droplets during the blast event.

10.3.2 Experimental Blast Testing

The most straightforward direction for future research on this topic is to perform blast testing on the protective jackets with live explosives, in cooperation with a research institution equipped to handle the requirements and regulations inherent to live blast tests, and quantitatively and qualitatively measure the performance of the jackets as compared to the simulation predictions from Chapter 8.

Another research possibility is to perform controlled simulated blast testing to as-

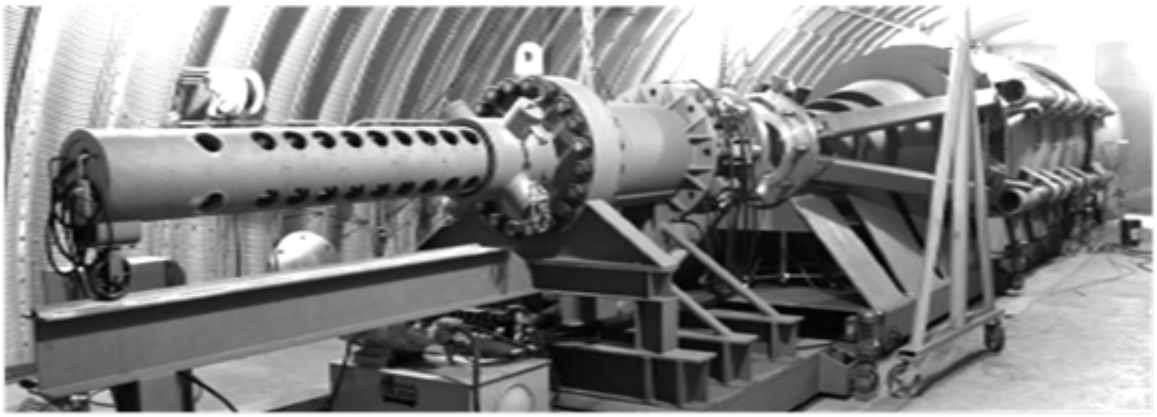

Figure 10.1 Blast load simulator at the Engineering Research and Development Center in Vicksburg, MS.

certain the mitigating effects of the protective jackets and relate these results to the finite element simulations; a blast load simulator that creates repeatable, controlled blast conditions such as the one at the Vicksburg Engineering Research and Development Center (Figure 10.1) would be the ideal way of performing these tests. However, depending on the capabilities of the blast load simulator, the simulated blast wave may or may not be of a comparable temperature to a blast created by live explosives, so the tests may be limited to examining the kinetic attenuation mode.

10.3.3 Design Refinement and Material Choice

In cooperation with chemists, polymer scientists and manufacturing engineers, interdisciplinary research can be performed to optimize the design and fabrication of the protective jacket: for example, finding the optimal polymer material and thickness, testing the effects of additives and solutes in the water (for example, surfactants to reduce the surface tension of the water and increase its dissipation speed, antifreeze for increasing the exterior temperature exposure servicability range or fire suppressant to increase the fire rating of a structure), optimizing the exterior shape of the jacket and investigating the effect of the stellate and "quilted" water distributions described in Section 1.5, or developing an automated manufacturing process that does not require filling the jackets by hand and sealing

them with chemical adhesives.

10.3.4 Architectural Finishing and Mounting

The methods for mounting, installing and maintaining the protective jackets, as well as the aesthetics and exterior finish of the jackets, could be studied in tandem with architects, construction technicians and urban designers, to increase the speed and ease with which the jackets are mounted without adversely affecting the occupancy, function or architectural appearance of the structure they are protecting.

REFERENCES

Absil, L. and Bryntse, A. (2006). "Blast mitigation by water." *Report No. FOI-R–2049–SE*, Totalförsvarets forskningsinstitut [Swedish Defence Research Agency], Stockholm, Sweden, <http://www2.foi.se/rapp/foir2049.pdf> (Jan. 19, 2011).

Adiga, K., Willauer, H., Ananth, R., and Williams, F. (2009). "Implications of droplet breakup and formation of ultra fine mist in blast mitigation." *Fire Safety Journal*, 44(3), 363–369.

Allahverdi, N. H. (2010). "Coupled simulation of loading and response of columns under extreme events." Doctoral dissertation, New Jersey Institute of Technology, Newark, NJ.

Ananth, R., Ladouceur, H., Willauer, H., and Farley, J. (2008). "Effect of water mist on a confined blast." *Suppression and Detection Research and Applications–A Technical Working Conference (SUPDET 2008)*, National Fire Protection Association, ed., Orlando, FL, <http://www.nfpa.org/assets/files/PDF/Foundation proceedings/Ananth.pdf> (Jan. 19, 2011).

ANSYS Inc. (2011). *ANSYS AUTODYN 12.1*.

Bathe, K.-J. (1996). *Finite element procedures*. Prentice-Hall, Englewood Cliffs, NJ.

Birnbaum, N., Fairlie, G. E., and Francis, N. J. (1998). "Numerical Modeling of Small Scale Water Mitigation Feasibility Tests." *Report No. N47408-97-M-0928*, Century Dynamics, Inc., San Ramon, CA.

Borrvall, T. and Riedel, W. (2011). "The RHT concrete model in LS-DYNA." *Proc. 8th European LS-DYNA Users Conference*, Strasbourg, France, <http://www.dynalook.com/8th-european-ls-dyna-conference/session-12/Session12_Paper1.pdf> (Oct. 14, 2012).

Brannon, R. and Leelavanichkul, S. (2009). "Survey of four damage models for concrete." *Report No. SAND2009-5544*, Sandia National Laboratories, Albuquerque, New Mexico, <http://prod.sandia.gov/techlib/access-control.cgi/2009/095544.pdf> (Oct. 14, 2012).

Carlson, N. J. and Saadeghvaziri, M. A. (2010a). "A multi-hazard protective jacket for structural members." *Structures Congress 2010*, 369(41130), 303.

Carlson, N. J. and Saadeghvaziri, M. A. (2010b). "On multi-hazard considerations on design of structures." *9th U.S. National & 10th Canadian Conference on Earthquake Engineering: Proceedings*, Toronto, ON, Canada.

Carter, C. J. (2011). "The inherent blast-resistance of steel framing." *Modern Steel Construction*, 9(August), 34–36.

Century Dynamics (2005). *AUTODYN remapping tutorial*. Horsham, West Sussex, UK, 4.3 rev. edition.

Century Dynamics (2006). *Hands-on session #12: detonation (2D wedge)*. Horsham, West Sussex, UK.

Chapman, T. (1995). "Blast wave simulation using AUTODYN2D: A parametric study." *International Journal of Impact Engineering*, 16(5-6), 777–787.

Cheng, M., Hung, K. C., and Chong, O. Y. (2005). "Numerical study of water mitigation effects on blast wave." *Shock Waves*, 14(3), 217–223.

Chong, W. K., Lam, K. Y., Yeo, K. S., Lin, G. R., and Chong, O. Y. (1999). "A comparison of simulations results with experiment on water mitigation of an explosion." *Shock and Vibration*, 6, 73–80.

Chun, S. (2004). "Nonlinear fluid-structure interaction in a flexible shelter under blast loading." Doctoral dissertation, Virginia Polytechnic Institute and State University, Blacksburg, VA, <http://scholar.lib.vt.edu/theses/available/etd-12012004-110546/> (Nov. 14, 2011).

Coleburn, N. (1964). "Chapman-Jouguet pressures of several pure and mixed explosives." *Report No. NOLTR 64-58*, Naval Ordnance Lab, White Oak, MD, <http://oai.dtic.mil/oai/oai?verb=getRecord&metadataPrefix=html&identifier=AD0603540> (Feb. 9, 2013).

Committee on Feasibility of Applying Blast-Mitigating Technologies and Design Methodologies from Military Facilities to Civilian Buildings (1995). *Protecting buildings from bomb damage: transfer of blast-effects mitigation technologies from military to civilian applications*. Board on Infrastructure and the Constructed Environment Commission on Engineering and Technical Systems National Research Council. National Academy Press, Washington, D.C., <http://www.nap.edu/openbook.php?isbn=0309053757> (Jan. 19, 2011).

Dalton, J., Gott, J., Parker, P., McAndrew, M., and Bowling, C. (2008). *Unified facilities criteria: structures to resist the effects of accidental explosions (UFC 3-340-02)*. Department of Defense, Washington, D.C.

Department of the Army (1986). *Fundamentals of protective design for conventional weapons*. Number TM 5-855-1 in Army Technical Manual. Department of Defense, Washington, D.C.

Department of the Navy (1999). *Selection and application of vehicle barriers (MIL-HDBK-1013/14)*. Department of Defense, Washington, D.C.

Donea, J., Giuliani, S., and Halleux, J. (1982). "An arbitrary Lagrangian-Eulerian finite element method for transient dynamic fluid-structure interactions." *Computer Methods in Applied Mechanics and Engineering*, 33(1-3), 689–723.

Eriksson, S. (1974). "Water in explosives storage." *4th International Symposium on the Military Applications of Blast Simulation (MABS 4)*, Southend-on-Sea, England.

Eriksson, S. and Vretblad, B. (1994). "Blast mitigation in confined spaces by energy absorbing materials." *26th Department of Defense Explosives Safety Seminar*, Miami, FL.

Federal Emergency Management Agency (2003). *Primer for design of commercial buildings to mitigate terrorist attacks (FEMA 427)*. Risk Management Series. FEMA, Washington, D.C.

Federal Emergency Management Agency (2004). *Primer for design professionals (FEMA 389)*. Risk Management Series. FEMA, Washington, D.C.

Glasstone, S. (1962). *The effects of nuclear weapons.* U.S. Atomic Energy Commission, Washington, D.C., revised edition.

Gurley, C. (2008). "Progressive collapse and earthquake resistance." *Practice Periodical on Structural Design and Construction*, 13(1), 19.

Hadden, D. (2003). "Overview of blast mitigation design measures.

J. O. Hallquist, ed. (1998). *LS-DYNA theoretical manual*. Livermore Software, Livermore, CA.

Hayhurst, C., Clegg, R., Livingstone, I., and Francis, N. (1996). "The application of SPH techniques in AUTODYN-2D to ballistic impact problems." *16th International Symposium on Ballistics*, 23–28.

Jalaal, M. and Mehravaran, K. (2012). "Fragmentation of falling liquid droplets in bag breakup mode." *International Journal of Multiphase Flow*, 47(0), 115 – 132.

Joachim, C. E. and Lunderman, C. V. (1997). "Blast suppression with water: results of small-scale test program." *Proc. 15th International Symposium on Military Aspects of Blast and Shock*, Banff, Alberta, Canada, 207–224 (Paper SB03).

Keenan, W. A. and Wager, P. C. (1992). "Mitigation of confined explosion effects by placing water in proximity of explosives." *25th Department of Defense Explosives Safety Seminar*, Anaheim, CA, <http://www.dtic.mil/cgi-bin/GetTRDoc?AD=ADA529566> (January 19, 2011).

Lee, E. and Hornig, H. (1968). "Adiabatic expansion of high explosive detonation products." *Report No. UCRL–50422*, Lawrence Radiation Laboratory, UC Livermore, <http://www.osti.gov/energycitations/product.biblio.jsp?osti_id=4783904> (Dec. 5, 2011).

Liu, J. (2010). "Preventing progressive collapse through strengthening beam-to-column connection, Part 1: Theoretical analysis." *Journal of Constructional Steel Research*, 66(2), 229–237.

Malvar, L. J. and Tancreto, J. E. (1998). "Analytical and test results for water mitigation of explosion effects." *28th DOD Explosives Safety Seminar*, Orlando, FL.

Mays, G. C. and Smith, P. D. (2001). *Blast effects on buildings*. Thomas Telford Publications, London.

Mills, C. (1987). "The design of concrete structures to resist explosions and weapon effects." *Proc. 1st Int. Conf. on Concrete for Hazard Protections*, Edinburgh, United Kingdom, 61–73.

Morgan, K. (1984). "An expansion equation of state subroutine." *Computer Physics Communications*, 35, C–167.

Nair, R. (2006). "Preventing disproportionate collapse." *Journal of Performance of Constructed Facilities*, 20(4), 309.

Ngo, T., Mendis, P., Gupta, A., and Ramsay, J. (2007). "Blast loading and blast effects on structures – an overview." *Electronic Journal of Structural Engineering*, Special Issue, 76–91.

Pilch, M. and Erdman, C. A. (1987). "Use of breakup time data and velocity history data to predict the maximum size of stable fragments for acceleration-induced breakup of a liquid drop." *International Journal of Multiphase Flow*, 13(6), 741–757.

Pujol, S. and Smith-Pardo, J. P. (2009). "A new perspective on the effects of abrupt column removal." *Engineering Structures*, 31(4), 869–874.

Razaqpur, A. G., Tolba, A., and Cotestabile, E. (2007). "Blast loading response of reinforced concrete panels reinforced with externally bonded GFRP laminates." *Composites Part B: Engineering*, 38(5-6), 535–546.

Schwer, D. A. and Kailasanath, K. (2005). "Water-mist mitigation of quasi-static pressure buildup in enclosures subjected to an explosion." *19th International Colloquium on the Dynamics of Explosions & Reactive Systems*, Paper 64.

Schwer, L., Saadeghvaziri, M. A., O'Daniel, J., and Madsen, T. (2008). "Free-air blast simulation: engineering models and MM-ALE calculations." *20th International Symposium on Military Aspects of Blast and Shock*, Oslo, Norway.

Sozen, M. A., Thornton, C. H., Corley, W. G., and Mlakar, Sr., P. F. (1998). "The Oklahoma City bombing: structure and mechanisms of the Murrah Building." *Journal of Performance of Constructed Facilities*, 12(3), 120.

US Army Corps of Engineers Protective Design Center (2012). *ConWep*, <https://pdc.usace.army.mil/software/conwep> (Feb. 2, 2011).

Vaziri, A., Xue, Z., and Hutchinson, J. W. (2006). "Metal sandwich plates with polymer foam-filled cores." *Journal of Mechanics of Materials and Structures*, 1(1), 97–127.

Willauer, H. D., Ananth, R., Farley, J. P., and Williams, F. W. (2009). "Mitigation of TNT and Destex explosion effects using water mist." *Journal of hazardous materials*, 165(1-3), 1068–73.

Xue, Z. and Hutchinson, J. W. (2003). "Preliminary assessment of sandwich plates subject to blast loads." *International Journal of Mechanical Sciences*, 45(4), 687–705.

Zhao, H., Liu, H.-F., Cao, X.-K., Li, W.-F., and Xu, J.-L. (2011). "Breakup characteristics of liquid drops in bag regime by a continuous and uniform air jet flow." *International Journal of Multiphase Flow*, 37(5), 530–534.

Zukas, J. A. and Walters, W. P. (1998). *Explosive effects and applications*. Springer, New York.